Investigation and Use of Dual (Twin) Low Pressure Proportional Counters for Active Neutron-Gamma Mixed Field Dosimetry

by

Faezeh Forouzan

A thesis submitted to the
School of Graduate and Postdoctoral Studies in partial
fulfillment of the requirements for the degree of

Doctor of Philosophy in Nuclear Engineering

Department of Energy and Nuclear Engineering

University of Ontario Institute of Technology (Ontario Tech University)

Oshawa, Ontario, Canada

May 2023

THESIS EXAMINATION INFORMATION

Submitted by: **Faezeh Forouzan**

PhD in **Nuclear Engineering**

Thesis title: Investigation and Use of Dual (Twin) Low Pressure Proportional Counters for Active Neutron-Gamma Mixed Field Dosimetry.

An oral defense of this thesis took place on April 4, 2023 in front of the following examining committee:

Examining Committee:

Chair of Examining Committee	Dr. Jennifer McKellar
Research Supervisor	Dr. Kirk Atkinson
Research Co-supervisor	Dr. Anthony Waker
Examining Committee Member	Dr. Edward Waller
Examining Committee Member	Dr. Glenn Harvel
University Examiner	Dr. Malcolm McEwen
External Examiner	Dr. James Gräfe, Toronto Metropolitan University

The above committee determined that the thesis is acceptable in form and content and that a satisfactory knowledge of the field covered by the thesis was demonstrated by the candidate during an oral examination. A signed copy of the Certificate of Approval is available from the School of Graduate and Postdoctoral Studies.

ABSTRACT

This thesis tackles accurate neutron-gamma mixed field dosimetry in radiation protection and radiation biology. While passive dosimeters are suitable for measuring low radiation levels, active instruments are necessary in high radiation environments, such as found in nuclear power plants and particle accelerator facilities and it is highly desirable to develop a single detector capable of discriminating between neutrons and gamma rays, providing real-time and independent dose-rate measurements.

Tissue equivalent proportional counters (TEPCs) have been used, but their accuracy is limited. In this study, a custom-built Cylindrical Graphite Proportional Counter (Cy-GPC) along with a twin Cylindrical TEPC (Cy-TEPC) has been extensively investigated for n-γ mixed field dosimetry. Following a series of experiments to confirm the identical nature of both counters for photon dosimetry, various mixed-radiation field measurements were conducted to explore the operation of the dual counters over a wide range of neutron and photon energies and health physics operational environments.

Monte-Carlo modeling was employed to assist in interpreting the experimental data and determining the neutron sensitivity of the graphite-walled counter. The study demonstrates that utilizing dual counters and the proposed methods improves neutron dose rate precision by approximately 5% to 20% compared to the standard TEPC method. This improvement is particularly significant in radiation biology and medical neutron applications, but of lesser importance in radiation protection where stringent accuracy requirements are not as crucial.

The GPC's graphite wall exhibits limited sensitivity to neutrons, while the tissue equivalent gas inside the counter contributes to neutron sensitivity at specific energies. However, within the framework of radiation protection, it is acceptable to assume that energy deposition events above 10 keV/μm in a TEPC are attributable to neutrons, and events below 20 keV/μm recorded by a graphite-walled counter are solely due to photons.

The agreement between measured and simulated data validates the use of simulations for predicting counter performance, particularly in scenarios where actual measurements are impractical, such as space exploration or future particle beam radiotherapy facilities. The study provides suggestions for counter geometry and manufacturing for facilitating the design of a single device that effectively addresses the challenges of neutron-gamma mixed-field dosimetry.

Keywords: Radiation dosimetry, neutron, gamma, proportional counters

AUTHOR'S DECLARATION

I hereby declare that this thesis consists of original work of which I have authored. This is a true copy of the thesis, including any required final revisions, as accepted by my examiners.

I authorize the University of Ontario Institute of Technology (Ontario Tech University) to lend this thesis to other institutions or individuals for the purpose of scholarly research. I further authorize University of Ontario Institute of Technology (Ontario Tech University) to reproduce this thesis by photocopying or by other means, in total or in part, at the request of other institutions or individuals for the purpose of scholarly research. I understand that my thesis will be made electronically available to the public.

Faezeh Forouzan

STATEMENT OF CONTRIBUTIONS

I significantly contributed to the design of the experiments and executed a series of neutron gamma, mixed-radiation field experimental measurements performed at the radiation protection laboratory of Ontario Tech University, Oshawa, Canada and the Radiation Material Testing Laboratory (RMTL), Kingston, Canada. The high energy neutron radiation field measurements reported in this thesis were conducted by Dr. Anthony Waker and Dr. Gloria Orchard at the CERN-EU high-energy Reference Field (CERF) facility, Geneva, Switzerland.

I was responsible for the analysis of all the experimental data collected in different experiments, including the raw experimental data collected at the CERF facility, and I independently wrote the MATLAB scripts and carried out all analysis and calculations described and presented in this thesis. I also created and executed all the PHITS codes for simulating the counters, which were later compared to the experimental results. This contribution included an extension of the PHITS simulation process hitherto used in the former Faculty of Energy Systems and Nuclear Science at Ontario Tech by incorporation of experimentally determined and reported neutron energy spectra.

I hereby certify that I am the sole author of this thesis and I have used standard referencing practices to acknowledge ideas, research techniques, or other materials that belong to others.

Part of the work described in Chapter 5 has been published as:

Forouzan, F. and A. J. Waker (2018). "Development of heterogeneous proportional counters for neutron dosimetry." Radiation Protection Dosimetry 180(1-4): 168-171. doi:10.1093/rpd/ncx291.

Some other parts were also presented at the University Network of Excellence in Nuclear Engineering (UNENE) annual meetings.

I carried out all the measurements, computational simulations, data analysis and writing of this thesis under the supervision of Prof. Anthony Waker.

DEDICATION

To my dear parents, Enayatollah and Fatemeh, who have always provided me with unconditional love, support, and guidance throughout my life's journey.

To my inspiring and enlightening teachers, Mrs. Ameneh Eskandani, Mr. Majid Atighi, the late Prof. Farhad Rahimi, the late Prof. Rahim Koohi, and Prof. Anthony Waker, who brought the wonders of physics and radiation science to life and guided me on my path.

To my devoted spouse, Yasin, who acts as my trusted advisor, and has been my rock through thick and thin.

And to our beloved son, Omid, who brings hope and happiness to our life.

ACKNOWLEDGEMENTS

I am deeply grateful for the opportunity to express my sincerest appreciation to all those who have supported me throughout my PhD journey.

I would like to extend my heartfelt gratitude to my research supervisor, Professor Anthony Waker, for his unwavering guidance, support, and encouragement throughout my research. His insightful advice, mentorship, and wisdom have been invaluable in shaping my academic and professional development. During my life challenges, he offered me immense kindness and understanding, for which I am truly thankful.

I am grateful to Professor Kirk Atkinson for kindly stepping in as my supervisor after Professor Waker's retirement. I am also thankful for my committee members, Professor Edward Waller and Professor Glenn Harvel, and the referees of my defense exam, Dr. Malcolm McEwen and Dr. James Gräfe, who offered valuable insights and constructive criticisms that helped me enhance my work.

I would also like to express my sincere gratitude to the former postdoctoral fellow of our research group, Dr. Gloria Orchard, for her mentorship and support during my research.

Additionally, I am grateful to Dr. Fawaz Ali for his companionship and help in getting me up to speed with the PHITS code, and to Sarah Watt for her aid in putting together the digital pulse processors and making them operational.

Robert Ulrich and Callan Brown have been fantastic lab technicians, providing technical support and ensuring our lab ran smoothly. Michelle Cholak and Robin Secord have been excellent secretaries, providing administrative support and ensuring everything was organized and in order.

I thank the University Network of Excellence in Nuclear Engineering (UNENE) and the Natural Sciences and Engineering Research Council (NSERC) for their funding to support this research.

Finally, I would like to express my love and gratitude to my parents, my husband, my siblings and friends, for their continual support and encouragement during my academic pursuits. I cannot express enough gratitude to all those who have helped me in this journey. Your support has been invaluable, and I would not have been able to do it without you.

Table of Contents

List of Figures

List of Tables

Chapter 1

Introduction

Nuclear power plants, electron accelerators, and cosmic rays are all sources of mixed neutron gamma radiation fields. This can be said for almost everywhere that neutrons are produced. The reason behind it is the presence of hydrogen in many materials, and neutron interactions with hydrogen. Since the hydrogen nucleus has only one proton whose mass is almost the same as the mass of a neutron, a fast incident neutron can impart up to all of its energy, through elastic scattering, to the hydrogen nucleon and become thermalized. Some of these thermal neutrons will then be captured by other hydrogen nuclei in the interaction of $^{1}H(n,\gamma)^{2}H$. As a result of the neutron capture, a high-energy photon with energy of 2.22 MeV is released. This photon carries away the excess energy and provides the binding energy required for the formation of a deuteron (^{2}H), which is a nucleus consisting of a proton and a neutron. Other neutron interactions with matter can also result in gamma emission (Turner, 2005). Consequently, neutron radiation is always accompanied by gamma rays.

Although both neutrons and photons are neutral particles, they interact with matter differently. This is particularly important when their interaction with human tissue is concerned. The main component elements of human tissue are hydrogen, nitrogen, carbon and oxygen. When captured by these nuclei, thermal neutrons may produce gamma rays or energetic protons mainly through $^{1}H(n,\gamma)^{2}H$ and $^{14}N(n,p)^{14}C$ interactions (Turner, 2005). Fast neutrons, however, predominantly undergo elastic scattering with the atomic nuclei. In these interactions, neutrons impart all or a part of their kinetic energy to the target nucleus. The less massive the atomic nucleus, the more energy can be imparted to it. Among the

constituent elements of tissue, hydrogen has the lightest nucleus consisting of only one proton with almost the same mass as of a neutron. Therefore, an incident neutron can impart all of its kinetic energy to the hydrogen nucleus in an elastic scattering (Turner, 2005). The energy that can be transferred to a nucleus can be found from the following equation (Knoll, 2010):

$$\Delta E = E_n - E_R = En\,(1 - \frac{4A}{(1+A)^2}\cos^2\theta) \qquad (1.1)$$

In this equation, E_n is the kinetic energy of the incoming neutron, E_R is the kinetic energy of the recoil nucleus, A is mass of target nucleus/neutron mass, and θ is the scattering angle of the recoil nucleus in the lab coordinate system.

In the case of neutron elastic scattering with Hydrogen, A is equal to 1 and

$$\Delta E = E_n - E_R = En\,(1 - \cos^2\theta) = E_n(\sin^2\theta) \qquad (1.2)$$

Therefore, since the average value of $\sin^2\theta$ is equal to $\frac{1}{2}$, the average energy transfer in the elastic scattering of neutron from H, is $\frac{E_n}{2}$.

Interactions such as ^{12}C(n,α), ^{14}N(n,α), and ^{16}O(n,α) are also possible for fast neutrons when they are captured by the four aforementioned elements and result in emission of heavier charged particles such as alpha particles (Auxier, Snyder, & Jones, 1968).

On the other hand, photons, based on their energy and the atomic number (Z) of the target material, interact with matter through three main interactions: photoelectric, Compton scattering and pair production. Photoelectric absorption is the predominant interaction for

low energy gamma rays and results in a secondary electron (photo-electron). The energy of the photoelectron is given by:

$$E_{e^-} = h\nu - E_b \tag{1.3}$$

in which, E_b represents the binding energy of the photoelectron in its original shell, h is Planck's constant and ν is the frequency of the incident photon. The majority of the initial photon energy is carried away by the photoelectron when dealing with gamma ray energies exceeding a few hundred keV. The photoelectric process is enhanced by high atomic number materials. Although there is no single analytic expression to describe the probability of photoelectric absorption per atom for all energy ranges and atomic numbers, a rough approximation suggests that it varies as a constant multiplied by $\frac{Z^n}{E_\gamma{}^{3.5}}$, where n ranges between 4 and 5 for gamma rays. The dependence on atomic number is a key factor for the preference of high-Z materials in photoelectric absorption (Knoll, 2010).

Higher energy gamma rays, typically with the energy of radioisotope sources, mainly undergo Compton scattering and transfer a fraction of their energy to an atomic electron which leaves the atom and continue its way through the matter. The probability of Compton scattering per atom increases linearly with the atomic number Z because it depends on the number of electrons available as scattering targets.

If the gamma-ray energy exceeds twice the rest-mass energy of an electron (1.02 MeV), pair production becomes energetically possible. (Evans, 1968). Although the probability for pair production is small for gamma-ray energies only slightly above the threshold, it becomes significant as the energy increases into the many-MeV range. During pair production, the

gamma-ray photon is converted into an electron-positron pair, with the excess energy becoming kinetic energy shared by the particles. There is no simple expression for the probability of pair production per nucleus, but its magnitude is approximately proportional to the square of the atomic number of the absorber (Knoll, 2010).

Therefore, the main outcome of neutrons interacting with matter is the production of protons and heavier charged particles, while gamma photons mainly produce electrons. Since these secondary charged particles have different masses and different charges, they transfer different amounts of energy to the surrounding atoms with which they interact through the Coulomb force. In the human body, the energy deposition of these secondary particles may create biological damage to living cells. The greater the amount of imparted energy to tissue cells, the more serious the damage will be. Therefore, it is of great importance to correctly identify the incident radiation in order to provide appropriate safety solutions for people who work in areas exposed to neutron-gamma (n-γ) mixed radiation fields.

In radiation protection science, a system of quantities and units such as absorbed dose and dose equivalent has been developed to quantify the amount of energy deposited by radiation in the human body. According to report 103 of the International Commission on Radiological Protection, absorbed dose is the ratio of the mean energy imparted by ionizing radiation ($d\bar{\varepsilon}$) to matter of mass dm (ICRP103, 2007), (ICRU_Report95, 2017). However, different particles, even with the same amount of energy, have different interactions with human tissue. As such, ICRP introduces the concept of quality factor (Q) for each type of radiation at a specific point in tissue and defines dose equivalent (H) as the product of the quality factor of the radiation and the absorbed dose. This system works well for taking into account

the biological effectiveness and the damages that the individual radiations may cause to human body. However, when dealing with complex radiation fields, it becomes difficult to distinguish between the components of the radiation field and also to identify the dose deposited by each of them. Amongst these complex fields, neutron gamma mixed-fields are the most common and at the same time the most complicated fields to be monitored. Because both neutrons and photons are neutral particles there is no direct way to distinguish one against the other in a mixed-field. This is why mixed-field dosimetry has found great importance in radiation protection science and considerable efforts have been made to invent useful methods to deal with it.

1.1 Current Practice in Neutron-Gamma Mixed Field Dosimetry

The International Commission on Radiological Units and Measurements (ICRU_Report26, 1977) recommends that two separate dosimeters with distinct sensitivities to the two component radiations, such as neutron and gamma rays, in a mixed field are used for mixed field dosimetry. Unfortunately, neutron monitoring devices, such as moderator sphere thermal neutron detectors (REMballs), which has almost zero sensitivity to photons, have a very poor response over the entire energy-range required in radiation protection. Devices which do have a good neutron energy response, such as ionization chambers, are however, equally sensitive to photons. Therefore, neutron dosimetry in radiation protection energy-range is not possible with a single device. The most common idea for neutron gamma mixed-field dosimetry is subtracting the gamma dose from the measured neutron-gamma mixed-field dose. The first implementation of this idea was based on using the combination of two ionization chambers which is known as the “twin chambers technique”. In this method, one

of the chambers has a hydrogenous wall and gas to measure the n-γ dose. The second chamber wall is made up of materials which have (almost) no sensitivity to neutrons. Carbon and magnesium are examples of the materials that are used, because of their very low cross sections for neutron interactions. The cavity of these chambers can also be filled with gases such as carbon dioxide (Delafield, Holt, & Boot, 1976) or Argon (Stinchcomb, Kuchnir, & Skaggs, 1980) which are not sensitive to neutron radiation. For obtaining the gamma and neutron dose with the twin chamber technique, a set of two standard equations (National Bureau of Standards Gaithersburg MD; G. S. Hurst, 1961), which relates the chamber reading, R, to the gamma and neutron dose, Γ and N, should be solved:

$$R_t = A_t(\Gamma + k_t N) \tag{1.4}$$

$$R_u = A_u(\Gamma + k_u N) \tag{1.5}$$

In the above equations, the subscript *t* and *u* respectively refer to the tissue equivalent chamber, and the other chamber which is not sensitive to neutrons. *A* denotes the gamma sensitivity of the chamber and *k* indicates the neutron sensitivity of the chamber which is normalized to the gamma sensitivity of the chamber for practical purposes. While the gamma sensitivity of the ion chamber is measurable using a well-known gamma source, such as ^{60}Co, determination of the response of these chambers to neutrons is a challenging problem and requires special experimental facilities and methods to be stablished (Stinchcomb et al., 1980). By inserting the two chambers readings, R_t and R_u, and the experimentally measured quantities A_t, A_u, k_t and k_u in equations (1.4) and (1.5), the gamma and neutron dose in mixed-field can be obtained. Although this technique is theoretically effective in the mixed-

field dosimetry, the ion chambers have some restrictive characteristics for this purpose. These chambers are the simplest type of gaseous (gas-filled) detectors. They operate mainly in current mode based on collecting all the charges created by direct ionization of the gas inside their cavity due to the interactions of radiation with the walls and cavity gas (Knoll, 2010). These dosimeters have been used for a long time and are still in used for area monitoring. However, due to relatively low electric field strength in the ionization chambers, they do not have the multiplication effect to amplify the original ion-current charge created inside their cavity. Therefore, the number of ion pairs created by the radiation should be high enough to be recorded by these chambers. The problem is that this is not always applicable. The other problem with these detectors is their operation in current mode which means that the output signal is a continuous current produced by the whole charge collected at the anode of the counter. Therefore, these chambers are not capable of showing the energy spectrum of the ionizing radiation that came into the sensitive volume. Consequently, they are not the best devices to discriminate between the radiation types. Furthermore, ionization chambers cannot provide a means of determining a quality factor for a given field and the determination of the dose-equivalent.

To resolve these problems a group of researchers recommended low pressure Tissue Equivalent Proportional Counters (TEPCs) which make possible the microdosimetric event-size measurements for neutron-gamma dose separation in a mixed-field (Stinchcomb et al., 1980). Both the wall and the fill gas of the TEPCs are made of tissue equivalent materials, so that these counters simulate micron-sized volumes in tissue. When the incident radiation interacts with the wall of the counter, secondary charged particles are created which then

enter the gas cavity. Using pulse processing electronics, TEPCs record the energy deposition of every secondary charged particle interacting with the gas molecules. The output then provides frequency distributions of the individual stochastic energy deposition events (event-size spectrum) occurring in a microscopic volume. N-γ mixed field dosimetry is possible using TEPCs by fitting and then subtracting a photon event-size spectrum (Figure 1-1).

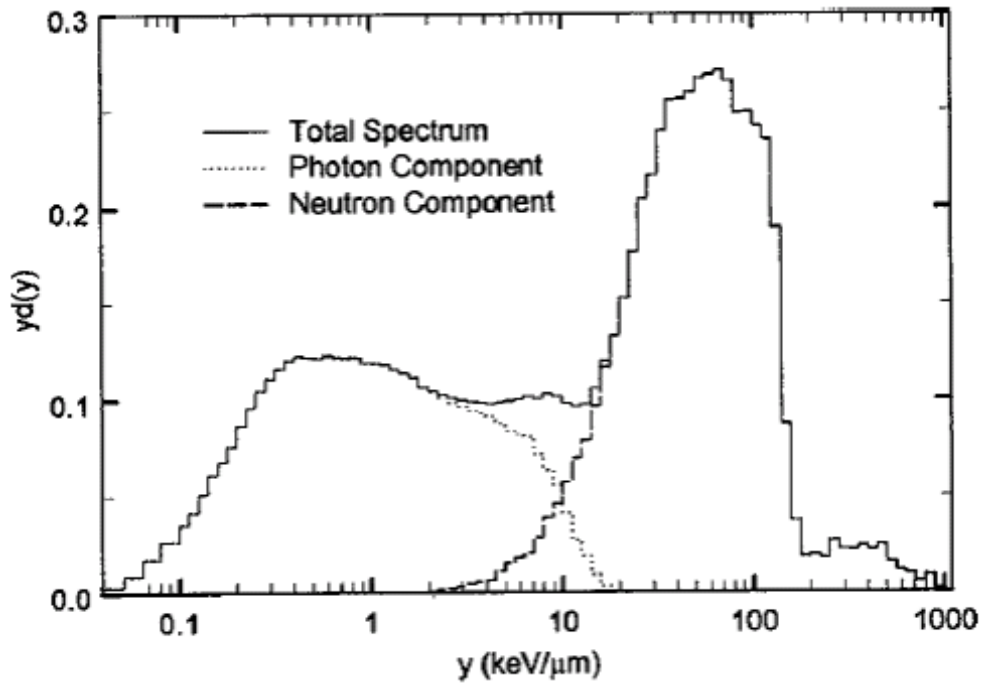

Figure 1-1 Total, gamma, and neutron lineal energy spectra for Cf-252 measured with a 12.3 mm3 TEPC for simulated site diameter of 1 μm at a depth of 5 cm in water (Burmeister, Kota, Maughan, & Waker, 2001)

This method has been applied in practical radiation protection dosimetry for some time. However, this approach falls short in several respects: *First*, although the applicable voltage range of TEPCs is wider than of the ionization chambers, TEPCs are limited in terms of high voltage that can be applied to the counter anode. Hence, the gas-gain of the counter that can

be achieved is limited and standard commercially available TEPCs used in radiation protection can only measure part of the gamma ray event-size spectrum. *Second*, the shape of gamma event-size spectrum generally depends on the gamma ray energy. However, in an unknown field, the shape of the gamma component is not known. In this situation, fitting an arbitrary photon spectrum is not adequate. *Finally*, TEPCs are sensitive to both gamma and neutron radiations. On the other hand, the photon component of the mixed field event size spectra does not always match completely with the primary fitted photon spectrum. Therefore, it is very important to find the exact contribution of neutrons and photons in the part of the spectrum that does not match the proposed photon spectrum. This process is usually feasible, because neutrons in general are detected with higher pulse heights than the photons. The reason is that the ionization density along the secondary charged particle tracks created by neutron radiation is more than the density of the ionizations in the secondary electron tracks produced by photons. However, the pulse height corresponding to photons and high energy neutrons are somewhat similar and therefore, there is an overlap between their fractions in the mixed-field event-size spectrum (Schrewe, Schuhmacher, Brede, & Dietze, 1990). This overlap may lead to uncertainties in neutron-gamma mixed field dosimetry.

1.2 Motivation of Research

To benefit from both the methods mentioned above and overcome the shortcomings, the idea of paired proportional counters has been proposed (DeLuca Jr, Schell, Pearson, & Attix, 1981). Such a set of counters contains a TEPC for measuring the neutron-gamma dose in the mixed-field plus a heterogeneous counter with a non-hydrogenous wall and filled with a

hydrogen-rich tissue equivalent gas similar to the TEPC for measuring the accurate gamma dose in the same field. Both counters are filled with the same tissue equivalent gas to mimic the interaction of the charged particles with human tissue. The wall of the counters however is different in such a way that the A-150 plastic wall allows both neutrons and photons to interact with the counter. On the other hand, the non-hydrogenous wall has a very low interaction probability with neutrons. Since both of these detectors have similar sensitivities to gamma radiation, the neutron dose spectrum is obtainable by subtracting the gamma spectrum measured by the heterogeneous counter from the mixed-field spectrum provided by the TEPC. Therefore, one can obtain the event size spectra of both gamma and neutron radiations as well as their absorbed dose in a tissue equivalent medium.

Mixed field dosimetry with a set of two separate proportional counters is an accurate but slightly time consuming process. This is due to the fact that the measurements should be taken one by one using both counters. Moreover, in real-life radiation fields, the situation of the radiation may change from time to time. This could happen for example if the physical conditions around the point of measurement have been changed between measurements, such as extra shielding put into place or modifications to the source by changes in reactor or accelerator output. In complex irradiation facilities for particle physics research other neighboring experiments can also affect radiation fields in a time variant manner. Therefore, the gamma component may not remain the same during the two measurements. This can be problematic if the assumption behind the method is that the gamma component of the mixed-field remains constant. In summary, combining a heterogeneous counter with a TEPC is a novel idea that can potentially be used in designing a single instrument capable of measuring

gamma and neutron dose at the same time in mixed radiation fields. An important contribution of this research will be an experimental verification of the method, which to date has only been investigated by computational means (Kyllönen & Lindborg, 2007) or experimentally in a very restricted neutron energy range (DeLuca Jr et al., 1981).

1.3 Research Objectives

The heterogeneous counter proposed in this research for applying the twin-counter idea was a Cylindrical Graphite Proportional Counter (Cy-GPC). The graphite wall of this counter is almost insensitive to neutrons. On the other hand, the wall shows almost the same level of sensitivity to gamma rays as does the wall of the Cylindrical Tissue Equivalent Proportional Counter (Cy-TEPC) made out of A-150 plastic. The research objective was to develop a design for concurrent use of this heterogeneous proportional counter along with a Cy-TEPC that can be used in neutron-gamma mixed field dosimetry. Two phases were deemed necessary to accomplish the goals of this research: 1- experimental measurements, and 2- computational simulations.

The following steps were designed and followed through for the experimental phase of the study:

Firstly, it was necessary to confirm that the heterogeneous counter and the TEPC show the same level of sensitivity to photons while exhibiting a very different response to neutrons. Consequently, as the first step, the equivalence of the gamma dose measurements between the Cy-GPC and its geometrically identical Cy-TEPC was investigated over a wide range of photon energies (form~20keV to ~1MeV). The reason for considering this wide range of

photon energies was that neutrons may have various capture and scattering interactions with matter, and as such, the resulting photons have a broad range of energy. For example, the photons which are emitted from an Am-Be neutron source have an energy of 60 keV, whereas, the energy of the gamma rays produced in thermal neutron absorption by hydrogen nuclei, ^{1}H (n,γ) ^{2}H, is ~2.2 MeV. In order to make a comparison between the photon responses of the two counters, three quasi-monoenergetic X-Rays with different energies and high energy gamma rays from Cs-137 were measured with both counters. Moreover, an A4-ionization chamber (Standard Imaging Co.) which is calibrated for gamma radiations was used as a benchmark to verify the operation of these two counters in photon dosimetry.

Once it was confirmed that the Cy-GPC and the Cy-TEPC similarly measure the photon dose, their response to neutron radiation was studied in pure neutron fields. For this purpose, the P-385 neutron generator at the Ontario Tech University radiation facilities was covered with a $\frac{1}{4}$ inch (6.35 mm) thick lead shield to block accompanying X-Ray radiation from the target and let the neutrons pass. These neutrons were then measured by the Cy-TEPC, the Cy-GPC and a 5" spherical TEPC as a benchmark to confirm that the Cy-GPC is almost non-sensitive to neutrons (in contrast to the Cy-TEPC and the 5" TEPC which measured a similar neutron dose).

In the second step of the experiments, the counters were exposed to the mixed radiation field of 2.5 MeV neutrons and Cs-137 Gamma rays. The use of this mixed-field measurement was necessary to confirm that the twin-counter set-up measures both the neutron and gamma

components, with good accuracy, when compared to the pure neutron and gamma radiations, where they were previously used.

Since the operation of the counters needed to be ascertained for a wide range of neutrons and photons, various mixed-field radiations were measured with these counters in the third step, including an ^{241}Am-Be radiation field, the radiation fields produced at the Queen's University Radiation Material Testing Laboratory (RMTL) accelerator and the CERN high energy reference field facility. These fields mainly consist of broad energy range of neutrons accompanied by significant photon fields. The neutron dose rate spectrum and the total neutron dose rate in each case were obtained by subtracting the gamma measurement of the Cy-GPC from the mixed radiation measurement of the Cy-TEPC.

In parallel to experimental characterization in phase I, Monte Carlo simulations were conducted for the phase II of this study. This helps to understand and predict the response of the twin counters to mixed-fields, and optimize the design of future devices. Comparison with experimental results also establishes confidence in the simulation methods themselves. Monte Carlo can also allow the response of the two counters to be investigated in radiation fields for which experimental data may not be available. For this purpose, the Particle and Heavy Ion Transport code System (PHITS) was chosen as the simulation tool. The geometry of the counters, the characterization of the radiation, and the setup of each experiment were defined for this code. The code analyzed the particles transport in the gas cavity, and provided the absorbed dose distribution deposited in the counter using the nuclear reaction models of the secondary charged particles provided in its data libraries.

The final step of this research was the performance assessment of the counters in mixed field dosimetry and making a plan for future works and developments towards designing a single device for this purpose.

The aforementioned experimental dosimetry and theoretical methods were all built upon microdosimetric concepts. The theoretical background of microdosimetry as well as its application in dosimetry is introduced in the next chapter.

Chapter 2

Experimental and Computational Methodologies

The definition of absorbed dose as the mean deposited energy divided by the mass of the exposed volume works well in the macroscopic world. However, when biological damages due to ionizing radiation are concerned, the mesoscopic world of cells and sub-cellular entities becomes of concern. On this scale, neither the medium nor the radiation can be considered continuous. Ionizing radiations interact with matter in different methods and create charged particles as a result. In a micro-scale volume of tissue, the secondary charged particles encounter an enormous number of interaction points to which they may interact and transfer their energy in less than a femtosecond. Moreover, the radiation emission itself may vary with direction and time. In conclusion, there are various values possible for the energy deposit, ε, at each point in the tissue. Therefore, the interaction of radiation with tissue cells is a stochastic phenomenon and should be studied at microscopic levels (Zaider & Rossi, 1996) and (Greening, 1985). Stochastic dosimetry, now generally called microdosimetry, was introduced by radiation scientists to stablish a correlation between the principle features of the ionizing radiation absorption in matter and the size and nature of the affected structures (ICRU_report36, 1983).

Simply put, microdosimetry can be thought of as the measurement of absorbed dose on microscopic scale as the summation of individual stochastic events within a given volume. To accomplish this purpose, microdosimetry defines a systematic methodology for

quantifying the distribution of absorbed energy in matter in terms of both space and time (Zaider & Rossi, 1996).

The determining factor in analyzing the radiation behavior in matter is the pattern of the radiation interactions with atoms. Consequently, the methodology of microdosimetry is based on defining the concepts and measuring the physical quantities that leads to an informative picture of the radiation interaction pattern rather than only measuring the mean values of quantities provided by conventional dosimetry.

Two types of formulations have been developed for implementing microdosimetry. The first one known as regional microdosimetry is based on the assumption that the medium is a collection of distinct micron-sized regions. Since these sites have very small sizes, the absorbed energy from the ionizing radiation to these regions is considered without accounting for the microscopic energy distribution inside them. This picture is mainly used in experimental dosimetry and mechanisms of radiation biological damage, because it represents measurable concepts for studying radiation effects in matter. The other formulation, which is more complicated and mainly attractive to theoretical microdosimetry, focuses more on the pattern of the energy deposition through charged particle tracks inside the matter. Structural microdosimetry deals with the study of junctions of the abovementioned pattern with the sensitive components of the matter to determine the initial impact of radiation on matter. While theoretical methods are of more importance in studying fundamental concepts of radiation interaction with matter through structural microdosimetry, experimental approaches which try to measure microdosimetric quantities, rely on regional microdosimetry (Zaider & Rossi, 1996). The great importance of experimental

microdosimetry is reflected in radiobiology and radiation protection sciences where a reliable method is needed for radiation dosimetry in tissue and live organs. Generally speaking, classical microdosimetry is a combination of accurate dose measurement and spectroscopic capability, making it useful for advanced radiation metrology, code verification, and radiation field analysis. It is also the best option for neutron monitoring and personal neutron dosimetry. However, the complexity of microdosimetric instrumentation and data systems presents a challenge for routine use in health physics (A. Waker, Schrewe, Burmeister, Dubeau, & Surette, 2002).

2.1 Principles of experimental microdosimetry

There are so many methods and devices introduced for radiation detection and measuring the absorbed dose in matter. Among them, low pressure Tissue Equivalent Proportional Counters (TEPCs) are the most preferred devices in experimental microdosimetry.

TEPCs are effective in measuring absorbed dose and dose equivalent over a broad range of neutron energies. They offer advantages over other neutron dosimeters, including self-calibration, absolute dosimetry, determination of quality factors, and coverage of a wide range of neutron energies (Brackenbush, 1991).

Since invented in the 1960s, TEPCs have been used to measure the amount and distribution of ionizing radiation in a given environment. The theory behind TEPCs is based on the fact that ionizing radiation interacts with matter and deposits energy, leading to the formation of ionization tracks in the material.

These counters were invented to mimic the microscopic-size tissue volumes.Therefore, the atomic composition of the wall material and the fill gas of these counters are chosen to be very similar to the muscle tissue. The size of the tissue volume is also simulated by controlling the gas pressure. This allows the TEPC to provide a more accurate measurement of the biological effects of ionizing radiation than other types of detectors that do not mimic the interaction of radiation with human tissue. When ionizing radiation or the charged particles created as the interaction of neutrons and photons with the wall material enter the cavity, they interact with the gas molecules and produce secondary electrons, which ionize the gas molecules in their path. The movement of electrons and ions produced by the ionization events create a small voltage drop in the electrical field inside the cavity. This potential change is then detected and amplified by a pre-amplifier and signal processing electronics By measuring the electrical pulses coming from TEPCs the energy and number of ionization events caused by the radiation can be determined. This information can be used to calculate the dose of radiation absorbed by the tissue-equivalent material. As a result, TEPCs provide a very accurate estimation of the absorbed dose in the biological tissue.

TEPCs are widely used in radiation protection and radiation therapy to measure the dose and quality of radiation delivered to patients, as well as in research to study the effects of radiation on biological systems.

Following a suitable calibration, the distribution of absorbed dose in the gas cavity is given by the TEPC in terms of lineal energy, y, which itself is related to LET as discussed in

section 2.2. The fundamental operational principles of the TEPCs are reviewed in the next sections.

2.2 Microdosimetric quantities and parameters

The most basic quantity to be measured in investigating the radiation behaviour in matter is the amount of energy deposited by the radiation inside the matter. The quantity that conventional dosimetry suggests for this purpose is the absorbed dose which is defined as the mean value of imparted energy per unit mass of irradiated matter:

$$D = \frac{d\bar{\varepsilon}}{dm} \tag{2.1}$$

The energy deposited in matter is different from one point to the other, and averaging over all these values might be useful for some applications, but not for studying the radiation interaction with tissue. In this case, every individual event is important and should be considered. The main approach of experimental microdosimetry is to simulate the sensitive microscopic sites of the irradiated matter and measure stochastic quantities inside them (Al-Bayati, 2012).

In order to practice this approach, the first step is to suitably define measurable stochastic quantities. The stochastic quantity equivalent to the absorbed dose is called specific energy z. In order to define specific energy in microdosimetry, a microscopic volume V is imagined around the point of interest in the irradiated medium (or tissue), and the total energy ε imparted to this volume is measured. This imparted energy is the sum of the individual energy deposits through all the interaction events that occur in this volume:

$$\varepsilon = \sum \varepsilon_i \tag{2.2}$$

The energy deposited in each interaction is obtained from the following equation:

$$\varepsilon_i = T_{in} - T_{out} + \sum Q \tag{2.3}$$

Above, T_{in} and T_{out} are the energy of the ionizing particles entering and leaving the volume respectively, and $\sum Q$ is the sum of rest mass energies of the particles and atoms involved in the interactions. The specific energy is defined as the ratio of the imparted energy over the mass of the volume V (Al-Bayati, 2012):

$$z = \frac{\varepsilon}{m} = \frac{\varepsilon}{\rho V} \tag{2.4}$$

When a charged particle traverses a microscopic volume, V, it is of interest to know the amount of energy it loses through interacting with the atoms on its way rather than the amount of energy that it carries. The quantity that is defined around this concept is called Linear Energy Transfer (LET). LET is defined as "the mean energy lost in electric collision by a charged particle traversing the distance dx" (Zaider & Rossi, 1996). Since there are so many possible paths that a particle can pass through, it is impractical to find the LET by measuring the deposited energy of all the possible interactions that a charged particle might have in the microscopic volume, V. In order to work with a measurable quantity correlated to LET, lineal energy, y, is used in microdosimetry. This quantity is defined as the ratio of the imparted energy ε in one interaction event divided by the mean chord length of the volume V:

$$y = \frac{\varepsilon}{\bar{l}} \tag{2.5}$$

The mean chord length of the volume ($\bar{l}$) represents the mean value of all the straight distances that a particle may traverse across the volume V and is calculated based on Caushy's theorem (Kellerer, 1971b).

According to this definition, the lineal energy of every charged particle in volume V, is a unique value which depends only on the energy imparted by that particle. Therefore, finding the frequency distribution of the lineal energies, f(y), one can obtain a realistic picture of the energy distribution of the charged particles in the microscopic volume V.

The frequency mean lineal energy, which is the mean value of f(y) is calculated as follows:

$$\bar{y}_F = \frac{\int_0^\infty y.f(y)dy}{\int_0^\infty f(y)\,dy} \tag{2.6}$$

In practice, the lineal energy distribution function is discontinuous and the discrete summation can be applied in the following equation:

$$\bar{y}_F = \frac{\sum y.f(y)}{\sum f(y)} \tag{2.7}$$

Another function, which is very useful in illustrating the energy absorption pattern in the microscopic volume V, is the dose distribution *d(y)*. This function is defined as the normalized product of y and $f(y)$:

$$d(y) = y.f(y) \tag{2.8}$$

The relative contribution of every lineal energy event y to the total absorbed dose in volume V can be realised from this distribution. The mean value of this function, which is called the dose mean lineal energy, is also defined similar to equation (2.7):

$$\bar{y}_D = \frac{\sum y.d(y)}{\sum d(y)} = \frac{\sum y^2.f(y)}{\sum y.f(y)} \tag{2.9}$$

Both frequency mean lineal energy ($\bar{y}_F$) and dose mean lineal energy ($\bar{y}_D$) are important in understanding the biological effects of radiation on living tissue.

$\bar{y}_F$ represents the mean energy recorded by the counter from individual particle tracks and provides insight into the average energy deposited per unit length of track in a medium by ionizing radiation in a similar manner to the non-stochastic quantity track-averaged linear energy transfer (LET), which is often used to specify 'radiation quality' in radiation biology.

On the other hand, $\bar{y}_D$ represents the lineal energy that contributes the most, on average, to the absorbed dose delivered to the counter. It takes into account the energy deposited per unit length of track in a medium, weighted by the dose deposited by different types of particles producing the tracks. $\bar{y}_D$ helps calculate the dose equivalent and has been used to specify radiation quality for different types of radiation and their relative biological effectiveness.

The quantities reviewed in this section are used to provide a quantified interpretation of the radiation interaction with matter. In the next section the methodology of experimental microdosimetry is described for measuring the absorbed dose in a microscopic tissue volume exposed to a radiation field.

2.2.1 TEPCs operational principles

TEPCs, like other proportional counters, measure the voltage drop between cathode and anode which occurs as a result of the collection of electrons at the anode resulting from ionization within the gas cavity. An electric field is applied between the anode wire and the cathode, which is usually the wall of the counter. Consequently, the free electrons and the positive charged ions of the ion pairs drift in opposite directions towards the anode and the cathode respectively. In its drift towards the anode, provided the electric field is strong enough, each electron can gain sufficient kinetic energy to cause further ionizations in the counting gaz. This multiplication in the number of electrons usually takes place close to the anode wire where the electric field is sufficiently high. As a result, the number of electrons which are collected at the anode is proportionally a few orders of magnitude higher than the number of electrons initially created by the radiation interactions in the counter. This multiplication effect is known as the gas gain which is an important specification of the gas inside the counter.

Many explanations of the process of gas amplification can be found in the literature (Knoll, 2010).

The actual gas gain value of a TEPC is not an absolute requirement for conducting experimental microdosimetry, as can be inferred from the Pulse Height Analysis (PHA) method used for TEPC calibration. (Lindborg & Waker, 2017). Nonetheless, it is helpful to have a basic comprehension of the multiplication process and how it is influenced by various factors particularly the applied cathode-anode voltage. In a cylindrical electric field there is a

logarithmic proportionality to the voltage (V) applied between the anode and the cathode (Lindborg & Waker, 2017)

$$\ln G = \frac{AV}{Bln\frac{c}{a}}\left[e^{-aP\frac{Bln\frac{c}{a}}{V}} - e^{-cP\frac{Bln\frac{c}{a}}{V}}\right] \tag{2.10}$$

In this equation, P is the gas pressure inside the cavity. A and B are gas specific constants, which have been approximated for methane-based and propane-based gases by Campion and Waker respectively (Campion, 1971), (A. Waker, 1983). A is proportional to the reciprocal of the mean free path in a gas at a given pressure and B is related to the ionization potential of the molecules in the counting gas. Parameters *a* and *c* are the anode and cathode radii respectively. Ideally the electron avalanche is confined to a very narrow volume around the anode wire and as *c* is usually much larger than *a,* the second term in the bracket can be ignored. After expansion of a series the equation then simplifies to:

$$\ln G \approx \frac{AV}{Bln\frac{c}{a}}\left[\frac{c}{a}\right]^{\frac{-aBP}{V}} \tag{2.11}$$

According to this equation and based on experimental verification, the gas gain of a TEPC depends on several factors, including the gas mixture used in the detector, the gas pressure, the voltage applied and the geometry of the detector. From equation (2.13) increasing the voltage increases the signal amplification logarithmically and will improve the sensitivity of the detector in terms of the lowest energy depositing events that can be detected. However, the voltage must be carefully controlled to avoid damaging the detector or distorting the signal by driving the counter in Geiger-counter mode of operation or electrical discharge.

The pressure of the gas determines the avalanche zone in the gas cavity. As the gas pressure inside the counter is decreased, the multiplication zone extends toward the cathode (A. Waker, 1983). This factor puts some limitations to the site size that can be simulated and the resolution of the counter.

As a result of the electron multiplication, an electron avalanche is collected at the anode, and therefore, a temporary voltage drop is created between the anode and the cathode. This voltage drop is converted into an electric pulse by a charge sensitive preamplifier with the height of the pulse being proportional to the energy released due to the initial interaction and ionization of the counting gas. When the gas gain of the counter is increased, more electron multiplication occurs and the resulting pulse will be stronger which makes the detection of smaller energy deposition events easier. The pulse from the preamplifier is further shaped and amplified for the pulse height analyser or multi-channel analyser, which determines the height of each pulse created by an energy deposition event. In this manner a spectrum of pulse-heights is accumulated and through the calibration process of the TEPC converted into a spectrum of single energy deposition events. TEPCs are used to record radiation energy deposition in microscopic volumes of unit density tissue. For this purpose, TEPCs must simulate both the dimensions and the atomic composition of tissue. The next two sections indicate the implementation of these requirements.

2.2.2 Site Size simulation in TEPCs

In order to simulate a unit density microscopic tissue volume with a TEPC, the key principle is that the energy measured in the gas cavity of the counter (E_g) should be the same as the deposited energy in the tissue volume (E_t). Therefore:

$$E_g = E_t \tag{2.12}$$

The deposited energy by a charged particle is defined as the product of the mass stopping power of that particle, the density of the site's consisting material and the distance that the particle traverses in the site (i.e. the path length across the volume). Therefore, equation (2.12) is rewritten as:

$$\left(\frac{1}{\rho_g}\left(-\frac{dE}{dx}\right)_g\right).\rho_g.\Delta x_g = \left(\frac{1}{\rho_t}\left(-\frac{dE}{dx}\right)_t\right).\rho_t.\Delta x_t \tag{2.13}$$

In this equation, $\left(\frac{1}{\rho_g}\left(-\frac{dE}{dx}\right)_g\right)$ is the mass stopping power of the ionizing particle in the gas and $\left(\frac{1}{\rho_t}\left(-\frac{dE}{dx}\right)_t\right)$ is the same particle's mass stopping power in the tissue site. Since the gas inside the counter is tissue equivalent, it has the same atomic composition as tissue has, but with different density. The mass stopping power is independent of density and depends only on the atomic composition of the target material, which means:

$$\left(\frac{1}{\rho_g}\left(-\frac{dE}{dx}\right)_g\right) = \left(\frac{1}{\rho_t}\left(-\frac{dE}{dx}\right)_t\right) \tag{2.14}$$

Therefore, the tissue equivalent gas inside the counter has the same mass stopping power as the tissue has. Equation (2.13) can thus be written as follows:

$$\rho_g . \Delta x_g = \rho_t . \Delta x_t \tag{2.15}$$

The geometry of the tissue equivalent site is assumed the same as the simulated tissue site with a specific dimension ratio. Therefore, the path length that a particle traverses across the volume can be assumed as any arbitrary path in the volume as far as it is identical (alike) in the two corresponding sites. The simplest dimension to be assumed as the path length across the volume is the diameter, which is a known value for both the tissue volume and the counter cavity (Figure 2-1):

$$\Delta x_t = d_t, \Delta x_g = d_g \tag{2.16}$$

The tissue is also assumed ideal with unit density ($\rho_t = 1$). Therefore, the density of the gas to simulate the tissue site is obtained from equation (2.15):

$$\rho_g = \frac{d_t}{d_g} \tag{2.17}$$

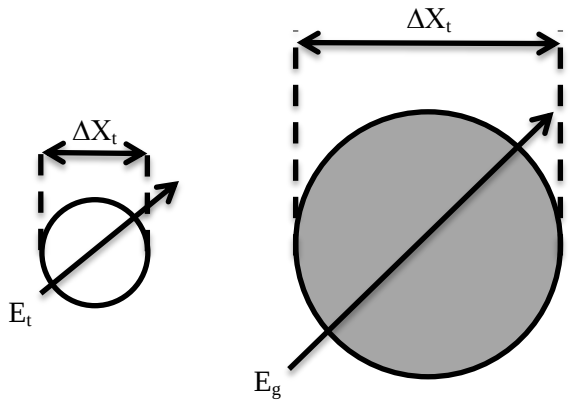

Figure 2-1 Microscopic tissue site simulation in TEPCs

On the other hand, based on the ideal gas law, the pressure of the gas is related to the density. According to this law, the product of the gas pressure (P) and the volume of the gas container (V), divided by the gas temperature (T), is equal to a constant value:

$$\frac{P.V}{T} = n.R \tag{2.18}$$

In this equation, R is the ideal gas constant and has a value of 8.314 ($J \cdot K^{-1} \cdot mol^{-1}$). n is the number of moles per unit volume of the gas and is equal to the mass (m) divided by the molar mass of the gas (M). The atomic composition of the gas is specified, so the value of the gas molar mass (M) can be calculated. Since the mass of the gas is the product of volume and density, n is related to the gas density as follows:

$$n = \frac{m}{M} = \frac{\rho V}{M} \tag{2.19}$$

By replacing the molar density (n) in equation (2.18) with this formula, the relationship between the pressure and the density of the gas is obtained:

$$P_g = \frac{\rho_g}{M_g}.R.T_g \tag{2.20}$$

If in this equation, ρ is replaced by equation (2.17), the following relationship is obtained for the desired value of the gas pressure inside the counter in terms of the specifications of the gas and the simulated tissue site (Al-Bayati, 2012):

$$P_g = \frac{R}{M_g}.\frac{T_g}{d_g}.d_t \tag{2.21}$$

Thus, the tissue site size can be simulated by applying the appropriate pressure to the gas inside the cavity. The next TEPC design requirement is to find a tissue equivalent atomic composition for the gas and the wall material of the TEPC.

2.2.3 Tissue equivalence in TEPCs

The human muscle tissue mainly consists of hydrogen, carbon, nitrogen and oxygen. The ICRU introduced a standard muscle tissue atomic composition of these four elements (ICRU_Report10b, 1964). This composition, whose elemental details are shown in Table 2-1, is referred as the main standard in designing tissue equivalent composite. The most appropriate material that has been applied as the wall of the TEPCs so far is A-150 Shonka plastic. The combination of this plastic is very similar to the ICRU tissue standard, except that A-150 has less oxygen and more carbon percentages. The reason for this difference is that the wall of the TEPC plays also the role of cathode in the electrical field inside the counter, and thus, it should be made up of a conductive material. By applying more carbon in the combination of wall material, it becomes conductive and ideal to be used in the counter wall. Furthermore, the cross sections of neutron and gamma radiation interaction with carbon and oxygen are very similar, at least for energies up to about 15 MeV for neutrons. Therefore, by replacing some oxygen atoms with carbons, the performance of the wall material for neutron and gamma radiation detection does not change perceptibly. The atomic composition of A-150 Shonka plastic is also shown in Table 2-1.

The A-150 material contains a significant amount of nylon, which has a hygroscopic nature. As a result, the A-150 can absorb moisture from the air, potentially increasing its weight by

up to approximately 10% due to the content of water vapor. Consequently, it is crucial to perform outgassing on the detector before it is filled with a TE (Tissue-Equivalent) gas (Lindborg & Waker, 2017).

The thickness of the wall is another important factor that should be considered in designing the counter wall. The wall thickness of the TEPC affects the energy deposition and scattering of secondary protons and particles within the detector. Thicker walls generally result in increased energy loss and scattering of these particles as they pass through the TEPC. This can lead to modifications in the measured spectrum, particularly at lower energies. With thicker walls, more secondary particles may undergo energy loss and scattering interactions, resulting in a broadening or redistribution of the particle energy spectrum. This can make it challenging to accurately determine the original energy distribution of the incident particles. Conversely, thinner TEPC walls allow for less energy loss and scattering, which can result in a more faithful representation of the primary particle spectrum. Therefore, the selection of TEPC wall thickness should be carefully considered to ensure that the measured secondary proton/particle spectrum accurately represents the incident particle spectrum of interest. The wall thickness must be at least equal to the range of the most energetic charged particle produced by the incident radiation. In this situation, the charged particle equilibrium condition is met and the flux of secondary particles leaving the inner side of the wall is independent of the wall thickness (Knoll, 2010). However, the wall must not be too thick to cause considerable attenuation to the radiation flux. In addition to the wall material, the gas inside the counter should also be tissue equivalent. There are two most well-known choices produced for this purpose. One of them is created based on Methane gas and the other which has a higher gain is Propane-based. The elemental composition of these two gases is also compared in Table 2-1.

Before using a counter in measurements, it is necessary to do some preparations for the experimental set up.

Table 2-1 Atomic composition of tissue equivalent materials (ICRU_Report26, 1977)

Material	Percent Elemental Weight				
	Hydrogen	Carbon	Oxygen	Nitrogen	Other
ICRU Muscle Tissue	10.2	12.3	72.9	3.5	1
A-150 Shonka Plastic	10.1	77.6	5.2	3.5	1.7
Methane Based Tissue Equivalent gas	10.2	45.6	40.7	3.5	-
Propane Based Tissue Equivalent gas	10.3	56.9	29.3	3.5	-

Chapter 3

Literature Review

The twin-proportional counters method has been studied in a limited experimental and computational scope, as it was primarily developed to improve the precision of neutron dosimetry used in neutron therapy. Neutron therapy was initially introduced in 1938 and early studies showed promise, but severe late side effects resulted in its closure and loss of interest in the method. Although neutron therapy was reintroduced in the late 1960s with some encouraging results, it also resulted in more frequent and severe complications, making the advantage of neutrons controversial. Consequently, research on the twin counter method has been limited due to the lack of research conducted in this area. Nevertheless, the need for accurate neutron dosimetry in other neutron-gamma mixed radiation fields still exists, and the twin counter method is worth further investigation. Therefore, this study draws inspiration from the few available studies on the subject to advance the twin counter method.

3.1 Survey of experimental methods used in neutron-gamma mixed field dosimetry

Delafield, Holt, and Boot used a pair of ionization chambers for dose measurement in monoenergetic neutron fields, with energies of 0.67, 2.1, 5.5 and 15.5 MeV, and also for 252Cf neutron source (Delafield et al., 1976). Both the ionization chambers had the same geometrical details. However, one of them was homogeneous, its walls and electrodes were made out of conducting plastic (CnHn) and filled with acetylene gas, and the other one, which was insensitive to neutrons, had a graphite wall and filled with carbon dioxide. Both

chambers had a collection volume of about 5 cm^3 and were working with a continuous flow of gas. The chamber with hydrogenous wall and gas was supposed to measure the dose deposited by both neutrons and photons, while the chamber with carbon wall measured only the gamma dose. For the gamma ray measurements, the ionization chambers were calibrated against a collimated Cs-137 source. The measurements were conducted at a 1m distance from the source resulting in an exposure rate of ~9 R/h. The graphite chamber calibration was obtained from a measurement with the chamber filled with air. The ratio of CO_2 response to air response was then determined for this chamber.

Monoenergetic neutron measurements were conducted for a time range of 30-60 min in the fields produced by a 3MV Van de Graf accelerator, above a deep pit. A set of detectors containing a tissue equivalent ionization chamber, a fission chamber, a GM counter and other moderated counters were used to monitor the neutron beam. In the measurements the distance of the CH ionization chamber from the surface of the target was 30 cm, while the graphite chamber, because of its lower sensitivity to neutrons, was placed 15 cm away from the target. The inverse square law correction between the 15 and 30 cm positions with the CH chamber was then applied to the data as well as other corrections in terms of normalization, the effect of gas flow in the graphite chamber and the wall attenuation effects. The ^{252}Cf measurements were also made similar to those for monoenergetic neutron beam from the accelerator, except that the monitoring system was not employed.

Due to recombination of positive and negative ions in the chamber cavity a lack of saturation may occur, which will affect the observed ionization charges. In order to correct this effect, gamma ray calibrations and neutron measurements were conducted with both

positive and negative polarizing voltages in specific voltage ranges. For every observation at a given voltage the mean value of the two charges collected for both polarities was taken and the saturation curve was plotted to find the true charge value at an infinite voltage. The results of the measurements were then compared to the experimental saturation curves and the standard errors were found using the least square fit method. The standard errors arose directly from the applied experimental technique and show the precision of the measurements. In addition to standard errors, systematic errors also need to be taken into account to establish the overall uncertainty of the measurements and calculations. The latter errors in this case were mainly due to the corrections (for lack of saturation, flow rate, etc.) applied to the ion chambers measured values and systematic errors in the calibration source. The other type of systematic errors was the uncertainties in the values calculated in equations, which convert the normalized charges measured by the two chambers into the neutron dose and gamma-ray dose. The source of the uncertainties in calculated quantities were mainly errors on the kerma ratios and W values used in these equations. The measurement results for the monoenergetic neutron fields with energies of 0.67, 2.1 and 5.5 MeV showed a high precision in finding the neutron component of the absorbed dose by a standard error of ±2% and systematic error of ±7%. The reason was that the neutron response of the graphite chamber at these energies was very low and it measured the gamma radiation component very accurately. However, for higher energy neutrons of 15.5 MeV the graphite chamber showed a higher response to neutrons and therefore, the neutron dose obtained from this method was less accurate (±3% standard error and ±14% systematic error). The authors made a correction to these results by replacing the gamma measurements of the graphite

chamber with a film dosimeter values and reduce the systematic error to ±7%. However, for the ^{252}Cf radiation field with the broad neutron energy range, this technique obtained the neutron dose with a ±10% and gamma dose with ±14% systemic error. Therefore, while the twin chamber method can be employed for mixed-radiation fields with lower energy neutrons, it did not show high accuracy in higher energy neutron dosimetry. Moreover, this method only measures the average dose deposited by charged particles and does not provide any information about the pattern of interactions that occur inside the chamber's cavity. By contrast, proportional counters have the ability to collect the signals due to the energy deposited inside their cavity by every individual interaction of charged particles, sort them according to their size and provide an event-size spectrum as the output. These devices, especially tissue equivalent proportional counters (TEPCs), became very popular in microdoimetry and made significant improvements in understanding the manner of radiation interaction with tissue. The idea of using a TEPC together with another proportional counter, which is not sensitive to neutrons, was proposed years ago. However, this idea has not been supported by sufficient experimental data. One of a few studies, which has been conducted measurements based on this idea, is summarized below:

DeLuca, Schell, Pearson, and Attix employed a pair of miniature proportional counters to measure neutron and gamma doses separately in a mixed radiation field. Both of the counters had a 1.27 cm spherical cavity (DeLuca Jr et al., 1981). However, one of them was enclosed by a spherical shell made of A-150 tissue equivalent plastic and was filled with propane-based tissue equivalent gas (at a pressure of 30 torr), while the other one had a graphite wall and was filled with Ar-CO_2 gas (55 torr). The radiation field was a mixture of ^{60}Co gamma

rays and 14.8 MeV neutrons. The counters were placed at a distance of 10 cm from the neutron source and 193 cm from the gamma source in the opposite direction. An A-150 walled ionization chamber (air-filled) and a miniature Geiger-Muller counter, which was insensitive to neutrons, were also used to examine the performance of the two counters by comparing the measured doses together. The CPC (Carbon proportional counter) was used to determine the photon dose component, which was obtained from a pre-calibrated ^{60}Co spectrum. This spectrum was then normalized to the mixed-field spectrum and again normalized to a photon only spectrum measured by the A-150 walled counter. The final normalized spectrum then was subtracted from the mixed-field dose spectrum measured by the tissue equivalent counter (A-150 walled counter) to find the neutron dose spectrum. These measurements were conducted in three different mixtures radiation fields; 100% neutrons, 70% neutrons + 30% photons, and 50% neutrons + 50% photons. Since the two counters could be assumed as Bragg-Gray cavities, the absorbed dose in tissue was obtained from the absorbed dose in the gas cavity using the equations based on the Bragg-Gray cavity theory. In these equations, the values of kerma in tissue and wall as well as the mass stopping powers in wall and gas were taken from previous studies. In order to find the stopping power values, the average energy of the secondary charged particles produced by photons and neutrons was estimated as follows: 300 keV for electrons produced by photons, 3 MeV for proton recoils created by neutrons and 3.7 MeV for alpha particles induced by neutrons. The results of this study showed a very good agreement in the neutron dose value obtained from the tissue equivalent counter and the A-150 ionization chamber for the pure (100%) neutron radiation field. However, for the mixed-fields of neutron and gamma radiation, despite being

in good compliance, there was a bigger difference between the neutron dose deduced from the TEPC and the one acquired from the ionization chamber. This difference shows that the determined gamma dose in this research was not very accurate. Albeit this report only compared the absorbed dose values and did not provide the actual dose spectrum measured by the TEPC and the CPC. Therefore, it is difficult to evaluate the details of its approach in gamma dose calculation, especially in the overlap area between the electron events and the fast recoil protons.

3.2 Survey of computational methods used to simulate Tissue Equivalent Proportional Counter response

In addition to experimental measurements, which are required to study the response of the twin-counter system proposed in this research, computational simulations are also beneficial to compare with experiments to provide further insight into the counter responses and establish confidence that simulations alone can be used to predict counter performance in mixed radiation fields, where the experimental measurements are difficult to make such as low orbit or space environments.

Simulation toolkits such as MCNP (different versions), FLUKA, GEANT and PHITS are the most well-known options that can be used for this purpose.They all work based on Monte Carlo techniques for simulating the transport of neutrons and charged particles through materials. These simulations are important for understanding the behavior of radiation in different environments and can help predict the response of radiation detectors. The detailed description of the Monte Carlo models for neutrons and charged particles transport can be found in (Berger, 1963) and (Bielajew, 2001) and a summary of these models is provided below.

When simulating the transport of neutrons, Monte Carlo methods are used to model the four main steps involved in the process. These steps include calculating the distance to the next collision, selecting the collision nucleus based on the total macroscopic cross section, identifying the type of interaction that the neutron will undergo with the nucleus based on the microscopic cross section, and calculating the kinetic energy lost by the neutron after the interaction and modelling the creation of secondary charged particles.

To model the transport of charged particles, Monte Carlo simulations involve modeling the trajectory of a particle by dividing it into small steps and using the condensed history technique to calculate the kinetic energy lost and the resultant angular deflection for each step. Two types of collisions, continuous and catastrophic, can be modeled. Continuous collisions involve the gradual loss of kinetic energy, while catastrophic collisions result in a significant loss of energy and secondary particle production.

There are different models used to describe charged particle transport using Monte Carlo techniques: Class I models involve determining the displacement length of a step, including finding the kinetic energy lost by the particle after step traversal and splitting the specific step into smaller sub-steps. Class I' models allow for the preselection of the kinetic energy at the end of all steps and Class II models describe continuous and catastrophic collisions and quantifies the angular deflection undergone by a charged particle after traversing a step. Different software packages use different transport models for simulating charged particle and neutron transport. The specific model used depends on the simulation requirements and the type of material being simulated.

The following methodology is used by MCNPX to transport electrons, positrons, and heavy charged particles. The Class I model is applied for electrons and positrons, while the Class I' model is used for heavy charged particles. The transport methodology used for electrons and positrons may not be suitable for charged particle transport across an interface that separates two material zones, as it can affect the calculation of the kinetic energy deposited by the particle in the newly traversed material. In contrast, the kinetic energy of heavy charged particles at a boundary is more realistic, as the kinetic energy lost by a heavy charged particle is based on the displacement lengths of the sub-steps it traverses, including the truncated sub-step that takes it directly to the boundary interface.

MCNPX is a widely used general-purpose Monte Carlo code for simulating particle transport in complex geometries. It has a comprehensive set of nuclear data and allows users to simulate a wide range of particle types and energies. It is often used in nuclear physics, radiation protection, and medical physics applications. Its ability to simulate complex geometries and the large variety of particles and energies through accurate tallies are considerable advantages. However, MCNPX can be time-consuming to run and requires a significant amount of expertise to use.

FLUKA uses the Class II model to transport charged particles. It applies path length correction and employs the Molière theory to calculate angular deflection. The drift technique is used to transport charged particles across boundaries. This information is based on studies by (Ferrari, Sala, Guaraldi, & Padoani, 1992) and (Fasso, Ferrari, Ranft, & Sala, 1995). FLUKA has a comprehensive set of nuclear data and includes a wide range of physical processes, such as electromagnetic and hadronic interactions. It is often used in

high-energy physics, radiation protection, and medical physics applications. Its advantages include the ability to simulate complex geometries and physical processes and high accuracy. However, like MCNPX, FLUKA can be time-consuming to run and requires a significant amount of expertise to use.

The Class II model is used to transport charged particles in GEANT4 and displacement length is calculated based on the particle's range and kinetic energy. Path length correction is used to modify the displacement length of the step. Continuous collisional and discrete losses are modeled, and the total kinetic energy lost by the particle after completing the step is calculated. For describing the energy loss and scattering of charged particles as they traverse through matter, the straggling model is used by GEANT4. This physical model is used to simulate the interactions of particles with matter in various applications, such as in high-energy physics experiments and medical physics. While GEANT has a user-friendly interface and can simulate complex geometries and physical processes, it may not be as accurate as other codes for certain applications (Faddegon et al., 2009) and can be computationally demanding.

PHITS utilizes the Monte Carlo method in event generator mode to trace the trajectory and interactions of every source particle, including the production of secondary particles that arise during their interactions. The Monte Carlo method involves randomly sampling from probability distributions to determine the outcomes of particle interactions, allowing for a statistically accurate simulation of particle transport.

PHITS also includes a number of advanced features in its event generator mode, such as the ability to model complex geometries and the ability to handle multiple sources of particles. In

addition, PHITS can simulate a wide range of particles, including neutrons, protons, heavy ions, electrons, and photons. It is often used in medical physics, radiation protection, and space radiation applications. Its advantages include the ability to simulate a wide range of particles and energies and efficient simulation of large-scale geometries. However, PHITS can be computationally demanding and requires a significant amount of expertise to use.

In order to choose an appropriate software to assess the TEPC response in neutron-gamma mixed field dosimetry, the study by Ali et al. (Ali, Waker, & Waller, 2013) has been used as the main reference. This study provided an inter-comparison between MCNPX v2.7.E, FLUKA v2011.2 and PHITS v2.24 to find the best candidate code for compact TEPC designs for operation in low energy neutron and gamma radiation fields. The three codes were used to simulate a 2μm site size for three different neutron irradiations and several site sizes for gamma rays of different energies. These simulations were then benchmarked against the experimental values in the same radiation fields. According to this assessment, the frequency and dose mean lineal energies calculated by FLUKA version 2011.2 for simulating different site diameters were in close agreement to the corresponding experimental values for the three incident gamma energies (323 keV, ^{137}Cs and ^{60}Co). However, in terms of neutron dosimetry, MCNPX and FLUKA were not capable of modeling the production and transport of secondary alpha particles created in the TEPC as a result of neutron capture reactions. PHITS on the other hand was able to simulate the transport of all secondary charged particles created by neutrons of different energies (144 keV, 570 keV and 14.8 MeV) thanks to its event generator feature. Therefore, based on the benchmarking work of Ali et al, despite the overestimation observed in 14.8 MeV neutrons event-size spectrum produced by PHITS in

the events region of 500 to 1000 keV/μm, the PHITS code was chosen for simulation to provide insight into the GPC and TEPC responses and assist in the measurement-data analysis. As demonstrated in chapters 5 to 9 of this thesis, good agreement found between the simulations and measurements would also give some confidence in using simulations to obtain instrument responses in radiation fields that would not be possible to obtain by experiment alone.

Although PHITS indicated acceptable TEPC simulation results for neutron dosimetry, code development is taking place continuously and open source codes with large user communities such as GEANT should be kept in mind for future studies.

Ménard, Cutarella, Lahaye, and Bolognese-Milsztajn provided a description of a small TEPC with multi element geometry (CIME) developed by the Institute for Protection and Nuclear Safety (IPSN) for personal radiation protection monitoring (Ménard, Cutarella, Lahaye, & Bolognese-Milsztajn, 2001). In this dosimeter a lattice of cylindrical elements is devised in a panel of resistive tissue equivalent plastic, which is enclosed between two plates of conductive tissue equivalent plastic. Each cylindrical element is filled with Ar-CO_2 gas with a low pressure of 200 torr. The counter was modeled in GEANT 4 and the 565 keV neutron interactions with the filled gas were simulated to investigate the charged particles chord length distribution in the counter. Due to the complexity of the counters convertor geometry, the chord length distribution of the charged particles is broad and complex. Therefore, when the dose distribution of the 565 keV neutrons inside the counter is obtained, the proton peak is also broad and has no obvious proton edge, which makes it impossible to perform lineal energy calibration for the counter.

Hanu, Byun, and Prestwich simulated the microdosimetric responses of a prototype thick gas electron multiplier (THGEM) to neutrons of different energies using GEANT4 v.9 (Hanu, Byun, & Prestwich, 2010). They calculated the deposited energy in the sensitive volume of the detector, which is a cylindrical gas cavity with the height and diameter of 5 mm. The counter was filled with propane-based tissue equivalent gas and the gas pressure was adjusted so that the gas cavity simulated a 2 μm tissue cell. The cylinder was vertically surrounded by an insulator, made of Rexolite and the whole area was enclosed by two horizontal layers of A-150 tissue equivalent plastic, which was performed as the cathode of the counter. The THGEM consisted of a series of holes, which were fabricated in a copper coated G10/FR4 fiberglass epoxy insulator. The electrons produced in the gas cavity were then multiplied and collected by the anode made of copper. When a voltage of 709 V was applied to the prototype THGEM, the created pulse was similar to the standard TEPC response. In order to investigate the response of this detector to neutrons, it was modeled in GEANT 4 and its irradiation by neutrons of different energies was simulated. Simulation results were then compared to the experimental data measured by a standard TEPC and reported elsewhere (Byun, Spirou, Hanu, Prestwich, & Waker, 2009). A detailed and useful description of the GEANT neutron-data libraries and the neutron and charged particles transport techniques applied in the simulations was provided in the publication. The THGEM detector measured the energy deposited in its sensitive volume. Therefore, the quantity, which was required to be obtained from the conducted simulations, was the deposited energy in the sensitive volume per incident neutron. This quantity was created in the output of a coded tally and the results were converted into a lineal energy distribution using a data

analysis code to provide a better demonstration of the microdosimetric quantities. The spectrum then redistributed into equal logarithmic bins (each decade into 60 bins), thus resulting in a smoother progression of the curve. Each data point was also multiplied by the corresponding lineal energy value (y) and the spectrum was plotted in a semi-log graph such that each area under the curve between two values of y was proportional to the fraction of dose in that region. Both the energy response and the angular response of the THGEM detector were investigated in this research. For the energy response, neutrons with different energies were simulated in GEANT4 to be irradiated to the detector at 0˚. The results showed distinct proton peaks in the dose distribution spectra, which indicated that the predominant interaction inside the gas cavity was elastic scattering from Hydrogen nuclei. The proton edges of the spectra for different neutron energies were at the same place and agreed to both the theoretical expectations and the experimental results from another study (A. Waker, 1995). The alpha particles and other heavy ions peak positions were also consistent with both the theoretical and experimental values. The edges of these peaks were distinctively visible in the spectra and revealed useful information about the neutron interactions with the gas molecules, which result in producing heavy ions.

The angular response of the THGEM detector was also studied by changing the incident neutron beam angle from 0˚ to 180˚ in the simulations. 100 keV and 1 MeV neutrons were included in this investigation and it was found that for 100 keV neutrons the neutron dose was almost independent of the beam angle. However for 1MeV neutrons the THGEM response was decreasing as the incident beam angle was increased from 90˚ to 180˚. After conducting more simulations of the detector with and without the wall material, the reason of

the angular dependence was found to be different contributions of the wall interactions to the dose deposited in the sensitive volume. Therefore, the design of the detector was modified by adding a layer of A-150 plastic over the THGEM resulting in improvement of the angular response.

Taylor, Hawkesa and Shippen developed a model of a Far West Technology LET-SW5 TEPC, using a standard release of GEANT4 9.6 p2 code (Taylor, Hawkes, & Shippen, 2015). However, the authors applied nonstandard neutron cross section files and environmental variable options provided by other experts to overcome the shortcomings of GEANT4 default libraries. They specifically selected the physics list QGSP_BERT_HP, in order to use the High Precision (HP) neutron cross section files, which are experimentally-based rather than model-based. This step was not enough to resolve the discrepancies between the simulations and measured data, especially in the alpha dominated part of the spectra. Therefore, in the next step, the G4NDL4.2 neutron data library of the code was substituted with CENDL3-1 [provided by (Mendoza, Cano-Ott, Guerrero, & Capote, 2012)], which included the $^{12}C(n, n' 3\alpha)$ reaction and provided better agreement to the experimental spectrum. A final modification was also applied to the code in order to calculate the number of ion pairs rather than the deposited energy in the gas cavity, similar to the quantity that is measured with the TEPC. To perform this transformation, the code was modified so that it provided information about the type of the particles, which deposit energy in the counter's sensitive volume and their energy when entering and exiting the cavity. Some algorithms from other studies ((Siebert, Grindborg, Grosswendt, & Schuhmacher, 1994) and (Taylor, Jansen, Zoetelief, & Schuhmacher, 1995)) were then applied to derive the appropriate w-values and calculate the

total number of ion pairs created by each source neutron. The final step was to find the dose distribution and compare it to the measured spectrum. In order to find the dose distribution such that its proton edge is aligned to that of the measured spectrum, the number of ion pairs was again converted to lineal energy using a fixed w-value of 33 eV/ion pair. Due to applying these modifications, the dose spectrum was significantly improved compared to the previous studies including the three simulation codes assessed by Ali et.al (Ali et al., 2013). A very good agreement was observed between the output spectrum and the experimental results, especially in terms of the proton peak, and the proton, alpha and carbon recoils edges. These improvements observed in both the cases of a 14.8 MeV monoenergetic neutron source and a 252Cf spontaneous fission neutron source, which has a broad energy spectrum from 4_x10-7 MeV to 15 MeV, with a mean energy of 2.1 MeV.

Min, Shuhu, Cong and Xu also used GEANT4 to simulate a spherical TEPC in three monoenergetic neutron radiation fields with energies of 2 MeV, 6 MeV and 10 MeV (Min, Shuhu, Cong, & Xu, 2017). They calculated the dose averaged-lineal energy from the simulation data and compared them to the experimental results reported in another study (Zhao, 2010). The agreement between the two sets was very good, with a deviation less than 2%.

Malimban, Nam, Pyo, Youn and Ye studied the response of a new spherical TEPC invented by the Korea Astronomy and Space Science Institute (KASI) to neutrons and photons through ground-based measurements and Monte Carlo simulations (Malimban, Nam, Pyo, Youn, & Ye, 2019). This detector was designed to monitor the space radiation environment in the low earth orbit and has been scheduled to be on board the Korea

NEXTSat2 satellite planned to be launched in 2021. It was a Benjamin-type TEPC (Benjamin, Kemshall, & Redfearn, 1968) with a spherical sensitive volume of 60 mm in diameter, filled with pure propane gas and surrounded by a 3 mm thick A-150 tissue equivalent plastic wall. The whole detector was enclosed in an aluminum case with a thickness of 1.5 mm to provide an air tight seal and protect the TEPC from electromagnetic interference. The pressure and density of the gas were set such that gas cavity simulated a 2μm tissue cell. The counter were irradiated once by 662 KeV gamma rays coming from a ^{137}Cs source and then exposed by mixed neutron and photon field of ^{252}Cf, both at a distance of 10 cm from the TEPC. The counter was then modeled in GEANT4 v 10.03.p01 and the experimental set-up and measurements were simulated using this Monte Carlo code. A primitive scorer of the code (G4PSEnergyDeposit) was used to calculate the deposited energy by all particles in every event created in the gas cavity. The deposited energy per event then converted into lineal energy to obtain the microdosimetric spectra. In the simulation of gamma field, the default electromagnetic physics constructor (G4EmStandardPhysics) was replaced with one of the low energy electromagnetic physics packages offered in Geant4 (G4EmLivermorePhysics) to lower the threshold of secondary electrons generation and provide better electron transport (Cirrone et al., 2010). The results of this simulation were then compared to the measured (and extrapolated) data and also to the data reported in another study (Moro & Chiriotti, 2015). The results showed a good agreement between the three sets of data, especially for the electron edge position. However, the simulation spectrum showed lower values in the lineal energy region of 0.4 keV/μm and

2 keV/μm. This was assumed to be due to shortcomings of the chosen electromagnetic physics model.

Neutron field simulation was conducted in two phases to reduce the simulation run-time. In the first part the ^{252}Cf source was modeled and in second part the TEPC response in this radiation field was simulated. In the latter part, the authors applied extra scoring filters, which included the G4UserTrackingAction class and stored the track histories of the generated particles. This way they were able to backtrack every particle that deposited its energy in the sensitive volume and score the energy deposited by photon and neutron events separately. An inter-comparison was made between the experimental and simulation results of this radiation field and two other studies published data ((Nam et al., 2015) and (Farah et al., 2017)). The agreement between these spectra was satisfactory, except for the gamma region ($y<10$ keV/μm), for which some deviations were observed between the four spectra. The experimental data were insufficient for the events below 1 keV/μm and unavailable for events higher than 450 keV/μm. This problem was addressed to be resolved by employing two gas gains (low and high) to the TEPC, to extend the lineal energy coverage. The anomalies in the GEANT4 simulation results for low lineal energy events were also addressed to the physics model implemented in the code. However, the proton peak and edge and the heavier ions edge of the measured and simulated spectra was in fairly good agreement with the results presented in the two reference studies.

Chapter 4

Experimental and Simulation Set-up Description for Neutron-Gamma Dosimetry with Twin Proportional Counters

In order to use a TEPC and a heterogeneous proportional counter for neutron-gamma mixed field dosimetry, the two aforementioned counters must be able to measure gamma dose accurately, and have very similar responses to gamma radiation. Another requirement for this method to work is that the heterogeneous counter, which is the Cy-GPC, should be insensitive to neutrons. On the other hand, the TEPC must be sensitive to neutron radiation to the same degree as human tissue. Thus, neutron and photon measurements were carried out with both the counters to verify these two requirements. When the intended neutron and gamma response of the two counters was confirmed, mixed-field measurements were taken with the counters. In order to find the pure neutrons dose rate spectrum in a mixed-radiation field, the dose rate spectrum measured with the Cy-GPC must be subtracted from the spectrum measured with the Cy-TEPC. Following the methodology described above, experimental measurements are presented and analyzed in the following chapters. This methodology was also further investigated through Monte Carlo simulations using the PHITS code and the results and comparison to the measured data are discussed at the end of each chapter. However, the general description and the details of the experimental and computational set-ups used in the conducted measurements and simulations of this study are presented in this chapter.

4.1 The twin proportional counters designed for neutron-gamma dosimetry used in the course of the current study

The heterogeneous counter used in this study is a Cylindrical Graphite Proportional Counter (Cy-GPC). Both the Cy-TEPC and the Cy-GPC counters used in this study were designed and custom-made by Dr. Waker (A. Waker, 2010) and both counters were disassembled and rebuilt for this study. The sensitive volume of these counters is a right cylinder, whose diameter and height are 1.5 cm. This volume is bounded by field tubes as well as the wall of the counter. The anode of the counter is a 50 μm diameter gold plated tungsten wire which is coaxial to the cylinder, and the wall of the counter acts as the cathode in these counters. The counters are contained in a gas-tight container made of aluminum.

All the geometrical characteristics of the two cylindrical counters are the same. Figure 4-1 shows a cross sectional view of these counters modeled in an interactive modeler called SimpleGeo.

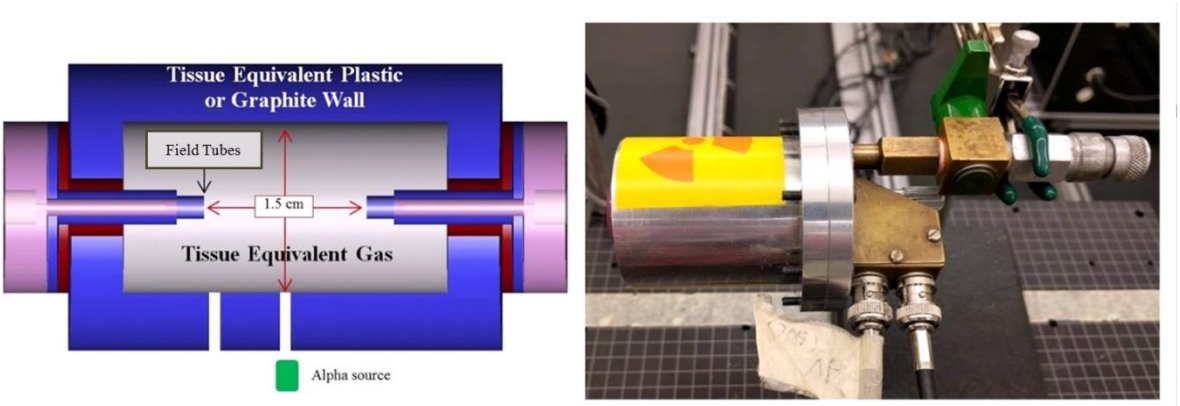

Figure 4-1 Actual and cross sectional views of Cy-TEPC and Cy-GPC

Both counters have a finely collimated internal alpha source, which emits quasi monoenergetic alpha particles inside the sensitive volume of the counter. The alpha source is used for calibrating the counter in terms of lineal energy, based on the process explained in section 2.2.1. There are two holes machined in the wall of the counter: one aligned to the middle of the sensitive volume, and the other aligned to the end of one of the field tubes (Figure 4-1). The location of the alpha source can be adjusted between these two holes. When the alpha source is positioned in front of a hole, a beam of alpha particles can pass through the counter, and deposit its energy in the sensitive volume. This is called the on-position of the counter relative to the alpha source. When the alpha source is positioned somewhere between the two holes, the alpha particles are blocked by the wall. The middle position of the two holes is called the off-position of the alpha source. Both of the counters are filled with propane based tissue equivalent gas. The pressure of the gas is adjusted in such a way that it simulates a particular microscopic site in tissue. The pressure of the propane-based tissue equivalent gas, which is used to fill the custom-made Cy-TEPC and the Cy-GPC in this study, was 55.6 Torr (~7413 Pa) to simulate a 2 μm tissue site size, which was the optimum choice for these measurements. Microdosimetric measurements commonly use simulated site diameters ranging from 0.5 to 2 μm, as larger sizes do not effectively capture the sub-cellular biophysical mechanisms of radiation action. The lower limit of simulated site diameters is constrained by the ability of the counter to produce gas gain at low pressures. ICRU Report 36 recommends not measuring below 0.3 μm. This limit depends on the counter's physical and electric field characteristics (Burmeister et al., 2001).

The A-150 plastic wall of the Cylindrical Tissue Equivalent Proportional Counter (Cy-TEPC), designed to simulate human tissue, was manufactured with a thickness of 5mm. This particular thickness was selected to approximate the range of protons generated within the TEPC wall when 65 MeV neutrons interact with it in a radiotherapy environment (Svensson & Landberg, 1994). The wall of the Cylindrical Graphite Proportional Counter (Cy-GPC) was made out of graphite which is very insensitive to neutrons compared to A-150. The cross-sectional data for neutron interactions with hydrogen, carbon, oxygen, and nitrogen, presented in Appendix A, shows that at lower neutron energies, the cross-sectional probability of elastic scattering with carbon is significantly lower than that with hydrogen (about eight times lower).

In addition to these two cylindrical counters, two other counters were used as third party benchmarks to examine the Cy-TEPC and the Cy-GPC responses to photons and neutrons.

In order to verify that the Cy-TEPC and the Cy-GPC are reliable for photon dosimetry, their measurements of photon dose rate were converted to the air-kerma rate, and compared with the photon air-kerma rate measured by an A4- Standard Imaging spherical ion chamber. The A4-ion chamber is filled with dry- air, and the wall material is also air equivalent (Figure 4-2). This counter was calibrated for the Cs-137 gamma radiation.

Figure 4-2 Standard Imaging A4-ionization chamber, collecting volume: 30cc

The neutron response of the Cy-TEPC was considered by comparing it with a commercial 5" tissue equivalent spherical counter from Farwest technology. The sensitive volume of this chamber is surrounded by a Shonka A-150 plastic wall of a specific thickness sufficient to make the proton equilibrium available (Figure 4-3) (Al-Bayati, 2012). The whole counter is placed in a tight aluminum container to provide the electrostatic shielding and maintain the low tissue equivalent gas pressure required for the counter operation.

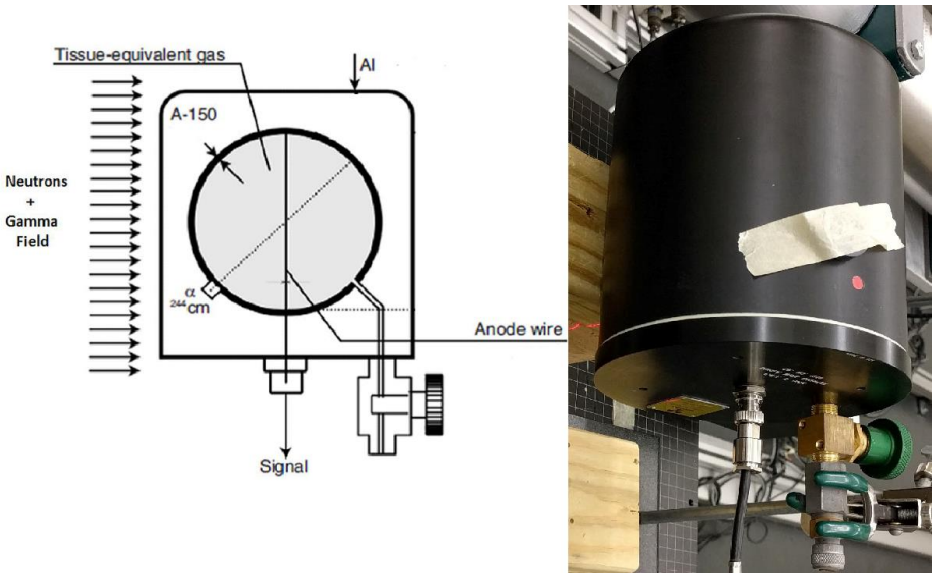

Figure 4-3 LET-SW5, 5" SINGLE WIRE COUNTER from Farwest Thechnology Inc. and its cross sectional view from (Al-Bayati, 2012)

The dimensions of the counters and composition of the gas and wall material are summarized in Table **4-1**.

Table 4-1 Detectors' specifications

Detector	**Geometry of Sensitive Volume**	**Dimensions (cm)**	**Wall Material**	**Gas Pressure (torr)**	**Mass of Gas (mg)**
Cy-TEPC	Cylinder	Diameter: 1.5 Height: 1.5	Shonka A-150 Plastic	55.6	0.35
Cy-GPC	Cylinder	Diameter: 1.5 Height: 1.5	Graphite	55.6	0.35
5" TEPC	Sphere	Diameter: 12.55	Shonka A-150 Plastic	6.5	16

4.2 Preparing the Experimental set-up and Data Presentation

Before taking the measurements, the counters are evacuated and then filled with the tissue equivalent gas. For the experiments in this work, the pressure of the gas is adjusted so that the counters simulate a 2μ diameter tissue cell. Figure 4-4 shows a typical vacuum and gas filling system used in these measurements.

Regardless of the type of the counter which is used in radiation dosimetry, the most important problem in validating the measurements is to make sure that the counter is calibrated correctly. The fundamentals of calibration of the TEPCs are reviewed in the next section.

Figure 4-4 Vacuum and gas filling system

4.2.1 Calibration of the proportional counters

Proportional counters generate pulse rate and pulse heights which are correlated to the interactions between the charged particles and associated secondary particles crossing the gas cavity. Therefore, in order to reliably use counter outputs in calculation the imparted energy in the cavity, the counter needs to be calibrated in terms of the event size or the lineal energy. In each of the Cy-TEPC, Cy-GPC and the 5" ion chamber a built-in monoenergetic alpha source with a known energy is used for this purpose. The calibration factor in this case is going to be the ratio of the desired quantity (i.e. the lineal energy) over the measured quantity (i.e. the pulse height).

In order to find the lineal energy of a particle with energy E, the mean energy deposited in the simulated cell volume, ΔE, needs to be calculated and divided by the mean chord length of the volume. ΔE can be found using the relationship between the energy and range of the particles. This information is accessible through the databases used in the Monte Carlo code SRIM (Stopping and Range of Ions in Matter) (James F Ziegler, Ziegler, & Biersack, 2010). A typical energy-range relationship for a particle in a specified medium is shown in Figure **4-5**.

The energy of the alpha particles when entering the counter is known (E_1), the corresponded range (R_1) can be easily read from the energy-range diagram. The change in energy of the particle when it passes through the counter correlates to the difference in the particle's range.

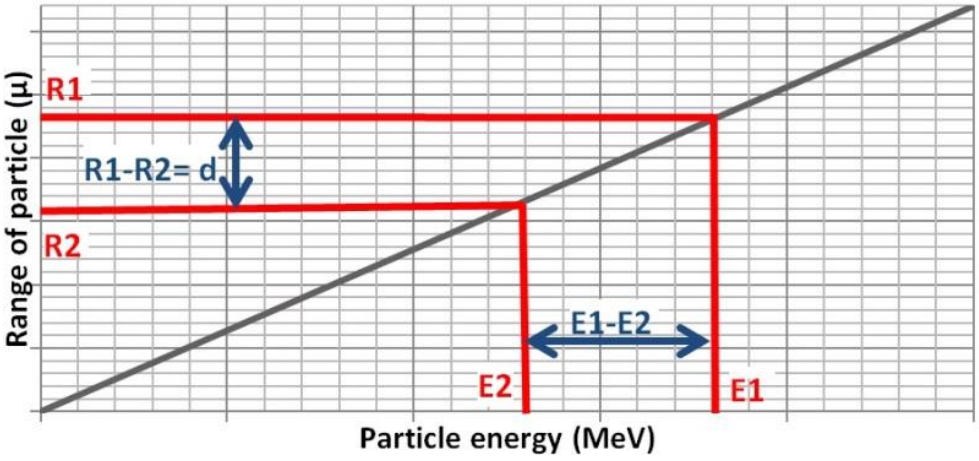

Figure 4-5 Typical range versus energy relationship

Since the counter is designed to simulate a tissue site, the range of the particle when exiting the counter (R_2) is obtained by subtracting the simulated site diameter (d) from the range of the particle when entering the counter (R_1):

$$R_2 = R_1 - d \quad (4.1)$$

The energy of the particle when leaving the counter (E_2) can then be obtained from the range-energy diagram. The difference in energy (ΔE) which is equal to E_1-E_2, should be divided by the mean chord length of the simulated volume ($\bar{l}$) to obtain the mean lineal energy of the particle. The mean lineal energy of the 5" Chamber, the Cy-TEPC and the Cy-GPC for a 2 μm simulated diameter are listed in Table 4-2.

Table 4-2 Mean lineal energy deposited in each counter by the alpha particles of the calibration source

Counter	Mean Energy of alpha source (MeV)	Mean lineal energy (keV/μm)
5" Chamber	5.76 (Cu-244)	127.5
Cy-TEPC	4.2 (Am-241)	161.8
Cy-GPC	4.35 (Am-241)	157.7

The next step in calculating the calibration factor is to read from the Multi-Channel Analyzer (MCA) the channel number corresponds to the mean deposited energy of the alpha particles inside the gas.

The alpha particles enter the sensitive volume of the counter through a small aperture in the wall. These particles ionize the gas inside the counter producing a voltage pulse as described in section 2.2.1. Although, the alpha particles emitted by the calibration source are quasi monoenergetic, they may have various paths within the gas or experience different interaction histories (straggling). Therefore, they can deposit different energies in the gas cavity. Consequently, the stored pulses in the pulse height analyzer follow a quasi-Gaussian distribution. The peak of this distribution corresponds to the most probable amount of lineal energy deposited inside the gas by individual alpha particles. Therefore, the position of this alpha peak needs to be read for calibrating the counter. The calibration factor is the quotient of the mean lineal energy of the alpha particles (in keV/μm) divided by the alpha peak position channel number. Thus, the unit of the calibration factor is keV/μm/channel.

The next step to prepare the equipment for doing a measurement is to find the appropriate high voltage and gain, which is applied to the amplifiers. These factors can be determined by estimating the range of lineal energy that the secondary charged particles deposit in the counter. Then, according to the lineal energy range of interest and the calibration factor of the counter, the gain of the amplifier(s) is calculated.

4.2.2 Combining data of two amplifiers

Sometimes, more than one amplifier is needed to cover the whole range of lineal energy. For example, in the photon and mixed-field experiments two amplifiers were used to cover a lineal energy range of 0.1 to 10 keV/μm (Figure 4-6).

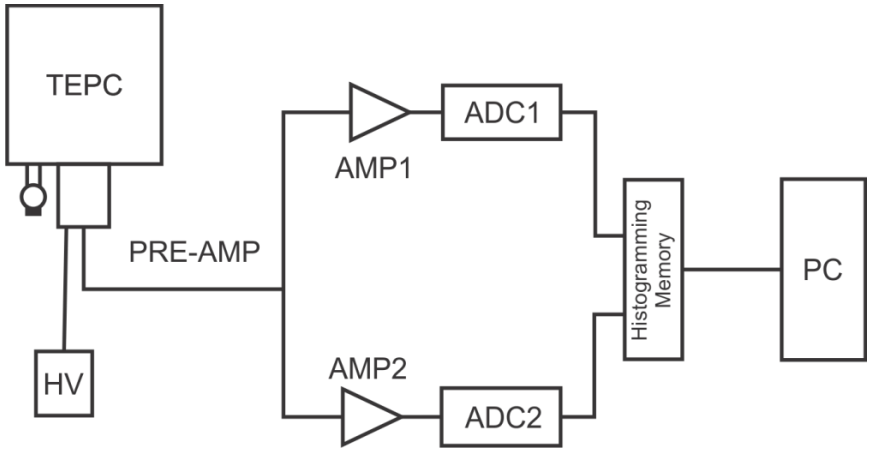

Figure 4-6 Schematic presentation of the gamma measurement set up (Al-Bayati, 2012)

The gain of the two amplifiers was set so that they have a relatively wide enough overlapping area (~a few hundreds of eV/μm) on the lineal energy spectrum. The lineal energy spectrum is finally plotted so that the left side of the spectrum up to the mid-point of the overlapping area is generated from the higher gain amplifier data and the right side of it is plotted based on the measurements of the lower gain amplifier (Figure 4-7).

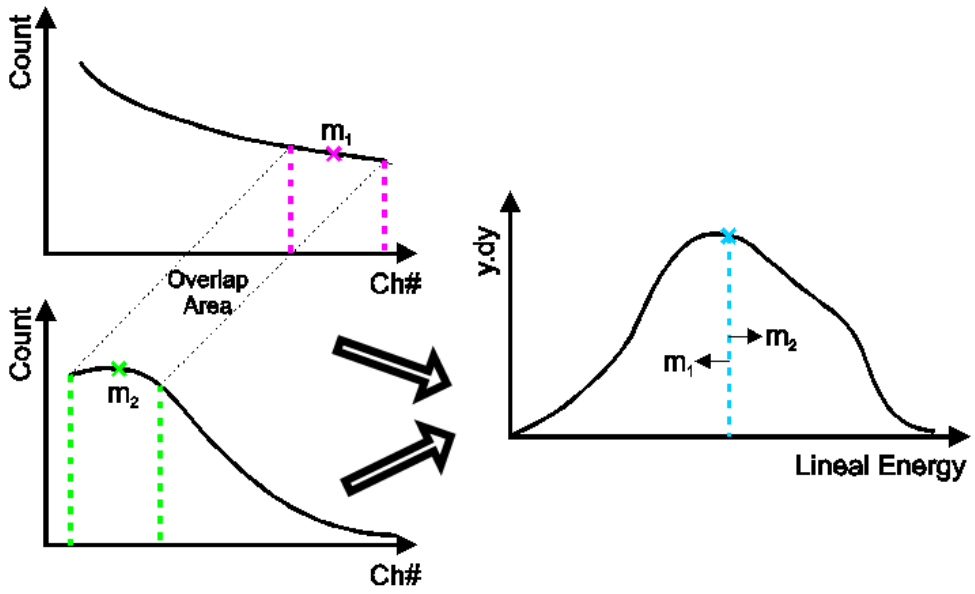

Figure 4-7 Combining the data of two amplifiers

After taking the measurements and collecting the data in the MCA, the deposited energy distribution inside the counter needed to be represented in an appropriate way for analysis. This process is explained in the following section.

4.2.3 Data representation and redistribution

The raw measurement data is represented linearly on the PCMCA screen (part (a) of) which shows the frequency of the pulses created by the individual energy deposition events in the counter. In order to create a better way of presenting data an equal logarithmic bin scale was used. This method of data representation makes the post-analysis of data more convenient. To implement this method, every linear decade on the horizontal axis (lineal energy) was represented in 50 equal logarithmic bins, so that the relationship between the logarithmic bins (x) and the lineal energy (y) was as follows:

$$x = 50 \log y + b_0 \quad (4.2)$$

Above, b_0 is the x-intercept and has to be set such that the bin numbers (x) start from zero. Since, the lineal energy of the events created by the photons in this research was typically more than 0.01 keV/µm, b_0 was set to 100 in order to make the logarithmic bins start from x_0=0. When transferring the linear lineal energy data to the logarithmic bins, the upper bound of each logarithmic bin (x_N) was placed at the nearest value of lineal energy for which the x in equation (2.2) became an integer number N. All the lineal energies up to that value were transferred into that bin. For example, substituting $y= 0.01$ keV/m in equation (4.2) resulted in $x=0$ which was the minimum value for logarithmic bins. The upper bound for lineal energies that were represented by the first bin was obtained by solving equation (4.2) for y when $x=1$. All the lineal energy values, for which the left hand side of equation (4.4) was between 0 and 1, were represented in the first logarithmic bin. Similarly, the lineal energies whose corresponding x values were between 1 and 2 were represented in the second bin and so on. The frequency of all the lineal energies transferred to each logarithmic bin were added up together to define the height of that bin (Al-Bayati, 2012). The Matlab script for data conversion into bin format can be found in the data representation section of the Matlab codes presented in Appendix C.

By converting data representation format from linear to equal logarithmic bins, the fluctuations of the frequencies for lower lineal energies were demonstrated more clearly (part (b) of). On the other hand, one might notice that in this method event sizes were simply counted and they all carry the same weight irrespective of how much energy was released in them. However, in reality, the events correspond to the higher lineal energies contribute more

to energy deposition inside the counter. For example, an event corresponding to 10 keV/μm contributes 1000 times more than the 0.01 keV/μm events which may appear more involved in energy deposition in the frequency distribution. Therefore, a better interpretation of the spectrum can be achieved if the emphasis is put on the fraction of the whole amount of deposited energy which is released by the events of a given size into the gas. In order to make this happen, the lineal energy deposited by each event (y_i) was multiplied by the frequency of that event $f(y_i)$. Then, for each logarithmic bin the $y_i.f(y_i)$ terms for all the lineal energies inside that bin were summed up. The deposited dose(μGy) distribution in the counter, in terms of lineal energy was obtained through dividing the $y_i.f(y_i)$ terms (keV/μm) by the mass of the gas (kg) inside the counter. The total deposited dose in the counter was also equal to the sum of all $y_i.f(y_i)$ terms divided by the mass of the gas in the counter. It should be noted that each measurement time was different from the others depending on the radiation type and the counter specifications. Therefore, to take into account the response of different counters in different radiation fields, the dose-rate spectra of a radiation field measured by the counters were compared together. In order to do this, all data from each counter measurement were divided by the live time of that measurement. Part (c) in the shows a typical dose rate spectrum of the neutron source.

The dose distribution was then normalized by dividing each $y_i.f(y_i)$ term by the product of the total dose and Δlny, which is the interval between the geometrical centers of two consecutive increment (yi - 1/2 and yi + 1/2) (part (d) in) (Al-Bayati, 2012).

a)

b)

c)

d)

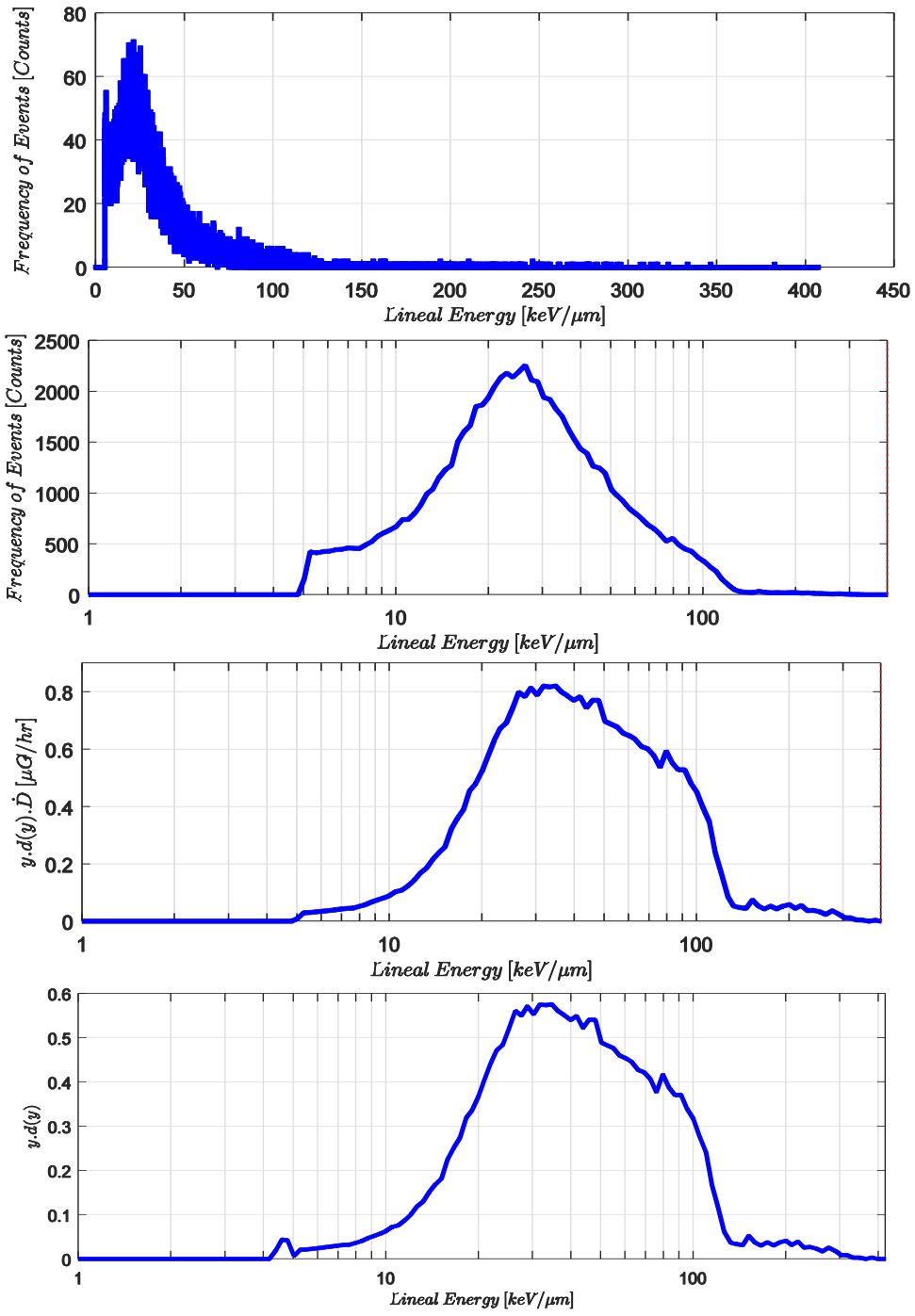

Figure 4-8 Redistributing the result spectrum. a) Linear frequency distribution of events. b) Redistribution into equal logarithmic bins. c) Dose rate distribution in equal logarithmic bins. d) Normalized dose distribution.

4.2.4 Uncertainties calculation

Statistical uncertainties of $\bar{y}_F$, $\bar{y}_D$ and the dose rate of each photon measurement have been calculated using the error propagation formula. The derivation process of the relative uncertainties of these quantities is presented in Appendix B and the obtained equations are as follows:

$$\frac{\sigma_{\bar{y}_F}}{\bar{y}_F} = \sqrt{\frac{\sum {y_i}^2 f(y_i)}{(\sum y_i f(y_i))^2} + \frac{1}{\sum f(y_i)}} \tag{4.3}$$

$$\frac{\sigma_{\bar{y}_D}}{\bar{y}_D} = \sqrt{\frac{\sum {y_i}^4 f(y_i)}{(\sum {y_i}^2 f(y_i))^2} + \frac{\sum {y_i}^2 f(y_i)}{(\sum y_i f(y_i))^2}} \tag{4.4}$$

$$\frac{\sigma_{\dot{D}}}{\dot{D}} = \frac{\sqrt{\sum {y_i}^2 f(y_i)}}{\sum y_i f(y_i)} \tag{4.5}$$

In addition to the statistical uncertainties, which depend on the number of events recorded, systematic errors also need to be considered when evaluating the precision and accuracy of the results. (Lindborg & Waker, 2017).

The most significant source of systematic uncertainty is the energy calibration of the counter. One common method of calibration is using a collimated alpha source. Knowing the actual energy of these sources is associated with a degree of error, which can lead to different stopping power evaluations and derivation of the energy lost in the counter being calibrated. Menzel et al calculated an uncertainty of 2.8 to 4.6% in the amount of energy loss by alpha particles (Menzel, Bühler, & Schuhmacher, 1982), while Kliauga reported an even larger uncertainty of ~8% (Kliauga, 1990). For the measurements reported in this work the energy

of the alpha particles used was determined by alpha spectrometry prior to their installation in the counters. Other uncertainties in the alpha source method of calibration are uncertainties in the range-energy relationship used to calculate the energy lost and errors in path length determination as well as particle straggling. A conservative estimate of the total calibration uncertainty in this work would be 5%. One way of reducing this type of error, would be to use the electron edge calibration for photon microdosimetry (Crossman & Watt, 1994), (Moro & Chiriotti, 2015) and the proton edge in the case of neutron measurements (A. J. Waker, 1985).

The gas pressure at the time of filling the counters determines the mass of gas and the simulated diameter. Error in the filling gas pressure therefore propagates to an error in absorbed dose and lineal energy. However, once filled, the counters are sealed and no change in gas density takes place. The uncertainty in gas pressure at the time of counter filling in this work has been estimated through comparison of the two different pressure gauges used and was 2%. After the counters are sealed, the gas pressure inside may change due to a change in ambient temperature between the location of gas filling and that of measurement and this may affect the gas-gain of the counter. However, any change in gas gain is taken into account by the calibration procedure that takes place immediately before and at the point of measurement.

Imprecision in the physical size of the counter will lead to uncertainty in derivation of the mean chord length of the counter. The counters used in this research have been machined to a tolerance of 0.05 mm in the 15 mm diameter and height of the sensitive volume of the

counter. This is resulting in an uncertainty of 0.3% and of the same order as the ~ 1% reported by Lindborg.

Regarding uncertainties introduced by the data acquisition system the pile up effect, which arises from long-time constants in the detection and feedback system and high count-rates, has been estimated to have an uncertainty of less than 1% by Lindborg. For the integration time constant used in this work of 2μs and the low count rates generally encountered the uncertainty value of Lindborg would be very conservative.

The aforementioned errors are listed in Table 4-3 along with the total experimental uncertainty in the average microdosimetry quantities determined in this study.

Table 4-3 Estimated systematic uncertainties for measured microdosimetric quantities reported in this work

Systematic uncertainty	$\bar{y}$ (%)	$\bar{y}_D$(%)
Energy Calibration	5	5
Gas Pressure, Mass of Gas and Simulated Site Diameter	2	2
Physical Dimensions and Mean Chord Length	1	1
Overall uncertainty (combining the uncertainties in quadrature)	~5.5	~5.5

4.3 Characteristics of photon and neutron sources used

To investigate the response of the Cy-TEPC and the Cy-GPC to photons, three X-Ray measurements and one gamma measurement were carried out. The sensitivity of the counters to neutrons was also examined in neutron measurements using the Cy-TEPC, Cy-GPC and the 5" Spherical TEPC. The characteristics of the radiation sources used in these measurements are summarized in Table 4-11. The P385 - neutron generator along with the G10 gamma source, were also used to produce a mixed n-γ radiation field. These radiation sources are shown in Figure 4-9, Figure 4-10 and Figure 4-11.

Table 4-4 Radiation sources used in this research

Source:	Manufacturer:	Specifications:
X80 - X-Ray Beam Irradiator	Hopewell Designs Inc.	X-ray range: 20-320 kV
G10 - Gamma Irradiator	Hopewell Designs Inc.	Cs-137 with an activity of 7.9 Ci
P385 - Neutron Generator	Thermo Fisher Scientific	Neutron yield of ~ 10^6 to 10^7 n/s Average energy of neutrons: 2.5 MeV

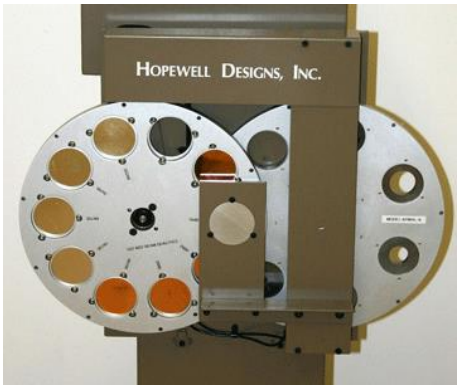

Figure 4-9 X80 - X-Ray Beam Irradiator, the filter wheels and the shutter

Figure 4-10 G10 - gamma Irradiator with a source of Cs-137

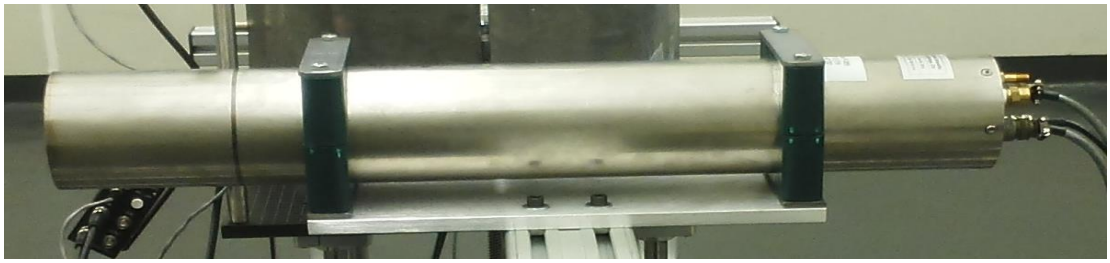

Figure 4-11 P385 - Neutron Generator (Thermo-Fisher Scientific)

4.4 Investigation of sensitivity to photon radiation for the Cy-TEPC and the Cy-GPC

The first step to investigate the functionality of the heterogeneous counter was to compare its sensitivity to photons to that of the TEPC's. The purpose of these measurements is to make sure that the two counters record the same dose and dose-rate distribution deposited by photons. Since the photons in a mixed radiation field can potentially have a wide range of energies, the response of the heterogeneous counter to different photon energies was investigated. Therefore, some X-Ray measurements were conducted to investigate the response of the Cy-GPC to lower energy photons and some gamma measurements conducted for checking its sensitivity to higher energy photons.

4.4.1 Evaluating the photon measurements

An A4-ion chamber was used as a benchmark instrument to evaluate the accuracy of the Cy-TEPC and the Cy-GPC measurements. With the Cy-GPC and the Cy-TEPC the total absorbed dose in the counter can be obtained. However, the ion chamber measures the air-kerma rate, because it is filled with dry air and is surrounded by an air-equivalent plastic wall. Therefore, the dose rate measured by the counters needs to be converted into air-kerma rate to make the comparison possible. However, this is not easily achievable, as photons emitted by interact with the wall of the GPC and the TEPC and lose some or all of their energy creating electrons. Thus, the number and energy of electrons which enter the counter cavity depend on the material of the counter wall. Whereas, in the A4-ion chamber, for which the wall and the gas are both air equivalent, the whole counter is considered as an integrated

medium with which the photons interact. Therefore, for the GPC and the TEPC, first the absorbed dose rate in the wall of the counter ($\dot{D}_{wall}$) should be found. Then, this quantity has to be converted into air kerma rate in order to make a comparison between the data of the counters with the air kerma rate measured with the A4 ion chamber.

When a photon beam is not attenuated in a volume and in the condition of charged particle equilibrium of the second electrons, the absorbed dose in the medium is related to the electron fluence as follows (Podgorsak, 2005):

$$D_{med} = \Phi_{med} \left(\frac{\bar{S}_{col}}{\rho} \right)_{med} \tag{4.6}$$

The term $\left(\frac{\bar{S}_{col}}{\rho}\right)_{med}$ in Eq (4.6) is the spectrum averaged collisional stopping power and Φ_{med} is the total fluence of electrons in the medium.

The fluence of radiation remains unchanged when it is passing through these small counters filled with a low pressure gas. Therefore, the conditions of the Bragg-Gray cavity theory are met for these counters. As a result, the total dose rate of monoenergetic photons in the wall of Cy-TEPC and the Cy-GPC can be calculated by multiplying the quotient of averaged stopping powers to the absorbed dose rate in the cavity (Podgorsak, 2005):

$$\dot{D}_{wall} = \dot{D}_{Cavity} \times \left[\left(\frac{\bar{S}_{col}}{\rho} \right) \right]_{\frac{wall\ material}{TE\ gas}} \tag{4.7}$$

Under the true Charged Particle Equilibrium (CPE) condition, the absorbed dose in the medium is equal to the collisional kerma:

$$\left(\dot{K}_{col}\right)_{wall} = \dot{D}_{wall} \tag{4.8}$$

On the other hand, the collisional kerma in two different materials are related to each other as follows:

$$\frac{K_{col,2}}{K_{col,1}} = \frac{\psi_2 \left(\frac{\bar{\mu}_{en}}{\rho}\right)_2}{\psi_1 \left(\frac{\bar{\mu}_{en}}{\rho}\right)_1} = \psi_{2,1} \left(\frac{\bar{\mu}_{en}}{\rho}\right)_{2,1} \tag{4.9}$$

In which ψ is the energy fluence of the radiation beam and $\left(\frac{\bar{\mu}_{en}}{\rho}\right)$ is the averaged mass energy absorption coefficient of the photons. When the energy fluence of the photon beam can be assumed to be the same in the two materials, the term $\psi_{2,1}$ is equal to 1 (Podgorsak, 2005) and the ratio of the collisional kerma in the two media is equal to the ratio of the mass energy absorption coefficients of them:

$$\frac{K_{col,2}}{K_{col,1}} = \left(\frac{\bar{\mu}_{en}}{\rho}\right)_{2,1} \tag{4.10}$$

Equation (4.10) can be used to convert the kerma rate in the counter wall to the air kerma rate by dividing the kerma values by the live time of the measurement. Therefore, the air kerma rate equivalent to the kerma rate in the wall material is equal to:

$$\dot{K}_{air} = \left(\dot{K}_{col}\right)_{wall} \times \left[\left(\frac{\bar{\mu}_{en}}{\rho}\right)\right]_{\frac{air}{wall\ material}} \tag{4.11}$$

Assuming that the CPE condition is approximately satisfied, the $\left(\dot{K}_{col}\right)_{wall}$ can be replaced by the dose rate in the wall according to the equation (4.8). By replacing the dose rate in the wall according to the equation (4.7) the final equation for the air kerma rate will be:

$$\dot{K}_{air} = \dot{D}_{Cavity} \times \left[\left(\frac{\bar{S}_{col}}{\rho}\right)\right]_{\frac{wall\ material}{TE\ gas}} \times \left[\left(\frac{\bar{\mu}_{en}}{\rho}\right)\right]_{\frac{air}{wall\ material}} \quad (4.12)$$

Since the photons of the X-Ray and Gamma Radiation are assumed monoenergetic, the averaged mass energy absorption coefficient is a unique value for each photon beam. But, because photons interact with matter in various ways, even a monoenergetic photon beam produces electrons with a wide range of energy. Therefore, the mass stopping power of the electrons should be averaged for all the electrons created by each photon beam. Without advanced computational methods it is difficult to determine the distribution and mean energy of electrons produced by the photon beam in different materials. Thus, the average energy of the electrons produced by each photon beam of a given energy has been estimated, and the mass stopping power of electrons with that energy applied in equation (4.12). For example, the low energy photons (e.g. 20 keV and 80 keV X-Ray beams) mainly interact with matter through the photoelectric effect and give almost all their energy to the produced photoelectrons. Therefore, the energy of these electrons can be assumed as almost the same as the photon beam energy. On the other hand, for higher energy photons (100 keV X-Rays to ~ 1 MeV gamma rays) the predominant interaction of photons with matter is the Compton Effect. The approximate average energy of the electrons released in the Compton interaction process has been assumed to be equal to 30% of the incident photons energy based on the information provided in Figure 7.7 of "Introduction to Radiological Physics and Radiation Dosimetry" by Frank H. Attix (Attix, 1986). The mass stopping power of the electrons with the third energy of the photon beam is then applied to the equation (4.12).

This may seem an imprecise method for finding the averaged mass stopping power. But, since there is a ratio of two mass stopping powers in the equation, both calculated in the same way, their uncertainties would be of the same order and the ratio should not change significantly.

In addition to the absorbed dose rate, two other averaged microdosimetry quantities were also useful in our investigations. One of them is the frequency-mean lineal energy, $\bar{y}_F$, which shows the mean value of the frequency distribution of y, f(y):

$$\bar{y}_F = \frac{\sum y_i . f(y_i)}{\sum f(y_i)} \tag{4.13}$$

The other one is the dos-mean lineal energy, $\bar{y}_D$, which is the mean value of the dose distribution:

$$\bar{y}_D = \frac{\sum {y_i}^2 . f(y_i)}{\sum y_i . f(y_i)} \tag{4.14}$$

These two quantities have been also calculated and compared for measured data with the counters in each set of experiments (Table 4-5).

4.4.2 X-Ray measurements

The x-ray production process involves accelerating electrons using a high voltage and directing them towards the anode material. When the electrons hit the anode, they interact with the atoms in the material, causing the atoms to emit a continuous x-ray spectra produced with a broad energy distribution.

The ISO N beams are a series of narrow-spectrum x-ray beams produced by an x-ray tube with a specially designed anode material. The anode material is made of a mixture of elements that generate characteristic x-rays with a narrow energy distribution centered around a specific energy value when bombarded by electrons.

The x-ray spectra of ISO N beams can be further modified by applying different filters and high voltages to remove unwanted x-rays and produce a quasi-Gaussian spectrum of energies with a mean value equal to the intended amount of energy. This can improve the contrast and resolution of the resulting images and make the beam more useful for specific applications, such as material analysis or medical imaging. The X-ray beams are designated as N-***, with *** denoting the applied high voltage in kilovolts to the X-ray generator (Belhaj et al.).

In this study, an X80 Model X-Ray Beam Irradiator (Hopewell Designs Inc.), ISO N Series with an X-Ray range of 20 - 120 kV, and a power of up to 4.2 kW was used to produce X-Rays. Three X-Ray measurements were made with each of the Cy-TEPC, Cy-GPC and the A4-ion chamber. The energy of the X-Rays was 20 keV, 65 keV and 100 keV.

In each experiment the appropriate filter material and high voltage were selected from the irradiator manual to produce the desired radiation quality. The counter was placed at a

distance of 1m from the surface of the filter, and at a height of 110 cm from the floor, so that it was levelled with the X-Ray beam. The X-ray generator collimator was chosen to ensure complete coverage of the counters at the 1 meter position.

Each experiment was run for duration of ~1000 s with the Cy-TEPC and the Cy-GPC. The position of the counter in front of the X-Ray irradiator is shown in Figure 4-12.

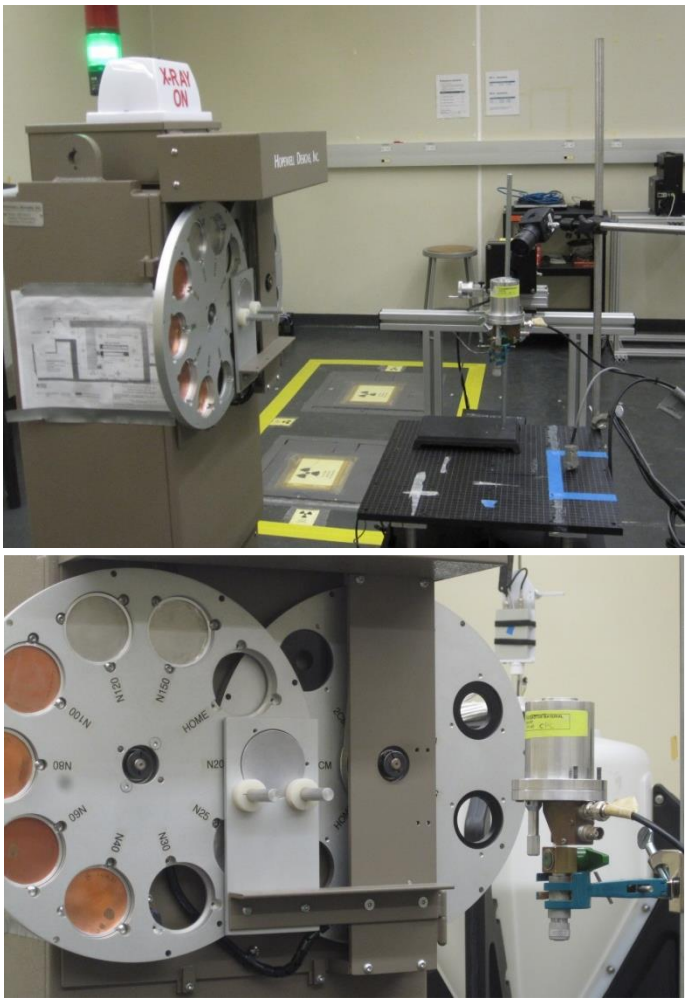

Figure 4-12 Position of counters in front of the X-Ray irradiator

The pulse height measurement data was then converted to normalized dose rate spectra using the MATLAB code. The total absorbed dose rates measured with these counters were also calculated and converted to the average air kerma rates to be compared to the A4-ion chamber measurements. The ion chamber was set to measure the X-Ray dose for 12 sets of 20 s. The average dose of these measurements was then calculated and divided by 20 s to obtain the average dose rate. The comparison of the dose rate spectra of these measurements are shown in Figure 4-14 to Figure 4-16. The air kerma rate measured by the Cy-TEPC, Cy-GPC and the ion chamber are also compared in Table 4-6 to Table 4-8.

4.4.3 Gamma measurements

The event size spectra and the dose rate of the G10 gamma irradiator of the Ontario Tech University ERCB506 Lab was measured with the Cy-TEPC, Cy-GPC and the A4- ion chamber. The gamma source is a 7.9 Ci Cs-137 which emits gamma radiation with the energy of 0.662 MeV. Our final step in this series of experiments was to measure the mixed radiation field of 2.5 MeV neutrons and Cs-137 gamma rays. The idea was to subtract the gamma event-size spectrum from the mixed-field event-size spectrum to find the pure neutron spectrum. Therefore, the gamma radiation field was chosen to be the same as in the planned mixed-field experiment. Therefore, it is necessary to demonstrate that the Cy-TEPC and Cy-GPC have the same sensitivity to 0.662 MeV gamma rays.

A helpful place to start the mixed-radiation field measurements seemed to be a point where received equal dose equivalent rates from neutron and gamma sources. A neutron spectrometer along with an ion chamber were used to find the dose equivalent rates from

both the sources and it was found that the neutron dose equivalent rate at a distance of 20-30 cm from the P385 neutron generator was almost the same as the photon dose equivalent rate at 4 m away from the G-10 source, when a 10X attenuator plate was applied in front of the G10 source collimator to reduce the intensity and hence the dose rate of gamma rays. Thus, it was appointed that for making the measurements in the mixed-field of 2.5 MeV neutrons and Cs-137 photons, the counters were placed at a point perpendicular to the neutron and gamma sources at the aforementioned distances. Furthermore, the gamma dose rate measurements were conducted at a distance of 4 m from the G10 gamma source to give an approximation of the photon dose rate at the point where the mixed-field measurements were set to be made. Gamma measurements were conducted with the Cy-TEPC and the Cy-GPC for around 10000s, so that it was sure that sufficient amount of data had been collected. The gamma measurement with the A4- ion chamber however was carried out for 12 sets of 20s.

In addition to the gamma measurements which were made separately with the Cy-TEPC and the Cy-GPC, another experiment was also conducted to measure the gamma dose rate with both counters simultaneously (Figure 4-13). In this experiment the two counters were mounted side by side, so that the midpoint between the counters was adjusted to a distance of 2 m from the center of the gamma source. The obtained event-size spectra in these measurements are shown in Figure 4-17 and Figure 4-18, and the comparison of the air kerma rates as well as the corresponding statistical uncertainties are shown in Table 4-9.

Figure 4-13 Simultaneous Cs-137 Gamma measurements with Cy-TEPC and Cy-GPC

4.4.4 Result analysis for photon experiments

The frequency-mean lineal energy ($\bar{y}_F$) and the dose-mean lineal energy ($\bar{y}_D$) and their relative counting statistics ($\frac{\sigma_{\bar{y}_F}}{\bar{y}_F}$ and $\frac{\sigma_{\bar{y}_D}}{\bar{y}_D}$) were also calculated in each experiment. The results are summarized in the Table 4-5:

Table 4-5 Frequency mean lineal energy and dose-mean lineal energy for photon measurements

Radiation Energy	0.662 MeV Gamma Ray		100 keV X-Ray		65 keV X-Ray		20 keV X-Ray	
Counter	Cy-TEPC	Cy-GPC	Cy-TEPC	Cy-GPC	Cy-TEPC	Cy-GPC	Cy-TEPC	Cy-GPC
$\bar{y}_F$	0.452	0.468	1.711	1.884	1.596	1.7495	2.471	2.3197
$(\frac{\sigma_{\bar{y}_F}}{\bar{y}_F})$	7.4e-4	7.5e-4	1.1e-3	1.4e-3	1.1e-3	1.3e-3	1.6e-3	1.9e-3
$\bar{y}_D$	1.867	1.829	3.706	3.710	3.482	3.5062	4.362	4.0479
$(\frac{\sigma_{\bar{y}_D}}{\bar{y}_D})$	2.2e-3	2e-3	1.8e-3	2.1e-3	1.8e-3	1.9e-3	2.3e-3	2.8e-3

The normalized dose distributions and the calculated air kerma-rates are also shown in the following figures and tables.

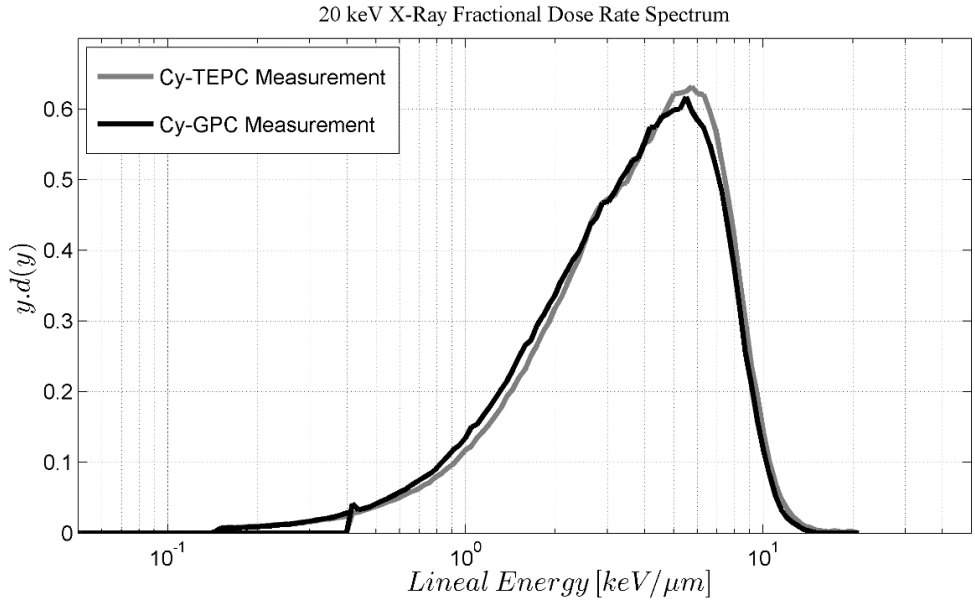

Figure 4-14 Normalized dose rate spectra of monoenergetic 20 keV X-ray, measured with Cy-TEPC and Cy-GPC at a 1m distance for a live time of ~1000s.

Table 4-6 Air kerma rates of 20 keV X-Ray measured with the Cy-TEPC, Cy-GPC, and A4-Ion Chamber

Counter	Air Kerma-Rate (μGy/s)
Cy-TEPC	1.697±0.002 (μ/ρ=0.7 cm^2/g)
Cy-GPC	2.070±0.003 (μ/ρ=0.44 cm^2/g)
A4-Ion Chamber	2.538

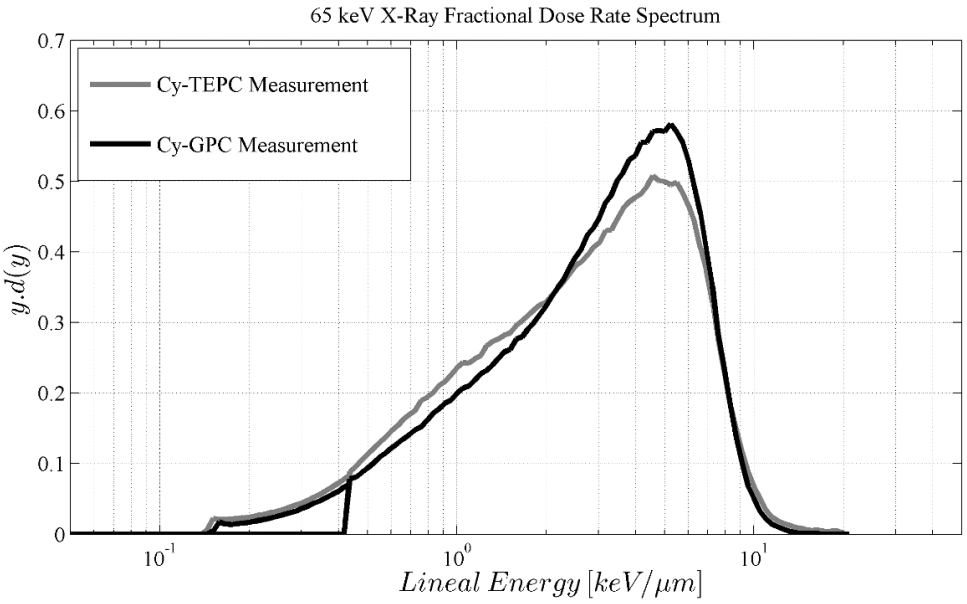

Figure 4-15 Normalized dose rate spectra of monoenergetic 65 keV X-ray, measured with Cy-TEPC and Cy-GPC at a 1m distance for a live time of ~1200s

Table 4-7 Air kerma rates of 65 keV X-Ray measured with the Cy-TEPC, Cy-GPC, and A4-Ion Chamber

Counter	Air Kerma-Rate (μGy/s)
Cy-TEPC	2.135±0.002 (μ/ρ=0.2 cm^2/g)
Cy-GPC	2.051±0.002 (μ/ρ=0.17 cm^2/g)
A4-Ion Chamber	1.290

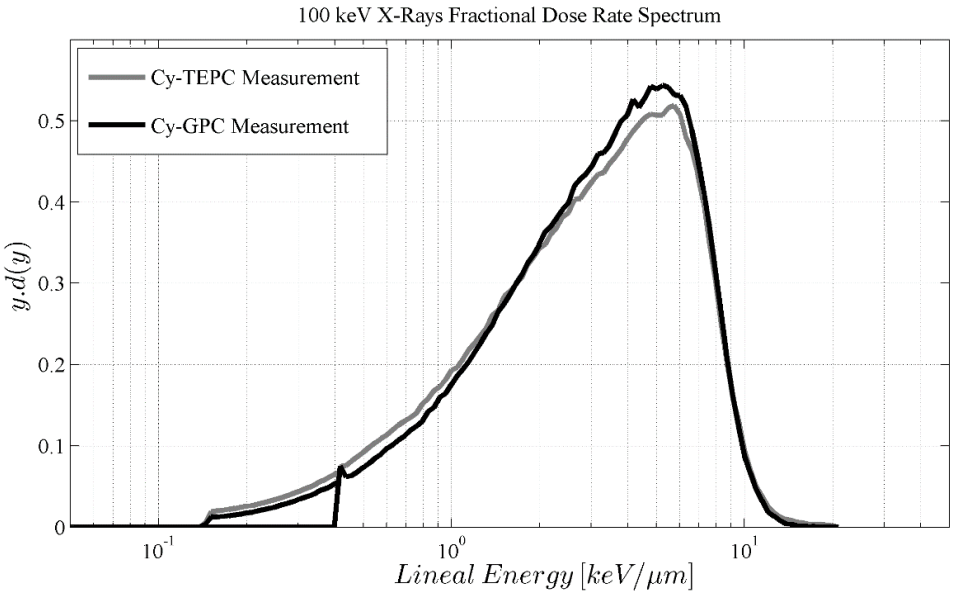

Figure 4-16 Normalized dose rate spectra of monoenergetic 100 keV X-ray, measured with Cy-TEPC and Cy-GPC at a 1m distance for a live time of ~1000s

Table 4-8 Air kerma rates of 100 keV X-Ray measured with the Cy-TEPC, Cy-GPC, and A4-Ion Chamber

Counter	Air Kerma-Rate (μGy/s)
Cy-TEPC	2.242±0.002 (μ/ρ=0.168 cm^2/g)
Cy-GPC	2.300±0.002 (μ/ρ=0.151 cm^2/g)
A4-Ion Chamber	1.617

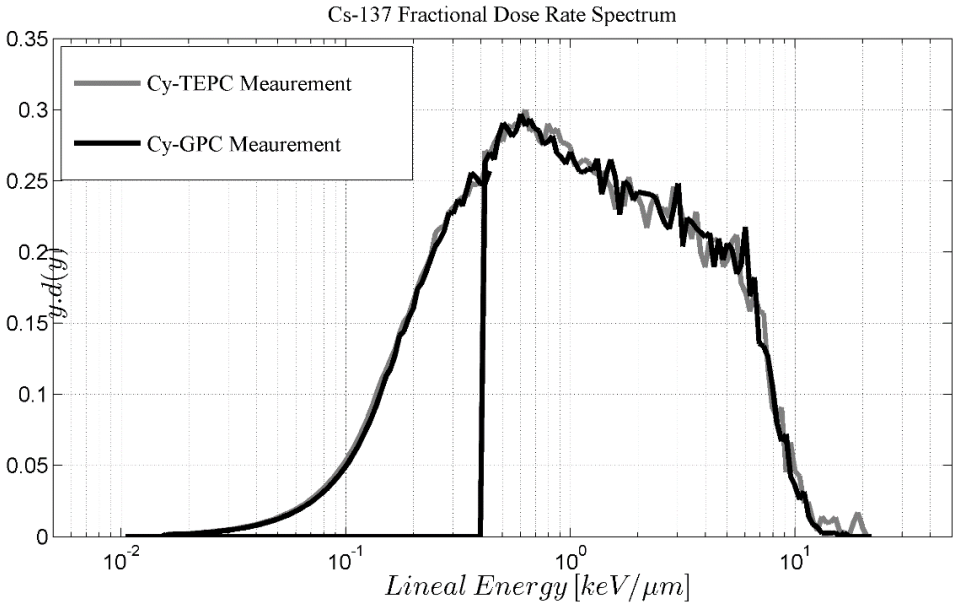

Figure 4-17 Normalized dose rate spectra of Cs-137 gamma source with 10x attenuator, measured with Cy-TEPC and Cy-GPC at a 2 m distance for a live time of ~2000s

Table 4-9 Air kerma rates of 0.662 MeV gamma ray measured with the Cy-TEPC, Cy-GPC, and A4-Ion Chamber

Counter	Air Kerma-Rate (μGy/s)
Cy-TEPC	0.543±0.0004
Cy-GPC	0.523±0.0004
A4-Ion Chamber	0.528

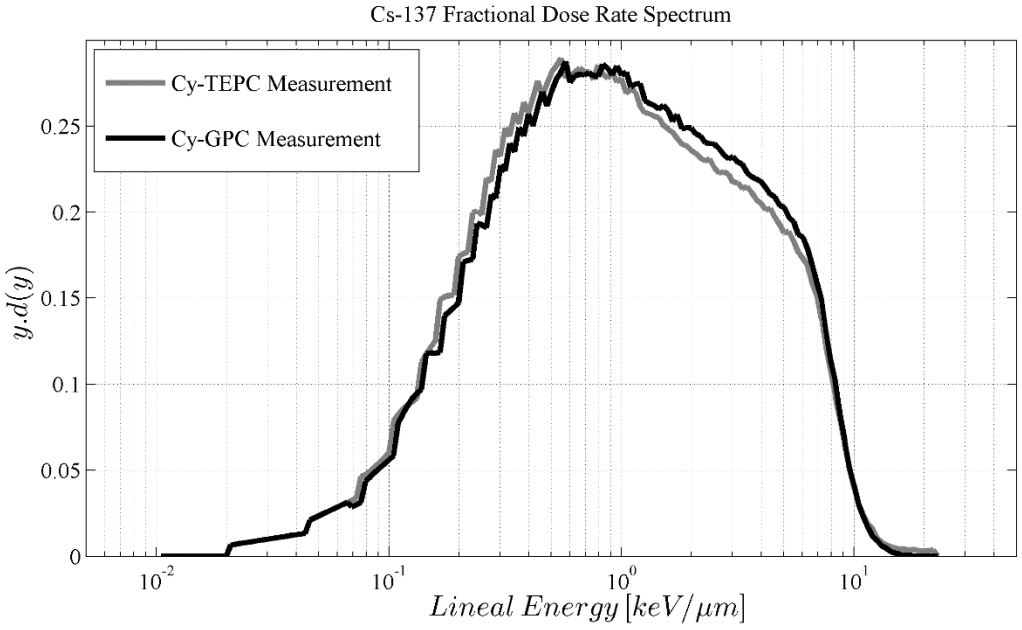

Figure 4-18 Normalized dose rate spectra of Cs-137 gamma source, measured simultaneously with Cy-TEPC and Cy-GPC at a 2 m distance for a live time of ~3000s

As can be seen in Figure 4-14 to Figure 4-18, there is a very good agreement between the dose distributions of photons with different energies measured with the Cy-TEPC and the Cy-GPC. The shapes of the compared spectra in each case are almost identical and the electron edges are at the same position. The two counters also show close similarity in $\bar{y}_F$ and $\bar{y}_D$ for different photon energies (Table 4-5). This gives confidence that the Cy-TEPC and the Cy-GPC have similar sensitivity to photon radiation.

In order to investigate the photon measurement accuracy of the two counters the calculated air kerma rate for the Cy-TEPC and the Cy-GPC were compared with the A4-ion chamber measurement in each case (Table **4-6** to Table **4-9**). As it can be seen in Table **4-9**, the

average dose rates of the 0.662 gamma radiation of Cs-137 measured by the three counters are in a good agreement. This is very encouraging regarding the reliability of the Cy-TEPC and Cy-GPC gamma measurement. However, for the X-Ray measurements the air kerma rates are slightly different for the three counters (Table **4-6** to Table **4-8**). For the 100 keV and 65 keV X-Ray measurements, the calculated air kerma for the Cy-TEPC and the Cy-GPC are close to each other. However, they are different with the A4-ion chamber measurements. For the 20 keV X-ray the three counters show different air kerma rates.

The reason of these differences might be the approximate approach was applied to find the mass stopping power of the secondary electrons produced by photons. Another possibility is that the wall of the Cy-TEPC and the Cy-GPC has a significant absorption effect to the incident X-Rays. Therefore, the flux of the radiation no longer remains unchanged and the "Bragg-Gray" condition cannot be applied to this situations. The other issue is that the A4. Ion chamber is calibrated for the Cs-137 gamma radiation. Thus, its response to X-Rays might not be as accurate as for the Cs-137 gamma radiation. Further investigation on these responses should be done in future work. However, the good agreement between the air kerma measurements of 0.662 MeV gamma radiation shows that the Cy-TEPC and Cy-GPC measure this gamma radiation accurately. Furthermore, the dose received by workers in nuclear power plants is mainly due to high energy gamma rays (90%) rather than low energy X-rays (10%) (Furuta, Nishide, Kudo, & Saigusa, 2020). Therefore, the effect of high energy gammas is more significant in the mixed field dosimetry of these facilities and is more important to be considered carefully. Consequently, the photon component of the first mixed-field radiation studied in this research was selected to be the Cs-137 gamma rays.

4.5 Investigation of Cy-TEPC and Cy-GPC response to 2.5 MeV neutrons

The pure neutron radiation field, which was available at the Ontario Tech University, was produced by a neutron generator that emits 2.5 MeV neutrons. These neutrons were used to investigate the neutron response of the two counters. The details of the neutron radiation field and the measurement results are explained in the following sections.

4.5.1 2.5 MeV neutron field of the Ontario Tech University neutron generator

The P385 - Neutron Generator produces neutrons through the DD-fusion reaction below:

$$D + D \rightarrow n + 3He$$

The average energy of the neutrons is 2.5 MeV. A normal by-product of the production of these neutrons are X-Rays which have a broad peak around 70 keV (Wharton et al., 2011). These X-rays are localized around the ion source in front of the target and the intensity declines quickly along the generator tube. They can be blocked by a thin lead shield, 3.2 mm (1/8 inch) thick (Al-Bayati, 2012). We applied such a lead shield to the neutron generator for measuring only the neutron radiation. In addition to the Cy-TEPC and the Cy-GPC, the 5" chamber was used to verify the measurements of these two counters.

As mentioned in section 4.4.3, for mixed field measurements, the distance between the counters and the neutron source should be ~20 cm, so that the dose equivalent rate of the neutrons is approximately the same as that of gamma radiation at a 4m distance. Therefore, the neutron measurements were also made at the same position against the neutron generator.

In each experiment, the counter was placed in front of the neutron generator target at a distance of 20 cm and measured the neutrons for a live time of ~10000s (Figure 4-19).

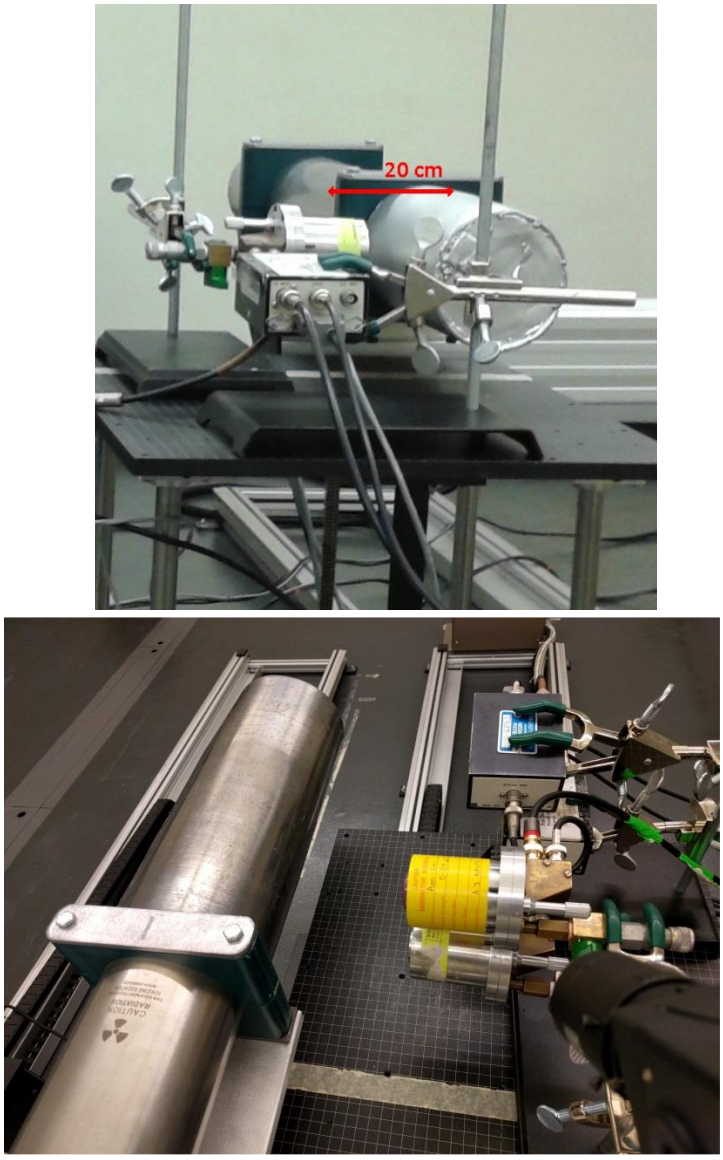

Figure 4-19 Twin counters in front of the neutron generator at a distance of 20 cm, Upper picture: Lead shield on, Lower picture: Lead shield off.

4.5.2 Result analysis for neutron experiments

The very low sensitivity of the Cy-GPC to neutrons compared to the Cy-TEPC and the 5" spherical TEPC is obvious from Figure 4-20. In order to verify the similarity of the neutron response for the Cy-TEPC and the 5" TEPC the normalized diagrams have also been plotted in Figure 4-21.

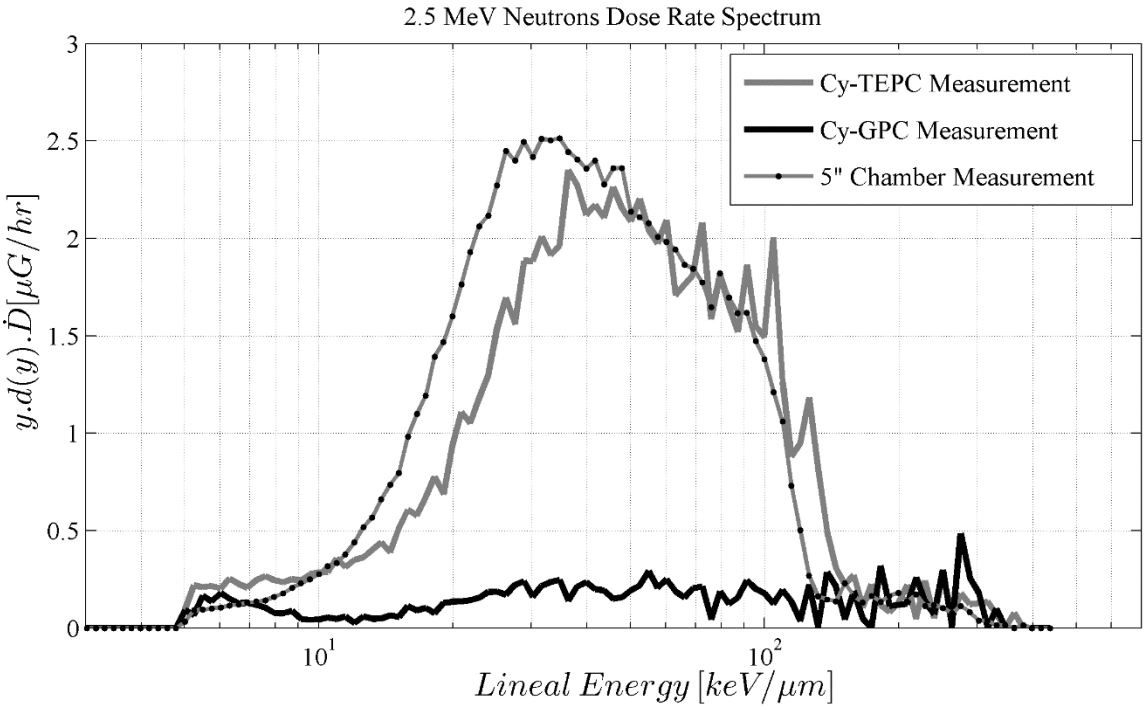

Figure 4-20 Dose rate spectra of P385 Neutron Generator (20 cm distance), measured using Cy-TEPC, Cy-GPC and 5" Chamber for a live time of ~10000s.

According to this figure, the neutron event-size spectra measured by the Cy-TEPC and the 5" TEPC have very similar shapes. However, the proton edges of these two spectra are not at the same place and the spectrum measured by the cylindrical counter looks shifted to higher lineal energies compared to the spherical counter measurements. This means that the protons

which transfer along the longest chord in the Cy-TEPC cavity deposit higher lineal energies in the counter compared to the protons which traverse the diameter of the 5” spherical TEPC. It is worth mentioning that both counters simulate a 2μm cell size and the gas pressure inside the 5” counter is lower than the Cy-TEPC gas pressure. Since these measurements have been repeated several times and the same results obtained, it was unlikely that this difference was due to a fault in the counters or calibration issues. For more investigations, these measurements were modeled in PHITS and these results were replicated in the simulation (Figure 5-9).

After considering the chord length distribution in different volumes, it was found that the ultimate justification for this problem is the difference in geometry and shape of the two counters. Further discussion is carried out in section 6.2. Nevertheless, the overall agreement in response of the Cy_TEPC and the 5” TEPC is sufficient for us to verify the reliability of the Cy-TEPC neutron measurement.

Figure 4-20 also shows that the Cy-GPC has very low sensitivity to neutrons, specifically in the 10 to 20 keV/μm range of lineal energy, which overlaps with photon event-size spectrum. According to the data presented in Table 4-10, the dose rate measured by the Cy-GPC for the events between 9 to 25 keV/μm, is ~14% of the dose rate measured by the Cy-TEPC in this area and ~9% of the 5”TEPC measured dose rate.

The few events recorded with lineal energy below100 keV/μm are generated by protons due to neutron interactions with the hydrogen atoms of the tissue equivalent gas inside the Cy-GPC cavity. The events with lineal energies larger than100 keV/μm are assumed to be

created by heavier ions, which in this case are carbon recoils that come from neutron-carbon elastic scattering in the graphite wall of the Cy-GPC. These results were reproduced in simulations and are discussed in section 5.1.1.

Table 4-10 2.5 MeV neutron dose rate measured with 5"TEPC, Cy-TEPC and Cy-GPC

2.5 MeV neutron measurements	5" TEPC	Cy-TEPC	Cy-GPC
Total dose rate (μG/hr)	94.29	85.72	13.25
Dose rate for 9 <y< 25 keV/μm (μG/hr)	21.25	12.86	1.84

A further experiment was also carried out to measure the dose rate spectrum of the P385 neutron generator radiation with the Cy-TEPC and the Cy-GPC simultaneously. The result spectra, which are shown in Figure 4-22, are in good agreement with the spectra in Figure 4-20.

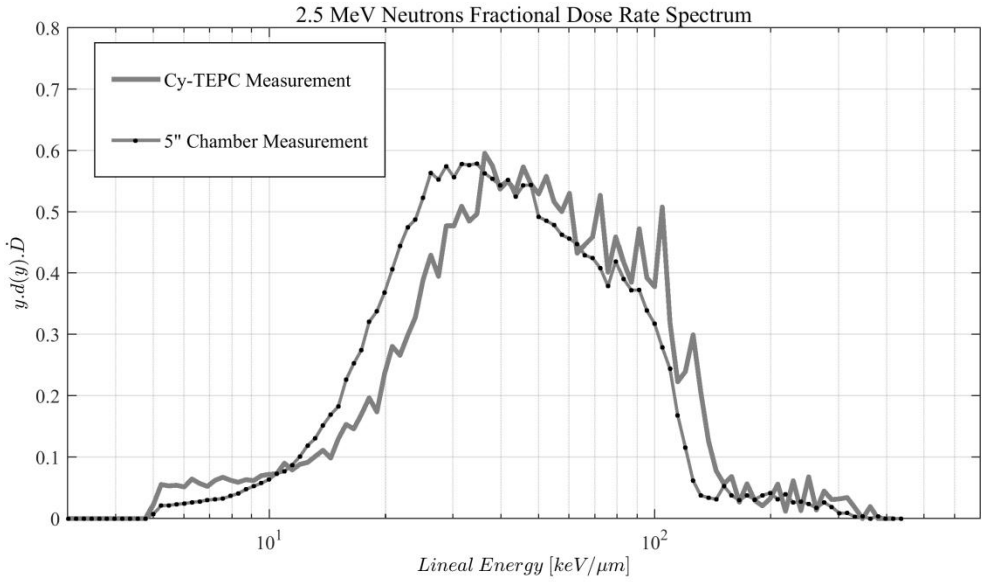

Figure 4-21 Normalised dose rate spectra of P385 Neutron Generator (20 cm distance) measured using Cy-TEPC, Cy-GPC and 5" Chamber for a live time of ~10000s.

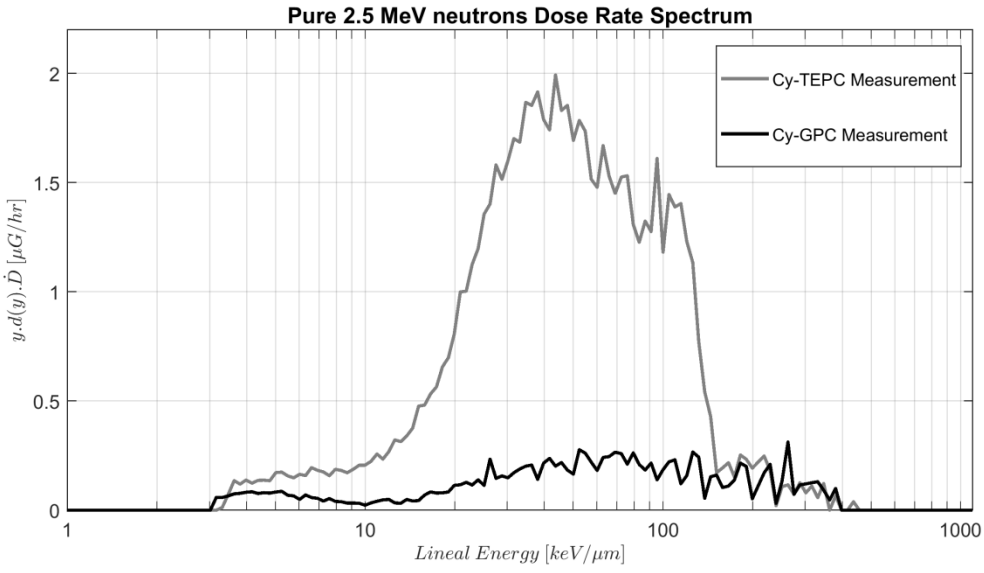

Figure 4-22 Dose rate spectra of P385 Neutron Generator measured simultaneously with Cy-TEPC and Cy-GPC (20 cm distance) for a live time of ~8000s

After verifying that the Cy-TEPC and the Cy-GPC have very similar sensitivity to photons, and the Cy-GPC is almost insensitive to neutrons, the two counters were used in different neutron-gamma mixed-field measurements to find the neutron component.

4.6 A brief description of the PHITs code and the sections used in this study

The other goal of this study is to benchmark PHITS code simulations against experimental data collected through measurements and to explore how simulation can assist in the analysis of experimental results. The final aim is to gain confidence that the code could provide useful information in those situations where measurement may not be possible. A requirement to simulation fidelity is to develop a representative geometric model of the counter and make a virtual space for particle transport calculations. In PHITS, the components of the counter are modeled as closed volumes called cells. Each cell consists of a combination of geometrical surfaces which are precisely defined with respect to a reference frame. All components of the counters were simulated with exact dimensions and details for both the Cy-TEPC and the Cy-GPC which are similar to each other geometrically. These counters have elaborate structures, and it is important to ensure that all dimensional details have been captured accurately, without any missing parts or any overlap between the cells. In this thesis, SimpleGeo, which is an interactive solid modeler, is used for geometrical modeling. This software provides the capability to export the geometric details of the counter in a text format compatible with the PHITS input code. A schematic view of the SimpleGeo model for the cylindrical counters studied in this thesis is shown in Figure 4-23.

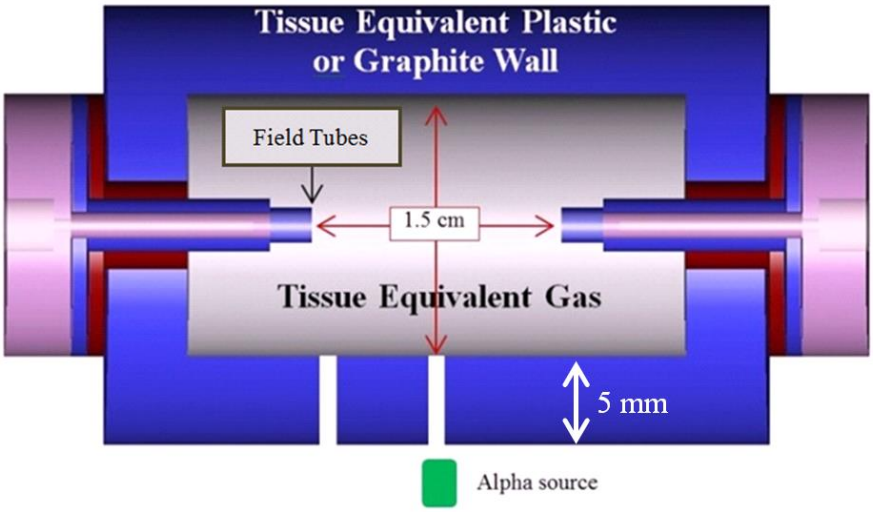

Figure 4-23 Cross sectional view of the Cy-TEPC and Cy-GPC modelled by SimpleGeo

Another counter that is used as a benchmark for the cylindrical counters performance is a 5" spherical tissue equivalent counter. The geometry of this counter is simple enough that can be modeled directly in the PHITS code (Figure 4-24). After establishing the geometrical details of a counter, the material for every component is defined for PHITS. Figure 4-25 shows the cylindrical counters geometry and the material of every component.

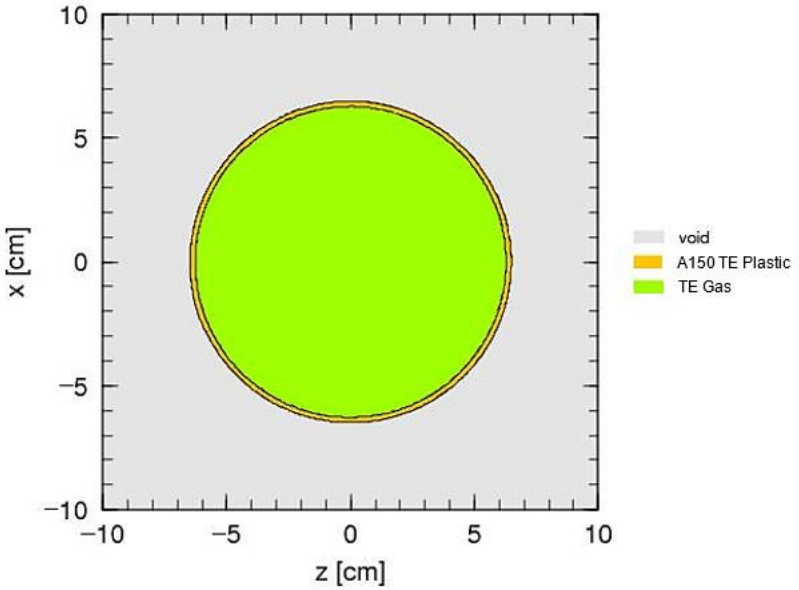

Figure 4-24 Cross sectional view of the 5" spherical TEPC, modelled by PHITS

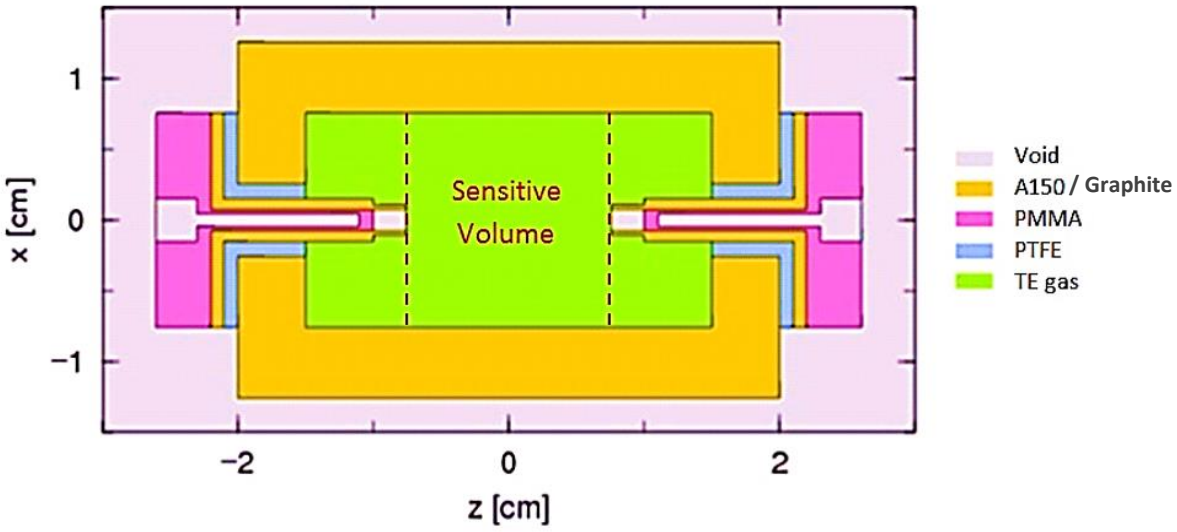

Figure 4-25 Cross sectional view of the Cy-TEPC/Cy-GPC showing every component material, modelled by PHITS

The elemental chemical composition of each material in the cylindrical counters is shown in Table 4-11. In order to determine the material composition for PHITS textual input in the [Material] section, each material is defined by its constitutive nuclides and either their particle density (atoms/cm^3) or mass density (g/cm^3).

In order to do the transport calculations effectively in PHITS, it is necessary to specify the region of interest for the counter. In the case of the Cy-TEPC and the Cy-GPC, the region of interest is the sensitive volume, which is a right cylinder with the height and diameter of 1.5 cm in the center of the gas cavity. The reason that this volume rather than the whole cavity is considered the region of interest is that the electrical field inside the cavity is defined by the field-tubes and is uniform only in the right cylindrical region at the center of the cavity between the two field-tubes. Therefore, electrons which are created in the region outside the sensitive volume are collected by the field-tubes and do not drift to the anode wire. As a result, they do not make a contribution in creating the voltage drop, and hence in the output pulse of the counter.

For the 5" spherical counter however, the region of interest is the whole spherical cavity inside the counter as electric field-shaping anode-wire supports ensure a uniform gas-gain along the whole length of the anode (A. J. Waker, 1986)

Table 4-11 Elemental composition of the Cy-TEPC/Cy-GPC constitutive material

Material	**Elemental Chemical Composition**				
Tissue Equivalent Gas (Propane based)	H (10.3%)	C (56.9%)	N (3.5%)	O (29.3%)	
A-150 Tissue Equivalent Plastic	H (10.1%)	C (77.6%)	N (3.5)	O (5.2%)	F (1.7%)
Graphite	(100%)				
Poly (methyl methacrylate), Plexiglass (PMMA)	H (53.4)	C (33.3%)	O (13.3%)		
Polytetrafluoroethylene, Teflon) (PTFE)	C (33.33%)	F (66.67%)			

After defining the details of the counter geometry and material, the characteristics of the radiation source were determined.

The radiation source in all simulations in this thesis is defined as a 2x2 cm^2 square at a distance of 20 cm from the counter center. For the polyenergetic neutron sources, the neutron energy spectrum has been digitized and defined for the code.

The output of the code is intended to show the distribution of deposited energy by the charged particles created in the counter. This distribution is achievable using the Tally [T-Deposit]. In this tally, the user can determine the specifications of the deposited energy spectrum such as the minimum and maximum of the deposited energy values to be considered, the number of energy groups, and most importantly, the secondary particle whose deposited energy should be calculated. Region of interest and the material in which the deposited energy should be scored are also specified in this tally.

There are also some general parameters such as calculation mode, cut off energy, switching energy, model options, etc. which should be determined for the code based on the physics of the studied radiation field.

The input files of some of the simulations conducted in this study are presented in Appendix D.

In order to compare PHITS simulations against the measurements, some neutron radiation fields with different energies were studied and the results are presented and discussed in the following chapters.

As it was mentioned before, the main challenge in discrimination of the neutron and gamma absorbed dose in a mixed-radiation field occurs in the lineal energy range of 10 to 25 keV/μm. This range is the overlap area for the events created by neutrons and photons interaction with matter. Therefore, the main purpose of this research was to compare the Cy-GPC and the Cy-TEPC responses in this range of lineal energy. For this purpose, several measurements and simulations were conducted in five different mixed radiation fields to

evaluate the two counters performance in a radiation fields with different neutron and gamma components and a wide neutron energy range.

The five radiation fields are as follows: 1) Mixed-field of 2.5 MeV neutrons from the P385 neutron generator and 0.662 MeV photons from the Cs-137 source, at the Ontario Tech University radiation facility. 2) Simulation of the 14.8 MeV Neutron Irradiation at the University of Leeds laboratories. 3) Broad spectrum of ^{241}Am-Be neutrons. 4) Neutrons generated in the Reactor Materials Testing Laboratory (RMTL) of Queen's University at Kingston, Ontario. 5) Neutron radiation field at the European Organization for Nuclear Research (CERN). The details and results of these measurements and simulations are explained in chapters 5 to 9.

Chapter 5

Study of Neutron Gamma Mixed Radiation Field at the Ontario Tech University Facility

The two counters responses to gamma rays and neutrons were studied for 0.662 MeV gamma radiation and 2.5 MeV neutrons respectively. Therefore, the mixed-field of these two radiations was an appropriate choice to be measured with both the counters to see if the neutrons event-size spectrum can be obtained by subtracting the photons event-size spectrum, measured by the Cy-GPC, from the mixed-field event-size spectrum, measured by the Cy-TEPC. The measured spectra was then compared to the 2.5 MeV neutron event-size spectra obtained by simulating the two counters in the PHITS code.

5.1.1 Measurements

The main purpose of performing a measurement in this mixed-radiation field was to investigate the response of the twin counters in the lineal energy range of 10 to 25 keV/μm, which was the overlap area for the events created by neutron and photons in this experiment. For this purpose, the two counters were put one above the other, at a distance of 4m from the Cs-137 gamma source and 20 cm from the P385 neutron source, so that the photon beam and the neutron beam were perpendicular to each other. Figure 5-1 shows a schematic view of this experimental set-up.

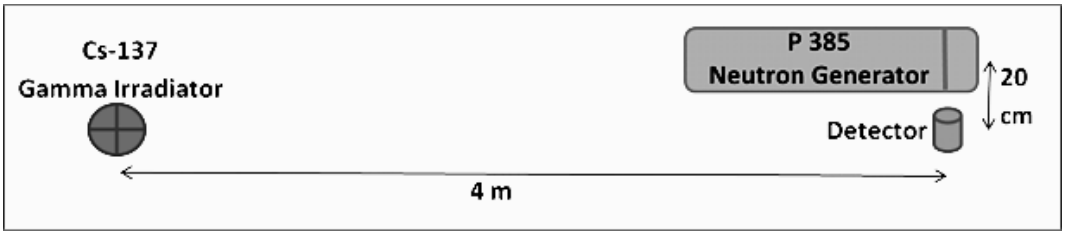

Figure 5-1 Experimental set-up of 2.5 MeV neutrons and 0.662 MeV photons mixed-field measurements

The arrangement of these measurements was similar to the schematic shown in Figure 5-2. Different high voltages (HV) were applied to each counter anode to establish a suitable gas gain in order for each counter to measure the entire event size spectrum for photons (Cy-GPC) or neutrons (Cy-TEPC). The output pulses of each counter were amplified and shaped in a pre-amplifier and a digital pulse processer (DPP), then sorted and stored by pulse-height. The frequency distribution of the pulses from both of the counters were then stored in the PC for post-measurement analysis. Figure 5-3 shows the results of this measurement.

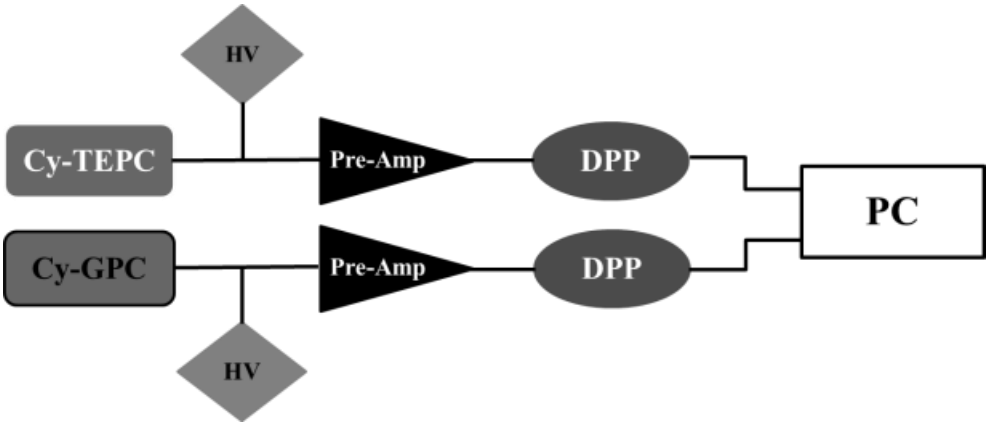

Figure 5-2 Schematic view of experiments arrangement

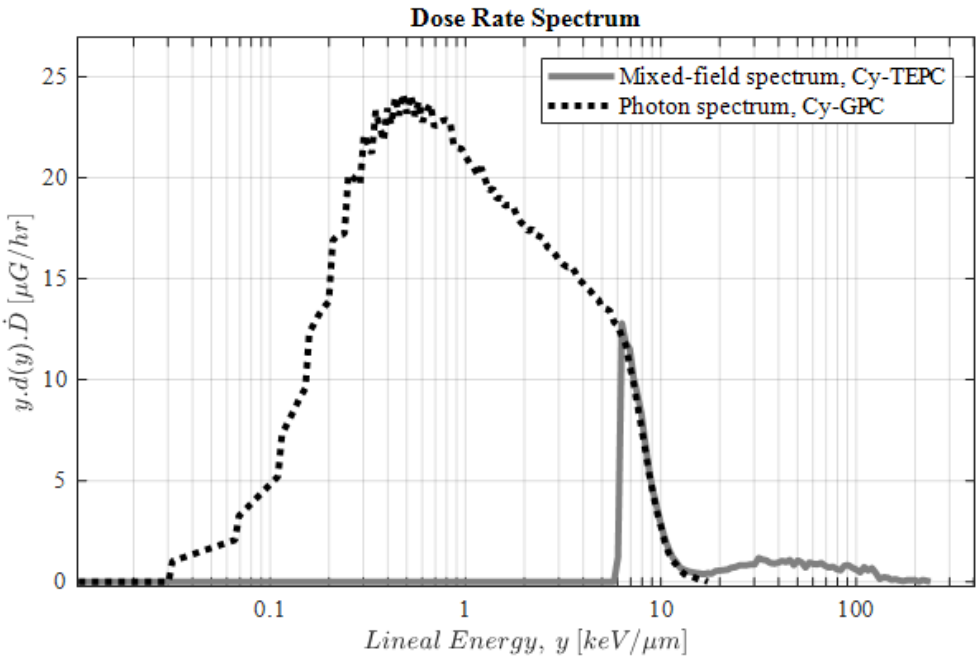

Figure 5-3 Dose rate spectra of P385 Neutron Generator (30 cm distance) and Cs-137 Gamma source (4m distance) mixed-field, measured with Cy-TEPC and Cy-GPC simultaneously.

Because of the gas gain limitation of the Cy-TEPC, it was not possible to measure all the events created by photons and neutrons with this counter. Considering the amplifier gain used for the Cy-TEPC, the widest lineal energy range which could be covered in the event-size spectrum measured with this counter was from 6 keV/µm to 300 keV/µm. This lineal energy range involves the overlap area with the Cy-GPC measurement spectrum, but not the events below 6 keV/µm. However, the spectrum measured by the Cy-TEPC matches perfectly to the photons dose rate spectrum measured by the Cy-GPC for lineal energies between 6 to ~20 keV/µm. The similar response of the two counters to photons was also previously demonstrated in section 4.4. Therefore, in order to determine the pure neutron

spectrum, the photon spectrum measured by the Cy-GPC above 6 keV/μm was subtracted from the spectrum measured by the Cy-TEPC (Figure 5-4).

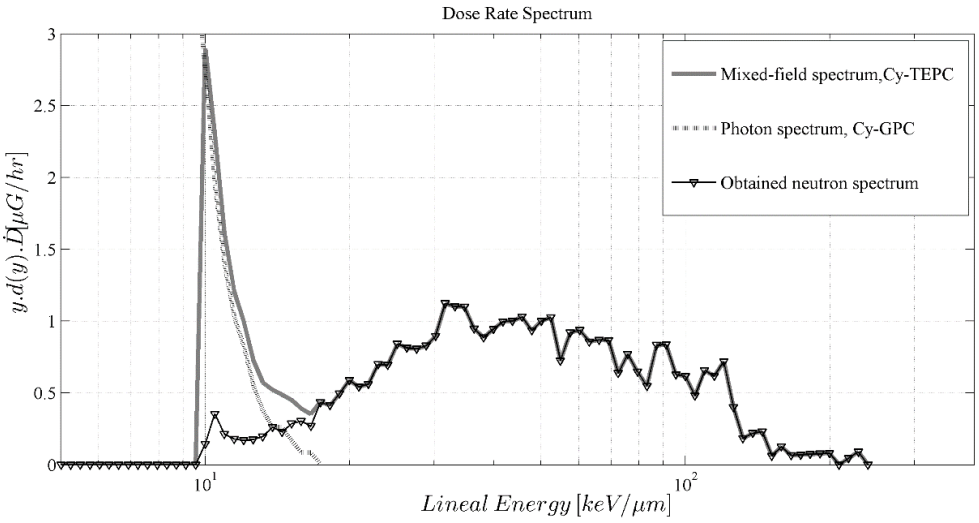

Figure 5-4 Neutron dose rate spectrum obtained by subtraction of gamma dose rate spectrum from the mixed-field spectrum

The obtained neutron spectrum was then normalized and compared to the pure 2.5 MeV neutron dose rate spectrum measured with the Cy-TEPC in section 4.5.2. As it can be seen in Figure 5-5, these two spectra fitted perfectly and confirmed the reliability of the twin-counters method in this radiation field.

It is quite common in experimental microdosimetry, as an approximation, to consider the events with lineal energies below 10 keV/μm to be created by photons, and lineal energies above this value to be generated by neutron interactions. However, as it is shown in Figure 5-4, there are events between 10 and 20 keV/μm recorded by the Cy-GPC and thus are supposed to be created mainly by photons. Therefore, by doing the subtraction of the Cy-

GPC spectrum from the Cy-TEPC measured spectrum a more accurate neutron dose rate spectrum can be obtained and compared to the conventional findings (Figure 5-5).

The results of the neutron dose rate calculation are summarized in Table 5-1.

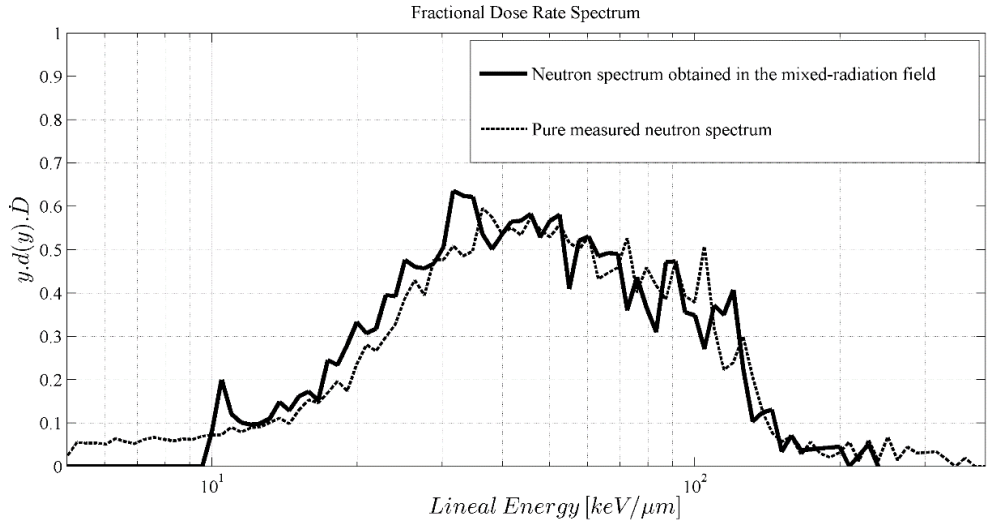

Figure 5-5 Comparison of normalized neutron spectrum in the mixed radiation field of 2.5 MeV neutrons and Cs-137 gamma rays with the measured spectrum of pure 2.5 MeV neutrons.

In radiation biology, the quantity of interest is absorbed dose or dose rate, whereas in radiation protection, the dose equivalent is considered as the reference quantity. Therefore, in order to investigate the contribution of the overlap area in the neutron and gamma spectra from the radiation protection point of view, the dose equivalent rate spectrum of this radiation field was also calculated and plotted in Figure 5-6.

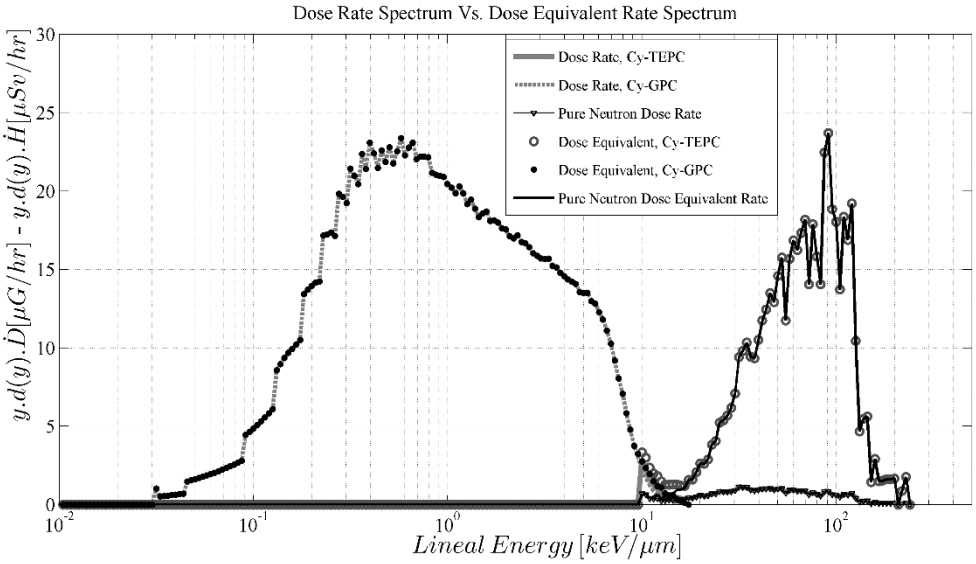

Figure 5-6 Comparison of dose rate and dose equivalent rate spectra for the mixed-field of 2.5 MeV neutrons and Cs-137 gamma rays.

The dose equivalent rate plot was obtained by multiplying the quality factor to the dose rate spectrum. According to the ICRP report 60 recommendations, the following equation shows the relationship between the quality factor and the unrestricted Linear Energy Transfer (LET or L) (ICRP60, 1991):

$$Q(L) = \begin{cases} 1\,, & L < 10\ \dfrac{keV}{\mu m} \\ 0.32L - 2.2, & 10\ \dfrac{keV}{\mu m} < L < 100\ \dfrac{keV}{\mu m} \\ \dfrac{300}{\sqrt{L}}, & L > 100\ \dfrac{keV}{\mu m} \end{cases} \qquad (5-1)$$

Although the LET and lineal energy (y) are not generally the same quantities, in this small micron-size site they can be assumed equal. Therefore, at each lineal energy, the

corresponding Q value was multiplied by the dose rate and the dose equivalent rate spectrum was found. The dose equivalent values for each radiation component were also obtained and are shown in Table 5-1.

Table 5-1 Neutron and photon dose rates and dose equivalent rates of the mixed-field of 2.5 MeV Neutrons and Cs-137 gamma rays.

Event-size Spectrum	Dose Rate (μGy/hr)	Dose Equivalent Rate (μSv/hr)
Photon, Cy-GPC	1.638e+03	1.644e+03
Mixed-field, Cy-TEPC (y ≥10 keV/μm)	48.08	626.82
Photon, Cy-GPC (y≥ 10keV/μm)	9.75	16.69
Neutron	38.32	610.13

As it can be seen in Figure 5-6 and the dose equivalent rate data in Table 5-1, the effect of neutrons from the radiation protection point of view is remarkably higher than their contribution in the dose rate spectrum.

On the other hand, according to the results in Table 5-1, the neutron dose rate value in this mixed radiation field is ~38.32 μGy/hr, whereas, if the conventional 'threshold' approach was applied, the neutron dose rate value would be 48.08 μGy/hr, which is due to the events

with the sizes above 10 keV/μm. The difference between these two values is ~ 9.75 μGy/hr, which denotes a 20% relative difference. However, applying the same threshold causes a relative difference of ~2.7% in the neutron equivalent dose rate, which may not be of great consequence in radiation protection dosimetry, but in radiation fields used for radiobiology or radiation therapy this cannot be assumed. Therefore, the twin-counter method improved the accuracy in procuring the neutron event-size spectrum and finding the dose rate in this mixed-radiation field. Part of these results has been published in Radiation Protection Dosimetry journal ((Forouzan & Waker, 2018).

In addition to the experimental measurements, this radiation field was also simulated in PHITS to benchmark the code versus the measurement results. The details and results are presented in the next section.

5.1.2 PHITS simulation

Cy-TEPC irradiated by 2.5 MeV neutrons was simulated to compare the results with the neutron even-size spectrum, which were obtained in the first set of measurements described in section 5.1.1 by subtracting the gamma even-size spectrum from the mixed-field spectrum. The event-size spectrum measured by the Cy-TEPC in the pure neutron radiation field was also compared to these spectra and the result of this comparison is shown in Figure 5-7 and Figure 5-8.

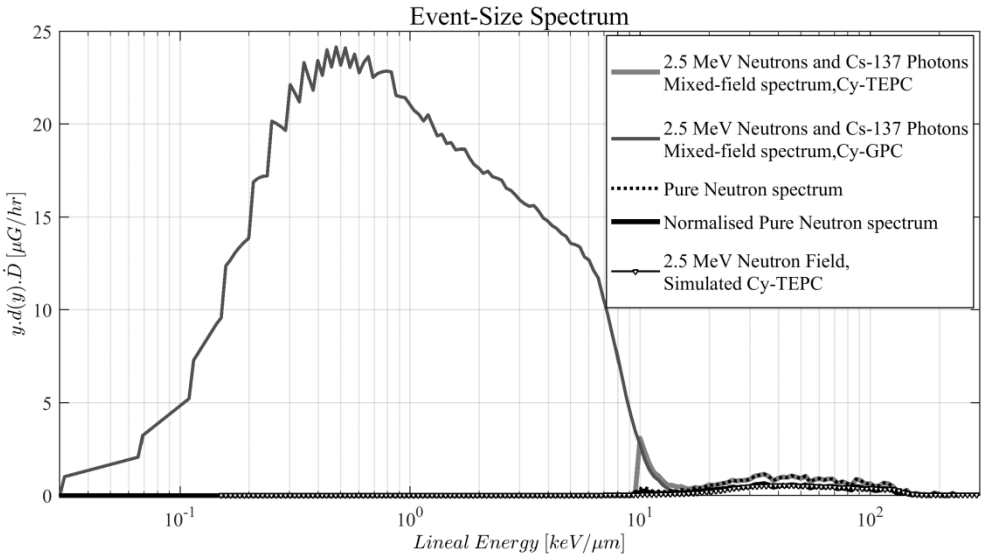

Figure 5-7 Comparison of 2.5 MeV neutrons event-size spectra obtained in measurement to the simulation results.

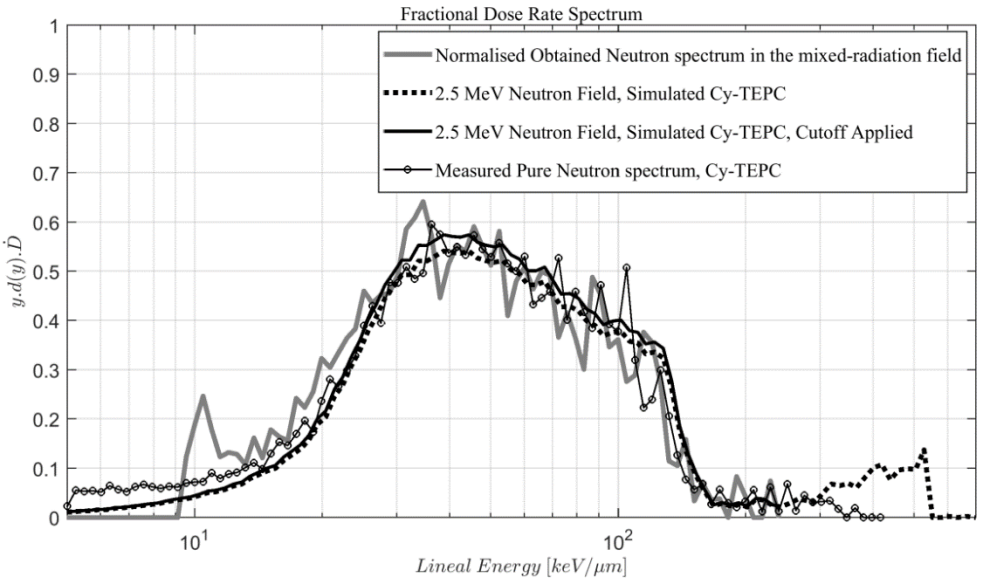

Figure 5-8 Comparison of event-size spectra obtained from the simulated Cy-TEPC in the 2.5 MeV neutron radiation field with measurements

As it can be seen if Figure 5-8, there is a good agreement between the 2.5 MeV neutrons event-size spectrum obtained from PHITS simulation and the measured spectra, especially in terms of the proton peak and the proton edge at ~40 and ~130 keV/ μm respectively. The simulation data points above 250 keV/μm of lineal energy cannot be verified with the experimental results, due to the Cy-TEPC applied gas gain, which defines the upper lineal energy limit. However, these events affect the normalization of the simulation spectrum, and because the experimental and simulation spectra were normalized to unity, they should have the same start and end points. Therefore, a cutoff point was applied to the simulation spectrum at 250 keV/μm to make the comparison of the normalized spectra more accurate. In the lineal energy range of 10 to around 20 keV/μm, where the gamma and neutron spectra overlap, the simulation results slightly underestimate the event-size values compared to the two experimental spectra. On the other hand, the proton edge of the simulated spectrum is a little bit higher than the experimental spectra. These differences are not significant enough to be compared quantitatively and lie within the estimated calibration uncertainty.

In addition to the Cy-TEPC and the Cy-GPC, the 5" spherical TEPC was also modeled in PHITS to compare the simulation results of the 2.5 MeV neutron field with the measured data. The results of this comparison are shown in Figure 5-9.

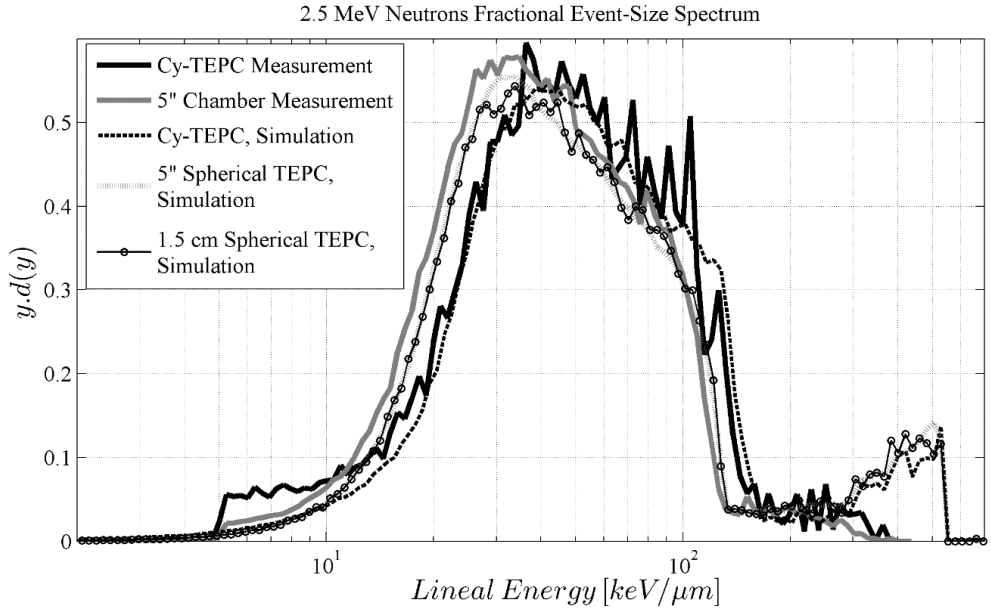

Figure 5-9 Comparison of 2.5 neutron event-size spectra obtained from TEPCs with different geometries.

According to Figure 5-9, the overall shape of the 2.5 MeV neutrons event-size spectra obtained from all the TEPCs either by measurements or simulations are very similar. However, the Cy-TEPCs event-size spectra show a shift toward higher lineal energies compared to the spherical TEPC spectrum. Although, the size of the cavities in the Cy-TEPC and the 5" TEPC are different, both of them represent the same tissue site size (by filling with different gas pressures). However, to eliminate the size difference and investigate only the geometry effect of the counters, another spherical TEPC with the diameter of 1.5 cm and the same gas pressure as the Cy-TEPC was simulated in PHITS. As it can be seen in Figure 5-9, the event-size spectrum of this smaller TEPC matches to the 5" TEPC spectra and has a proton edge at ~120 keV/μm rather than the ~150 keV/μm, which is the proton edge position of the Cy-TEPCs results. Therefore, it seems that the dosimetry results depend not

only on the mean chord length of the counter, but also on the geometry of cavity. This issue was investigated in more depth and an explanation is represented in section 6.2.

Due to the applied gas gain to the TEPCs, the data for the events above 300 keV/μm is not available to be compared to the simulation results.

Summary

In this chapter the use of the custom-made cylindrical graphite proportional counter (Cy-GPC) along with the cylindrical tissue equivalent proportional counter (Cy-TEPC) was studied for neutron–gamma mixed-field dosimetry in the radiation field produced by a P385 Neutron Generator (Thermo Fisher Scientific) together with a Cs-137 gamma source. The gamma dose-rate spectrum was measured with the Cy-GPC, while the neutron dose-rate spectrum was obtained by subtracting the Cy-GPC measured spectrum from the Cy-TEPC spectrum, which measured the events created by both neutrons and photons. The obtained neutron dose-rate spectrum was in very good agreement with the dose-rate spectrum measured with the Cy-TEPC in the pure neutron radiation field of the P385 Neutron Generator.

The results of the measurements also showed that if a simple lineal energy threshold was used to separate the neutron induced events, the photon contribution to event sizes above 10 keV/μm can be significant and make an inaccuracy in the neutron and photon dose discrimination. As it was shown in the comparison of the dose-equivalent rates data in this chapter, this inaccuracy may not be of great consequence in radiation protection dosimetry, but in radiation fields used for radiobiology or therapy this cannot be assumed.

Furthermore, the Cy-TEPC was simulated in PHITS and the event-size spectrum was compared to the normalized neutron event-size spectrum obtained in the measurement of the same neutron-gamma mixed radiation field and also to the spectrum measured in the pure 2.5 MeV neutron radiation field. In addition to the cylindrical counter, the 5" and the 1.5 cm spherical TEPCs were also simulated and the event-size spectra were compared to the measured spectra. The overall shape of the results were very similar to each other, except that there was a shift towards higher lineal energies in the spectra obtained by the cylindrical counters compared to the spherical counters results. This issue has been studied in the chapter 6 in more details.

Therefore, based on the results of the measurements and simulations conducted in the mixed-radiation field, it was confirmed that the concept of combining two counters is practical for building a single instrument for gamma and neutron dose measurements, which is the ultimate purpose of this research.

Chapter 6

Computational Simulations and Discussion of 14.8 MeV Neutron Irradiation

6.1 PHITS simulation and comparison to the measured data

The other monoenergetic neutron measurement, which was simulated in the PHITS code was the 14.8 MeV neutron radiation field. The measurement was carried out at the Physikalisch-Technische Bundesanstalt (PTB), Braunschweig, as a part of an international project for inter-comparison of TEPC systems from seven European groups used for radiation protection in late 1980s (Alberts, 1989)

The counter was modelled according to the specifications of the Far West LET-SW5, 5" single wire counter, which was used in the measurement. This counter was a sphere with an inside diameter of 12.55 cm and a wall thickness of 0.213 cm made out of A-150 Shonka plastic. It was filled with propane based tissue equivalent gas with the density of $1.59 \times 10^{-5}\ \frac{g}{cm^3}$ (pressure of 5.6 torr) to simulate a 2μm site-size in tissue. Similar to the case of 2.5 MeV neutrons simulation, a square-shaped neutron source with the energy of 14.8 MeV was defined in the PHITS code. However, the dimensions of the planar source in this case was 13 cm × 13 cm to make sure that it covered the entire cross section of the 5" spherical counter with a uniform neutron beam.

In addition to the spherical TEPC, the Cy-TEPC and the Cy-GPC were also modelled to make a comparison and have an idea of their performance in this neutron field.

The input files of these simulations are shown in Appendix D and the results are shown in Figure 6-1.

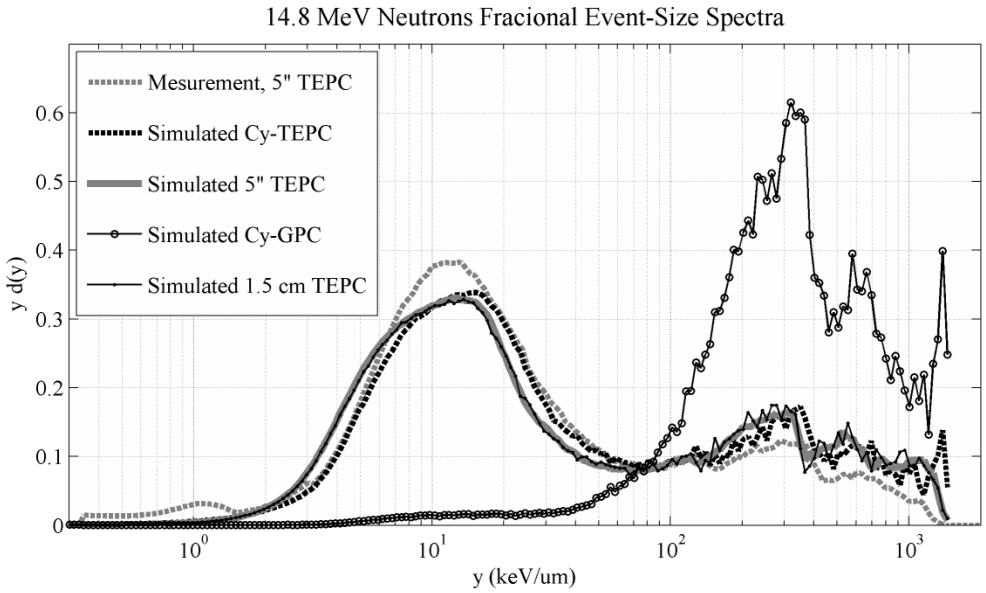

Figure 6-1 Comparison of measurement and simulation results for 14.8 MeV neutrons fractional event-size spectra

This figure shows a good agreement between the simulated TEPCs output and the 5" TEPC measurement results in terms of the overall shape, the position of the recoil proton peak (at ~12 keV/μm) and also the proton edge (at ~140 keV/μm) and the heavier ions edges (created by alpha particles and carbon recoils). However, the proton peak of the measured event-size spectrum with the 5" TEPC is larger than the simulated TEPC proton peaks. Similar to the case studied in chapter 5, the reason of this probably is that in the measurement, the energetic neutrons have been interacted with the walls and equipment of the laboratory through elastic scattering and have been created more low-LET events in the TEPC compared to the simulations, where the details of the laboratory contents were not included in the code input.

In the same way of the 2.5 MeV neutrons dosimetry case, a spherical TEPC with the diameter of 1.5 cm was also simulated for the 14.8 MeV neutrons irradiation and similarly,

the shift between the spectra of the simulated Cy-TEPC and the simulated spherical TEPCs can be seen in Figure 6-1. However in this case, the proton edge position and the overall shape of the 5" TEPC measured spectrum fits better to the simulated Cy-TEPC data rather than the simulated spherical TEPC. This is probably happened due to inaccuracy in the calibration factor of the 5" spherical TEPC. However, since the measurement was conducted several years ago by another group, it was not possible to be repeated and checked for the correctness of the calibration process.

For the event sizes larger than 100 keV/μm, it seems that PHITS simulation overestimates the dose rate contribution of heavier ions, such as alpha particles and carbon recoils. This is in agreement with the results reported by Ali et.al (Ali et al., 2013).

The simulated Cy-GPC on the other hand, shows almost no response to proton recoils, but records heavier charged particles with lineal energies above 40 keV/μm. The Cy-GPC spectrum shows that the entire dose recorded by this counter is deposited through carbon recoils rather than recoil protons. Therefore, it still works well for a good measurement of the gamma component of a mixed field at higher energies.

6.2 Discussion on geometry effect of the counter on the event-size spectrum

As it was observed in the measurements and simulation results of 2.5 MeV neutrons dosimetry, and the simulation results of the 14.8 MeV neutrons, the spectra obtained by the Cy-TEPC were shifted towards higher lineal energies compared to the spherical TEPC data. Although both the Cy-TEPC and the 5" spherical TEPC simulate the same tissue site size (2μm), their actual sizes are different. Therefore, in order to eliminate the difference between the counters size and investigate only the effect of the counters geometry on the dose

spectrum, another spherical TEPC with the diameter of 1.5 cm, which was the same as the Cy-TEPC diameter, was simulated in PHITS. As it was shown in Figure 5-9 and Figure 6-1, the event-size spectra obtained from the 1.5 cm spherical TEPCs matched to the 5" spherical TEPCs spectra. The same shift between the Cy-TEPC and the 5" spherical TEPC spectra was also observed between the Cy-TEPC and the 1.5 cm spherical TEPCs spectra. This shift was quantified in each case by estimating the difference between the proton peak positions of the two spectra obtained by the cylindrical and spherical TEPCs and divided that value by the proton peak position of the spherical counter. For the 2.5 MeV neutrons the shift was around 15%, and in the case of 14.8 MeV neutrons it was ~20% larger than the spherical TEPC proton edge position. These numbers are larger than the typical uncertainty in the proton edge position that might happen due to changes in gas pressure (2%) and/or calibration errors (5%) (Lindborg, 1975). Therefore, it seems that it is not enough that the two counters have the same mean chord length for measuring identical dose spectra. But rather the geometry of the counter is also an effective factor on the pattern of interactions occur inside the counter's cavity. Although, right cylinder, whose diameter and height have the same length, is the most similar shape to sphere, the chord length distribution in these two volumes are not the same. The chord length distribution equation in a sphere with diameter d is $f(l) = \frac{2l}{d^2}, 0 < l \leq d$, and it has a linear shape with the slope of $\frac{1}{d^2}$ (Birkhoff, Turner, Anderson, Feola, & Hamm, 1970). However, the analytical formula for the chord length distribution in a cylinder is so complicated (Birkhoff et al., 1970) and cannot be plotted easily. This distribution has been derived by numerical methods in other works (Kellerer, 1971a). Birkhoff and Turner used Monte Carlo technique to find the track length distribution in cavities with different

geometries, included a right cylinder with the height and diameter of 2 cm (Birkhoff et al., 1970). This was the closest dimensions to the Cy-TEPC cavity in this research (d=h=1.5 cm). The track length distribution plot of this cylinder was borrowed from the paper and used for a better visual comparison with the chord length distribution in the two spheres with 2 cm and 12.5 cm diameters (Figure 6-2).

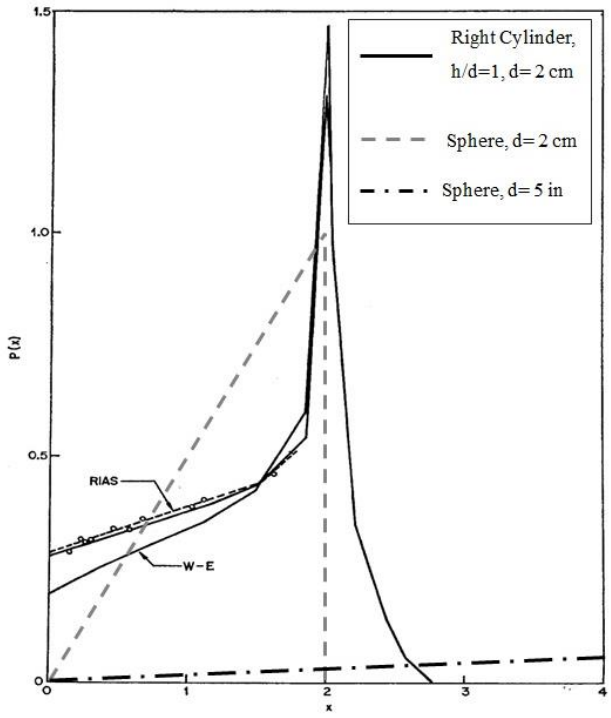

Figure 6-2 Comparison of chord length distribution in right cylinder and spheres. The distribution in cylinder has been taken from (Birkhoff et al., 1970)

According to the work of Birkhoff and Turner, the chord-length distribution can be scaled from one cylinder to another one with the same elongation (height/radius) ratio. The reason is that the probability distribution equation depends only on this ratio, not the absolute dimensions of the cylinder. Therefore, Figure 6-2 shows a typical comparison between the chord-length distributions in a right cylinder and two spheres.

As it can be seen in this figure, the longest chord in a sphere is the diameter. Thus those energetic protons, whose range is equal to the counter's diameter, will deposit the largest amount of lineal energy in the cavity. This value corresponds to the proton edge lineal energy in the event-size spectrum obtained from a spherical TEPC. In a cylinder however, there are chords longer than the cylinder's diameter. These chords can be anywhere in the area shown in Figure 6-3 with dashed lines. If protons have longer ranges equal to these longer paths, they will create events with larger lineal energies compared to the events created by protons traversed the cylinder diameter. Therefore, the proton edge of the cylindrical counter's event-size spectrum occurs at a higher lineal energy in comparison to the spherical counter with the same diameter. This can describe the reason of the consistent difference between the event-size spectra positions in the cylindrical and spherical counters data. Many protons do not have enough energy to traverse these longer chords in the cylinder, and most of them go along the diameter. This is the reason of the sharp peak of the track length distribution around the cylinders diameter in Figure 6-2.

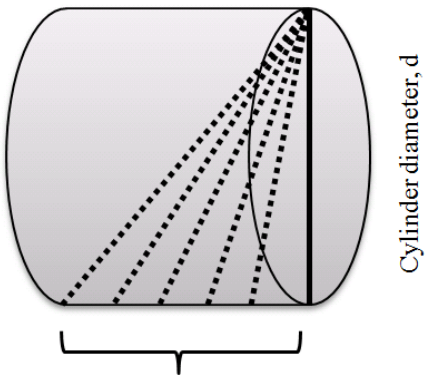

Figure 6-3 Chords longer than the diameter in a right cylinder

Summary

The 5” spherical TEPC which had been used in another study for measuring the event-size spectrum of 14.8 MeV neutrons was modelled in the PHITS code and the obtained results showed general similarity to the measured data, except that there was a shift between the two spectra, probably due to the inaccuracy in the TEPC calibration factor during the measurement. Moreover, similar to the results obtained in the mixed-radiation field of 2.5 MeV neutrons and 0.662 MeV gamma rays, more low-LET events were observed in the experimental results compared to the simulation event-size spectra. The details of the laboratory contents should be added to the simulation code to find more accurate results.

Geometrical shape of the counters was also another parameter that was affecting the results. Similar to what was previously observed in chapter 5, the event-size spectra obtained by the cylindrical TEPC was shifted towards higher lineal energies compared to the spherical TEPC data. A discussion on the cord length distributions in the cylindrical and spherical cavities was provided to study the reason of this shift more deeply. It was shown that there are some chords longer than the diameter of the right cylinders and if the protons have the same range as these paths, they will impart more lineal energies than those which have a range equal to the diameter of the counter cavity. These larger energy impartments result in higher-LET events and explain the upward shift in the spectra obtained by the cylindrical TEPCs compared to the spherical counters.

Chapter 7

^{241}Am-Be broad spectrum neutron source

The Americium–Beryllium (^{241}Am-Be) neutron source is recognized as the most widely used and frequently employed reference neutron source. Therefore, ^{241}Am-Be sources have become the standard for assessing detector performance. As it plays a crucial role in neutron metrology, it is essential that detectors will be evaluated using this source. It generates neutrons in the energy range of 0-11 MeV, with the average neutron energy of ~4.2 MeV. Figure 7-1 shows the simulated neutron energy spectrum for this source presented in the International Organization for Standardization ISO-8529/1 (Standardization, 2001) and the actual figure has been taken from another paper (Mazrou, Idiri, Sidahmed, & Allab, 2010). The broad energy range of neutrons makes ^{241}Am-Be source an appealing choice to study the response of the Cy-TEPC and the Cy-GPC to non-monoenergetic fast neutrons. The measurements and simulations conducted in this radiation field is discussed in this chapter.

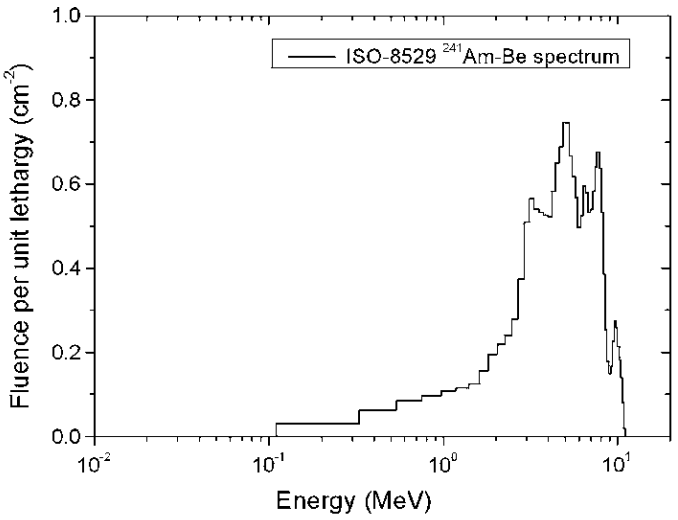

Figure 7-1 Simulated ^{241}Am-Be neutron energy spectrum (Mazrou et al., 2010)

7.1 Measurements

The radiation protection laboratory of Ontario Tech University is equipped with a multisource ^{241}Am-Be neutron irradiation facility, which can accommodate up to 9 ^{241}Am-Be capsules protected in 179 cm long aluminum tubes. At the time of these measurements only three ^{241}Am-Be sources were installed in the first row of three tubes. The bottom of the tubes is immersed in water to moderate the neutrons emitted from the sources and provide shielding to meet radiation safety regulations. During the measurements, the sources are elevated in the tubes using thin cables connected to the source capsules. The whole arrangement is protected by a cage to limit access as shown in Figure 7-2.

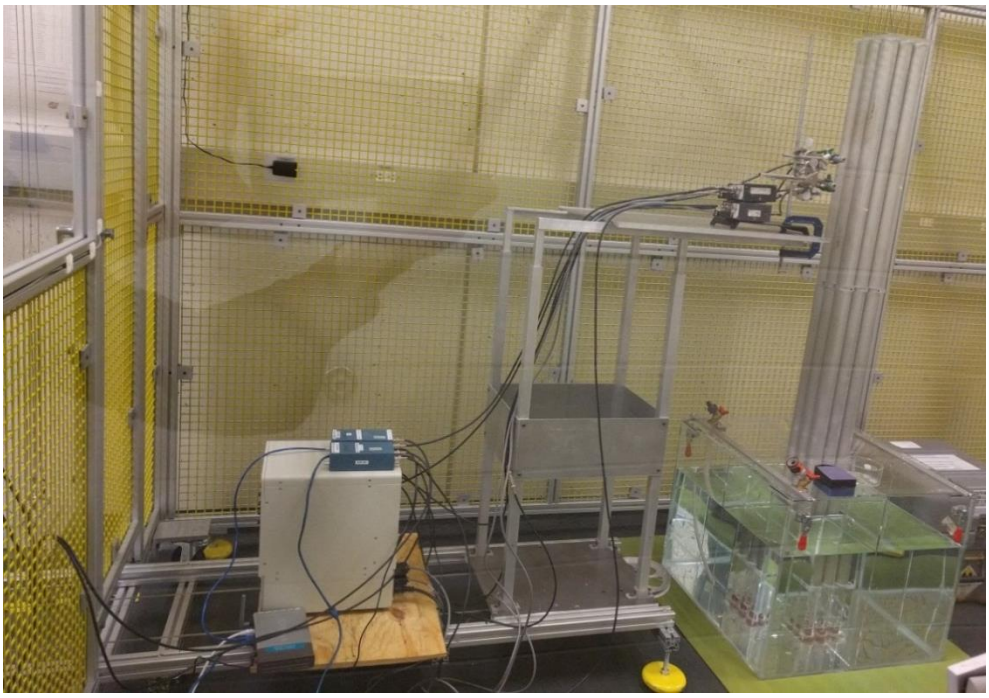

Figure 7-2 The Am-Be facility at Ontario Tech University.

The two counters, the Cy-TEPC and the Cy-GPC, were placed at the closest proximity to the sources (~3 cm) to ensure that the neutron field count-rate was maximized (Figure 7-3).

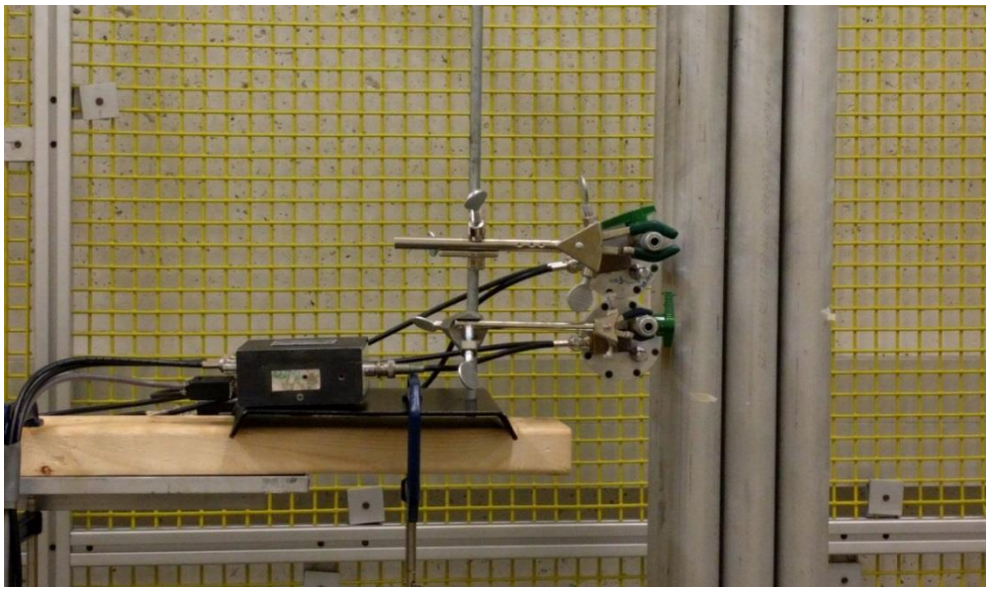

Figure 7-3 Position of the Cy-TEPC and the Cy-GPC in front of the Am-Be neutron source.

The frequency distributions of the energy deposition events created by radiation interactions in the counters were generated out of the measurements with the pulse-height signal processing system. These distributions then converted to the dose rate spectra, presented in the equal logarithmic distribution format, following the steps explained in section 4.2.3. Figure 7-4 shows the ^{241}Am-Be dose rate spectrum, measured by the Cy-TEPC and the Cy-GPC.

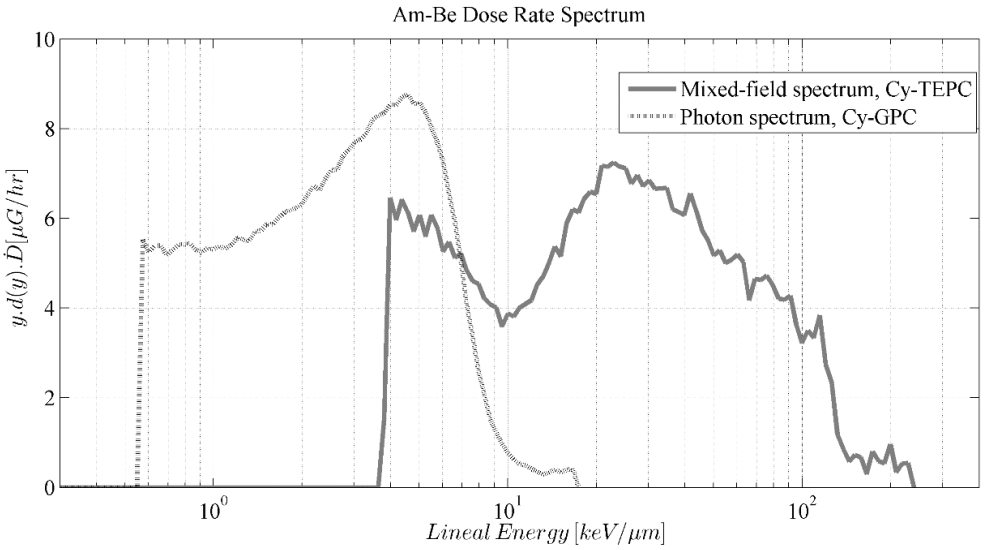

Figure 7-4 ^{241}Am-Be dose rate spectrum measured with the Cy-TEPC and the Cy-GPC

It is apparent from Figure 7-4 that the Cy-GPC, which is mainly used for measuring the events created by photons, recorded some events with lineal energies higher than 10 keV/μm. It is important to identify if all of these events are photon induced or some of them are neutron induced. The latter means that the Graphite counter is not completely insensitive to neutrons. To investigate this issue, the Cy-GPC measured spectrum in the ^{241}Am-Be radiation field has been compared against another measurement made with the same counter in an X-Ray beam of mean energy 65 keV. This energy is very close to the energy of the dominant photons emitted by the ^{241}Am-Be source (60 keV) (Figure 7-5).

In order to make this comparison feasible, the X-Ray dose-rate spectrum was scaled down, to match the Cy-GPC measured spectrum in the ^{241}Am-Be radiation field.

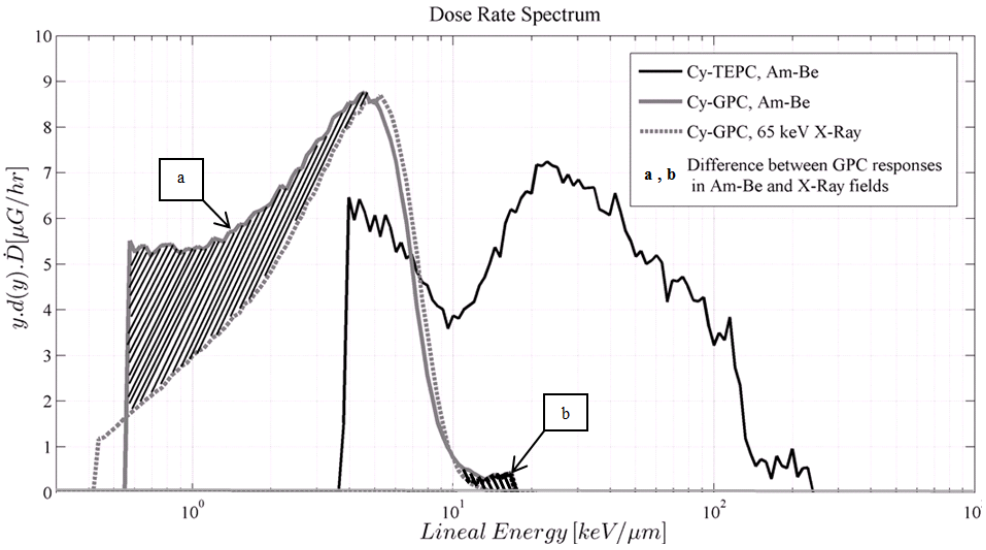

Figure 7-5 Comparison of the Cy-GPC responses in the 65 keV X-Ray and 241Am-Be radiation fields and the difference between the dose rate spectra for the events a) between 0.6 and 5keV/µm and b) between 10 and 20 keV/µm.

Overlaying the data reveals that the Cy-GPC measured spectra in the ^{241}Am-Be and 65 keV X-Ray radiation fields do not match in the area of the events smaller than 5 keV/µm. There is a difference of ~ 79 µG/hr between the dose-rate of the two spectra in this area (area a in Figure 7-5), which leads to an error of ~26% in the photon dose rate measurements. This discrepancy is possibly due to electrical noise or some pulse pile-up in the data acquisition system when measuring the ^{241}Am-Be dose rate.

When setting up a radiation detection system, the observed performance may be worse than expected due to extrinsic noise sources from other devices, often through ground connections. Interference always involves a source, coupling medium, and receiver, and problems depend on the details of a particular setup and parasitic circuit elements. Grounding issues can cause noise pickup and ground loops, which can be eliminated by ensuring that all

components are internally grounded to a single common point for the entire system. Common mode rejection is sometimes helpful in reducing the effects of noise pickup on interconnecting cables. The concept of "ground" includes three distinct and important notions: a common connection to earth ground for safety, the return path for power supply current, and a reference for signals. To minimize ground noise, these functions should be separated as much as possible, and a "star" ground approach can be helpful (Knoll, 2010). Knoll also mentions the use of common mode rejection to reduce noise pickup on interconnecting cables and the potential for high-frequency noise pickup from nearby equipment, such as computers (Knoll, 2010). However, access to the laboratories was prevented due to the COVID-19 pandemic and health protocols, which means that further efforts to investigate and overcome this issue will need to be made in future studies.

Another problem that should be addressed in future works, is the details of the experimental set-up and environment and their effect on the radiation field. For instance, as it can be seen in Figure 7-3, the mounting system for the counters is a significant amount of metal that is near the sensitive volume of the Cy-TEPC and the Cy-GPC. The metal mounting system can introduce scatter effects on photon and neutron spectra by interacting with incident particles, changing their energy and direction. The magnitude of these effects depends on factors like metal composition, thickness, particle energy, and setup geometry. However, for future works, consideration of these effects by modeling the experimental setup should be given.

In contrast, for the higher events the two photon spectra measured by the Cy-GPC are in good agreement, especially in terms of the electron peak and the electron edge positions at ~5 keV/μm and ~9 keV/μm respectively. For the events between 10 to 20 keV/μm, the dose rate

measured by the Cy-GPC in the ^{241}Am-Be radiation field was 3.12 μGy/hr more than what was measured in the 65 keV X-Ray field (area b in Figure 7-5). This analysis once again indicates that the Graphite counter has some sensitivity to neutrons in our region of interest, which covers the events from 10 to 20 keV/μm. It should be noted that for measuring the ^{241}Am-Be spectrum, the gas gain applied to the Cy-GPC was chosen such that it could record anywhere between the smallest photon events possible, to events with lineal energy of up to ~20 keV/μm. If a lower gas gain was applied to the counter, larger events created by neutrons could also be measured with the Cy-GPC. This highlights the fact that the neutron sensitivity of the Cy-GPC should be investigated carefully to understand how much uncertainty it brings to gamma-neutron mixed-field dosimetry. To this end, the event-size spectra, measured by the Cy-GPC, in both the 65 keV X-Ray and ^{241}Am-Be radiation fields were subtracted from the ^{241}Am-Be dose rate spectrum measured by the Cy-TEPC to find the effect of the neuron sensitivity of the Cy-GPC on the obtained neutron spectrum (Figure 7-6).

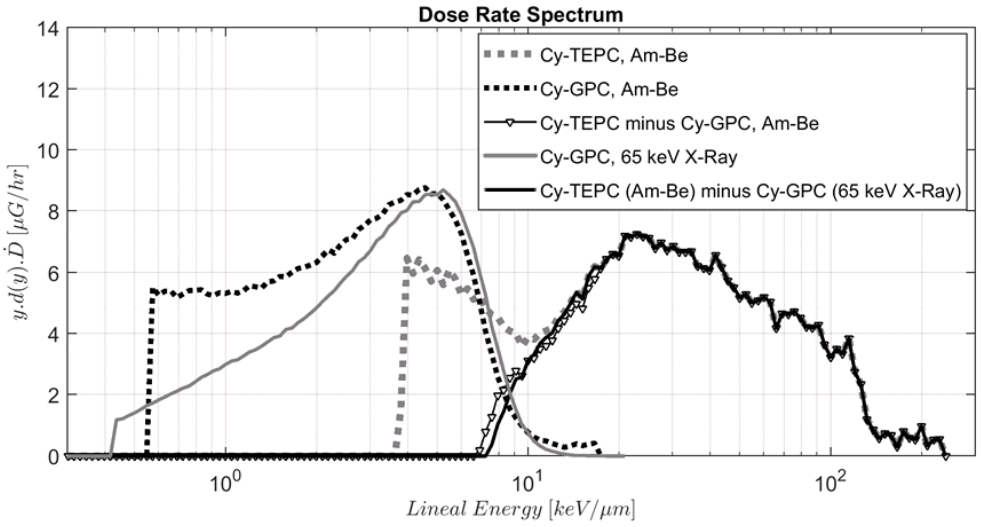

Figure 7-6 Subtraction of the dose rate spectra measured with the Cy-GPC in the 65 keV X-Ray and ^{241}Am-Be radiation fields from the ^{241}Am-Be dose rate spectrum measured with the Cy-TEPC.

The two obtained spectra in Figure 7-6 show insignificant difference in shape and a difference of only ~1μG/hr (~0.3% uncertainty) in the amount of the dose rate, which is negligible. Therefore, our analysis indicates that the sensitivity of the Cy-GPC to neutrons does not create a meaningful uncertainty in neutron- gamma dosimetry for the event-size range of 10 to 20 keV/μm, and thus makes it reasonable to assume that the dose rate spectrum obtained by subtracting the Cy-GPC from the Cy-TEPC measurements in the ^{241}Am-Be radiation field can be assumed to be the pure neutron dose rate spectrum. This spectrum was further studied in terms of radiation biology and radiation protection as follows.

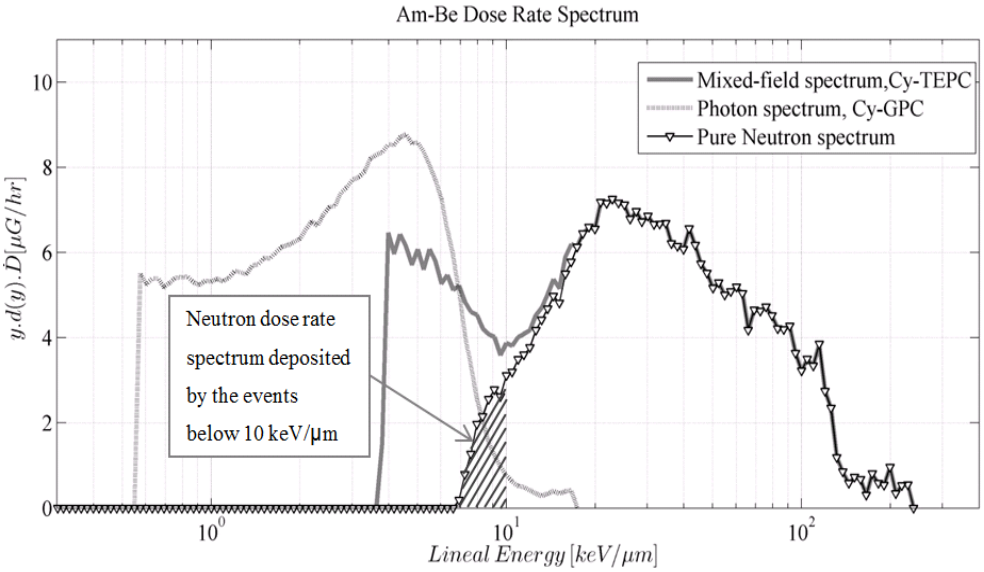

Figure 7-7 ^{241}Am- Be neutron dose rate spectrum, obtained by subtracting of the Cy-GPC measured spectrum from the Cy-TEPC measured data.

As it was mentioned before, in radiation biology, the quantity of interest is absorbed dose or dose rate. Therefore, in order to quantify the effect of the Cy-GPC neutron sensitivity and other uncertainties on neutron dosimetry form the radiation biology point of view, the dose rate spectrum has been studied.

As shown in Figure 7-7, the proton edge of the Cy-TEPC spectrum is at ~ 140 keV/μm, which is expected. However, for the lineal energies below 10 keV/μm the measured spectrum by the Cy-TEPC does not match the Cy-GPC spectrum. One contributing factor might be a malfunction in the measurement system at the time of conducting the measurements leading to a higher level of noise impacting the data below 10 keV/μm. On the other hand, we confirmed that the events smaller than 10 keV/μm were caused by neutrons too. This was done by checking the stopping power of 4-10 MeV neutrons in TE gas in the SRIM program

and ensuring that they can create events smaller than 10 keV/μm (J. F. Ziegler). Nevertheless, the pure neutron dose rate spectrum of the ^{241}Am-Be radiation field was obtained by subtracting the Cy_GPC photon spectrum from the mixed-field spectrum measured by the Cy-TEPC from the lineal energy of 7 keV/μm, at which the two spectra coincide with each other.

A part of the obtained pure neutron dose-rate spectrum is created by events smaller than 10 keV/μm (dashed area in Figure 7-7). These events are created either by high energy recoil protons, with lower LET or by lower energy protons that interact in the counter over a very short chord-length.

The dose rate deposited by these small events was calculated as ~17.4 μGy/hr. When this value was compared to the entire ^{241}Am-Be neutron dose rate, a contribution of ~5% was found for this part. However, if the value of 10 keV/μm is considered as the traditional threshold of the neutron-created events, the area below 10 keV/μm generates an uncertainty of 5% to the neutron dose rate spectrum.

To find the effect of the uncertainties in the Cy-TEPC and Cy-GPC measurements in term of radiation protection, the dose equivalent of the obtained neutron spectrum has been also calculated and plotted in Figure 7-8.

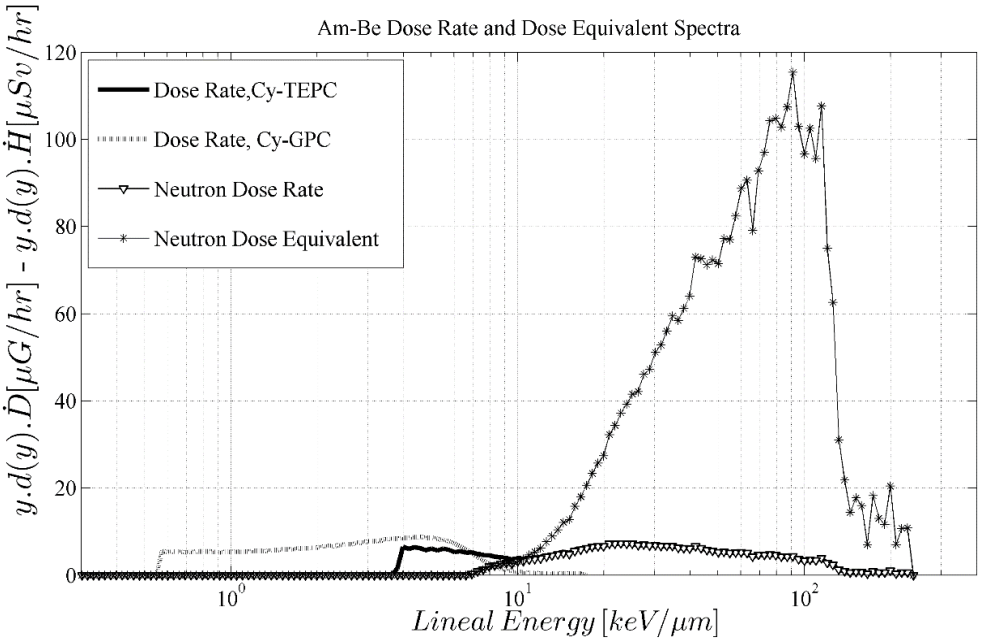

Figure 7-8 Comparison of ^{241}Am-Be neutron dose rate and neutron dose equivalent rate spectra

Figure 7-8 shows that in terms of radiation protection, neutrons with lineal energies larger than 10 keV/μm has significantly higher contribution than the photons and neutrons with smaller lineal energies. In order to have a better understanding of the neutrons and photons contribution in ^{241}Am-Be mixed-field dosimetry, the dose rate and the dose equivalent rate values of each component have been calculated and are presented in Table 7-1.

Table 7-1 ^{241}Am-Be neutron and photon dose rates and dose equivalent rates

Event-size Spectrum	Dose Rate (μGy/hr)	Dose Equivalent Rate (μSv/hr)
Mixed-field, Cy-TEPC ($y \geq 7$ keV/μm)	335.3	3390
Photon, Cy-GPC	381.9	386.4
Photon, Cy-GPC ($y \geq 7$ keV/μm)	21.1	25.6
Difference between Cy-GPC responses in the Am-Be and 65 keV X-Rays fields	3.12	7
Neutron	314.4	3365
Neutron ($y \leq 10$ keV/μm)	17.4	17.4

As shown in the table, the neutron dose rate, calculated by subtracting the photon dose rate, measured with the Cy-GPC, from the mixed-field dose rate, measured with the Cy-TEPC (for the events above 7keV/μm) is ~314.4 μGy/hr. The uncertainty in neutron dose rate measurement due to the neutron sensitivity of the Cy-GPC for the events between 10 and 20 keV/μm is estimated at ~ 3.12 μGy/hr, meaning that the relative error in neutron dose rate is

less than 1%. The dose equivalent values corresponding to the aforementioned quantities are 3365 and 7 μSv/hr respectively. This means that the neutron sensitivity of the Cy-GPC causes a slight relative error of ~2 $_x10^{-1}$ % in the neutron dose equivalent rate. Also, if the conventional threshold for the neutron induced events is considered, the events below 10 keV/μm create an uncertainty of ~ 0.5 % in the ^{241}Am-Be pure neutron dose equivalent rate (compared to the 5% error in the neutron dose rate). Therefore, as far as the radiation protection aspect is concerned, it seems reasonable to follow the conventional approach in radiation dosimetry and put a threshold at 10 keV/μm. The events below the threshold measured by the Cy-GPC then can be considered photon-induced and the events above 10 keV/μm recorded by the Cy-TEPC can be assumed neutron-induced. However, applying this threshold in radiation biology will lead to an uncertainty of about 5% in the dose rate calculation and neutron-gamma dose rate discrimination.

In retrospect, further investigation of the Cy-TEPC might have allowed us to identify a problem with either the counter or the acquisition system resulting in a mismatch between the Cy-TEPC and the Cy-GPC measurement data in the lower LET events (below 10 keV/μm). Upon successful troubleshooting, the measurement could have been repeated to confirm the reliability of the calculated ^{241}Am-Be neutron dose-rate spectrum.

In the next section, the neutron dose rate spectrum obtained from simulations is compared against the measurements for further study.

7.2 PHITS simulations

It is demonstrated in Figure 7-1 that the ^{241}Am-Be source emits neutrons in a broad range of energy from about 10^{-1} MeV to 11 MeV. This energy spectrum was defined as the source

energy in the PHITS code to simulate the measurements made by the Cy-TEPC and the Cy-GPC, and find the ^{241}Am-Be event-size spectrum. For the study presented in this section, the ^{241}Am-Be neutron energy distribution, which was shown in Figure 7-1, was implemented in the PHITS input file. The simulation results are compared to the normalized measured event-size spectra in Figure 7-9.

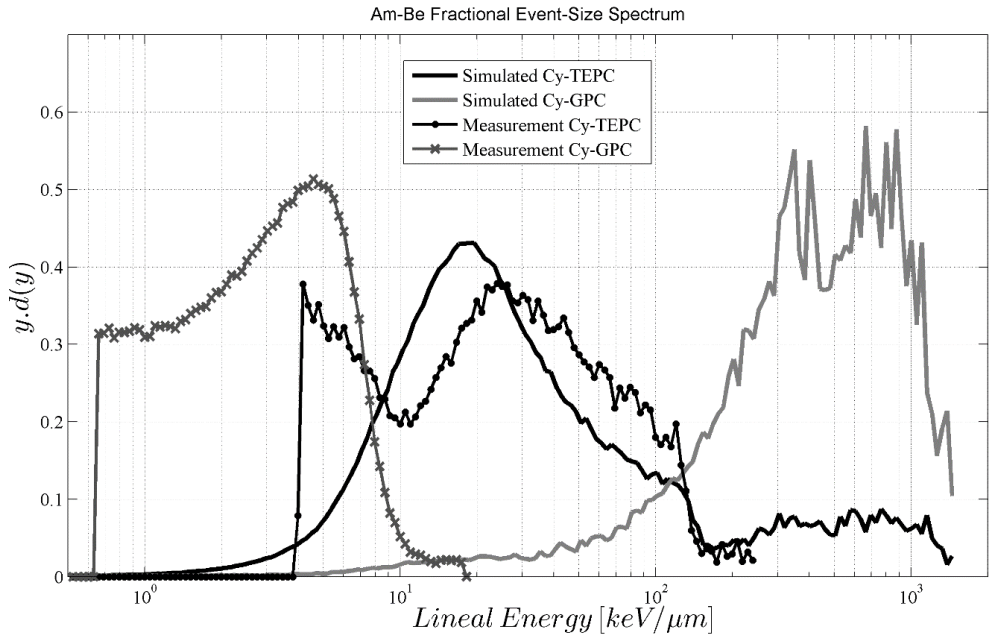

Figure 7-9 Comparison of measurement and simulation results for ^{241}Am-Be neutrons fractional event-size spectra.

As shown in Figure 7-9, the simulated Cy-GPC event-size spectrum shows low y d(y) values for the lineal energies below 100 keV/µm indicating that the Cy-GPC has a very low sensitivity to neutrons compared to the Cy-TEPC. The Cy-GPC experimental data are only available for lineal energies up to 20 keV/µm and the counter response to heavy particles such as Carbon ions and alpha particles cannot be evaluated against simulated data.

However, in the lineal energy range of 10 to 20 keV/µm, the Cy-GPC measured and simulated outputs are in good agreement.

For presenting a more accurate comparison, Figure 7-10 shows the simulated neutron spectrum overlaid on top of the measured pure neutron spectrum, obtained by subtracting the Cy-GPC spectrum from the Cy-TEPC spectrum measured in the ^{241}Am-Be radiation field.

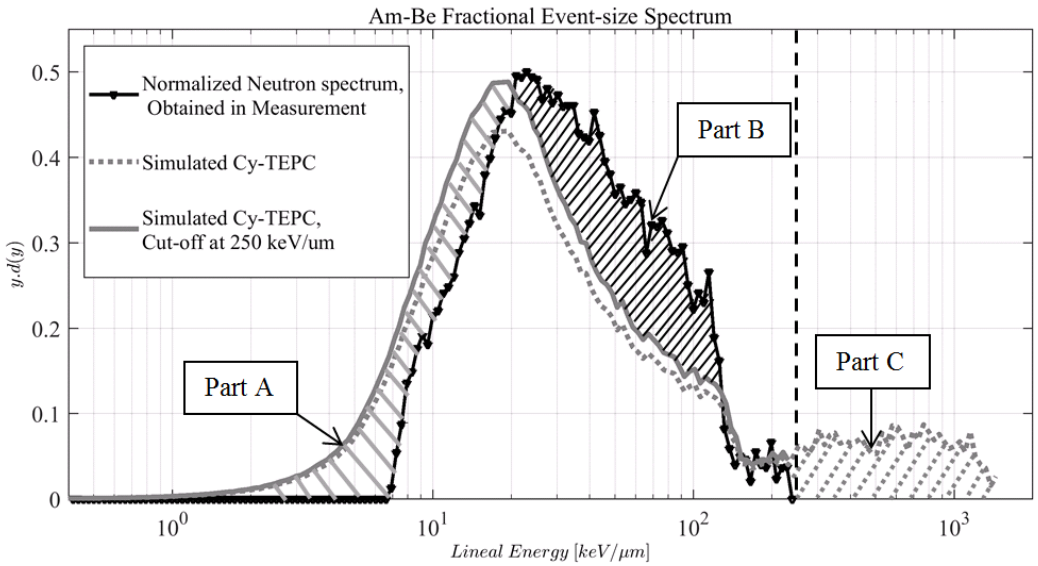

Figure 7-10 Comparison of measured pure neutron event-size spectrum and the simulation result with the cut-off at 250 keV/µm. Part A is the fraction of the two spectra below 20 keV/µm. Part B is the fraction of the two spectra between 20 and 140 keV/µm, and part C is the fraction of the simulation spectrum larger than 250 keV/µm

This figure indicates that for the measured and simulated neutron spectra, the proton edges are coincident at around 140 keV/µm. Moreover, the overall shape of the two spectra match reasonably well. Although, the pure neutron experimental spectrum shows a shoulder at the lineal energies of about 20 to 140 keV/µm (Part B in Figure 7-10) and its proton peak

position has occurred at a higher lineal energy compared to the Cy-TEPC simulation spectrum. It should be noted that the Cy-TEPC simulation spectra covers larger events created by heavier ions (Part C in Figure 7-10), whereas the measured pure neutron spectrum is terminated at ~ 250 keV/μm, due to the gas gain limitation of the Cy-TEPC. However, the two spectra have been normalized to unity and this is affecting their appearance in terms of shape and height. To fix this problem and make the comparison more accurate, the end point of the simulated event-size spectrum was set at 250 keV/μm. By applying this cut-off to the simulated spectrum, its proton peak almost matches the peak of the measured spectrum.

However, there is still a difference in other parts of the two spectra. The difference in the shoulder area (Part B in Figure 7-10) is likely due to the existence of more low-energy neutrons in the measurements compared to the simulation. These low energy neutrons are mainly created by interaction of the emitted energetic neutrons with the walls, floor and ceiling of the corridor as well as the contents of the corridor and other equipment of the laboratory, which were not simulated in the PHITS code in full detail. As a result, the fraction of more energetic neutrons, which create lower-LET events, are greater in the simulation compared to the measurement and this can explain the more simulated events below 20 keV/μm than those in the measurement (Part A).

And last but not least, Part C in Figure 7-10 demonstrates the fraction of the larger events mainly created by carbon recoils and heavier ions and it has a contribution of ~16% in the whole neutron spectrum. This part makes an important contribution to radiation protection, because of the high LET of the heavier ions and the damage they could cause to the tissue. However, due to the applied gas gain to the Cy-TEPC this part could not be measured

experimentally, and it would be important in future measurements to adjust the gas gains of the counters so that the higher end of the spectrum can be completely captured. Moreover, since the large events have a low probability of occurring, the measurements should be carried out for much longer exposure periods to collect enough data for processing.

Although demonstrating the general agreement between the simulated and measured data is a noteworthy contribution of this thesis, there is room for improvement in the simulation input file. One approach to enhance accuracy would involve incorporating the specific details of the measurement environment into the model. Another option is to utilize the actual measured neutron energy spectrum from the radiation field as the input energy spectrum for the PHITS code, rather than relying on the simulated Am-Be neutron energy spectrum. The first option was not feasible due to the extensive array of materials and complexities present in the radiation room. However, the second option was executed by measuring the neutron energy distribution at the Am-Be radiation field at Ontario Tech University using a Nested Neutron Spectrometer (NNS). Subsequently, the simulation was conducted once more, this time employing the measured input energy distribution. The obtained results were then compared to the measured and previously simulated event-size spectra, as illustrated in Figure 2.

This figure clearly demonstrates that the spectrum obtained from the latter simulation exhibits a significantly improved agreement with the measured event-size spectrum. This finding confirms the presence of a greater number of lower energy neutrons in the radiation facility, capable of generating events within the range of 20 to 150 keV/μm, in contrast to the simulation results that were derived from the simulated ^{241}Am-Be neutron energy

distribution. Consequently, if it is feasible to measure the actual neutron energy distribution within a radiation facility, it would provide a more precise input for the simulation, enhancing its accuracy and reliability.

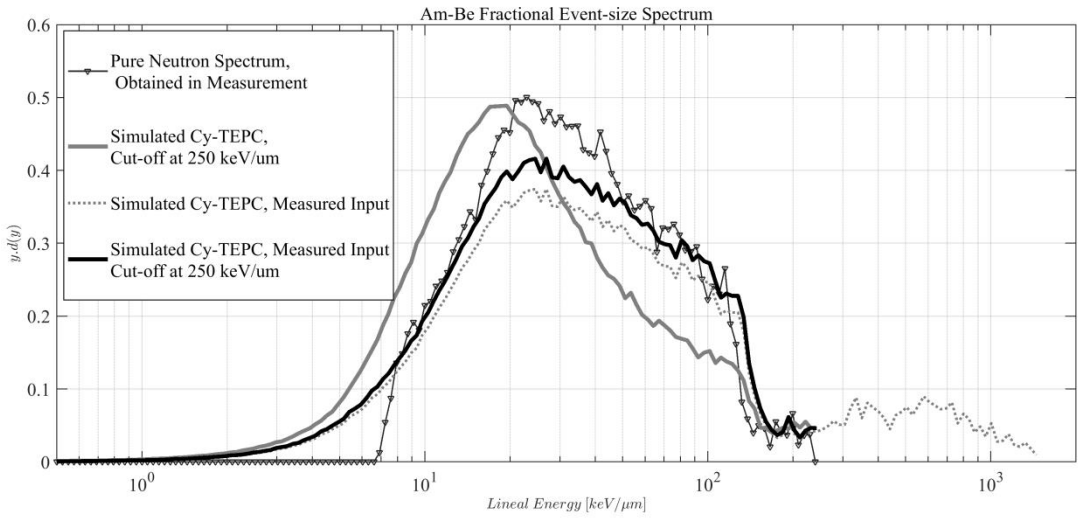

Figure 7-11 Comparison of the measured pure neutron event-size spectrum with two simulations utilizing simulated and measured input energy spectra.

Summary

The ^{241}Am-Be neutron dose rate spectrum was measured by subtracting the Cy-GPC measurement from the Cy-TEPC measured spectrum at the Ontario Tech university radiation protection laboratory. Since the ^{241}Am-Be source emits neutrons with a broad range of energies, the gas gain of the Cy-TEPC was selected so that it can detect as many neutron-induced events as possible. The Cy-GPC on the other hand, collected the lower-LET events, created mainly by photons. However, some unexpected data were observed in the very low end of the Cy-GPC measured spectrum in addition to a few events recorded above 10 keV/μm, which was conventionally considered as the threshold of neutron-created events. Therefore, this spectrum was compared to the dose rate spectrum of 65 keV X-Ray considering the similarity between the two in terms of photons energy. The comparison led us to the conclusion that the discrepancy in the very low end of the two photon dose rate spectra was due to some pulse pile-up and/or some electrical noise in the data acquisition system at the time of the measurement. On the other hand, our investigation showed that the Cy-GPC was slightly sensitive to neutrons. However, this sensitivity did not create any significant uncertainty in the pure neutron dose rate spectrum, obtained by subtracting the Cy-GPC measured spectrum from the Cy-TEPC measurement.

Furthermore, the measurement was simulated with the PHITS Monte Carlo code and the two obtained neutron spectra compared. Good agreement was observed between the two spectra in terms of the overall shape and the proton edge position. The only major difference between the two spectra was that more higher-LET events were recorded in the

measurement, probably due to the low energy neutrons created by scattering of the source neutrons from the walls, floor and equipment of the laboratory. The details of the laboratory and its contents were not simulated in PHITS. Consequently, more low-LET events were appeared in the simulation dose rate spectrum compared to the measurements due to more energetic neutrons considered in the code. For obtaining a more reliable comparison, these details should be added to future simulations or an experimental determination of the neutron energy spectrum in the laboratory used as input to the Monte-Carlo code. The gas gain of the Cy-TEPC should also be adjusted so that it records the very large events created by recoil carbons and heavier ions. These events may contribute significantly to the dose and dose equivalent and therefore it is important they are captured in the measurement process.

Chapter 8

High gamma component mixed radiation field at Kingston Reactor Materials Testing Laboratory (RMTL)

The Reactor Materials Testing Laboratory (RMTL) was built to study the damage mechanisms to nuclear power plants component materials from radiation exposure. It uses a 4 MV tandem accelerator to produce up to 8 MeV protons or 12 MeV alpha particles (Figure 8-1).

Figure 8-1 RMTL accelerator chamber (RMTL, 2015)

The high energy charged particles beam is then directed into one of the two target rooms, where the target material is installed and gets damaged in microscopic scale due to nuclear reactions (Figure 8-2).

Figure 8-2 Beam lines directing the charged particles beams to the target rooms (RMTL, 2015).

Figure 8-3 shows a diagram of the accelerator facility and the position of the target rooms, which are well shielded to protect the staff from radiation.

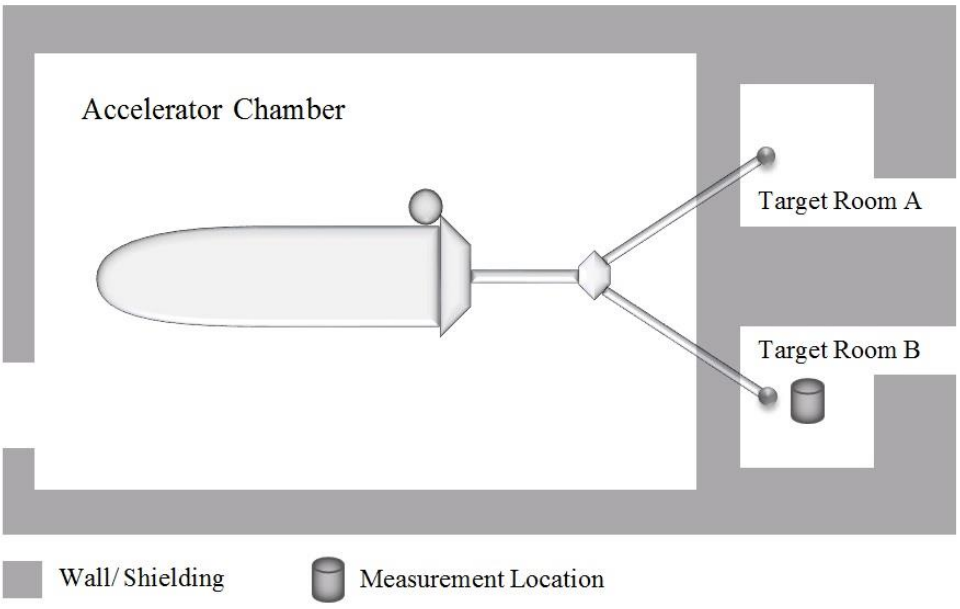

Figure 8-3 Schematic view of the RMTL accelerator facility and target rooms

In reactions between the accelerated particles and the target material atoms, several photons and neutrons with different amounts of energy are released. The energy distribution of these neutrons has been measured by Orchard and Waker for different target materials at room B (Figure 8-4) (G. Orchard, Feuerstake, McDonald, & Waker, 2021).

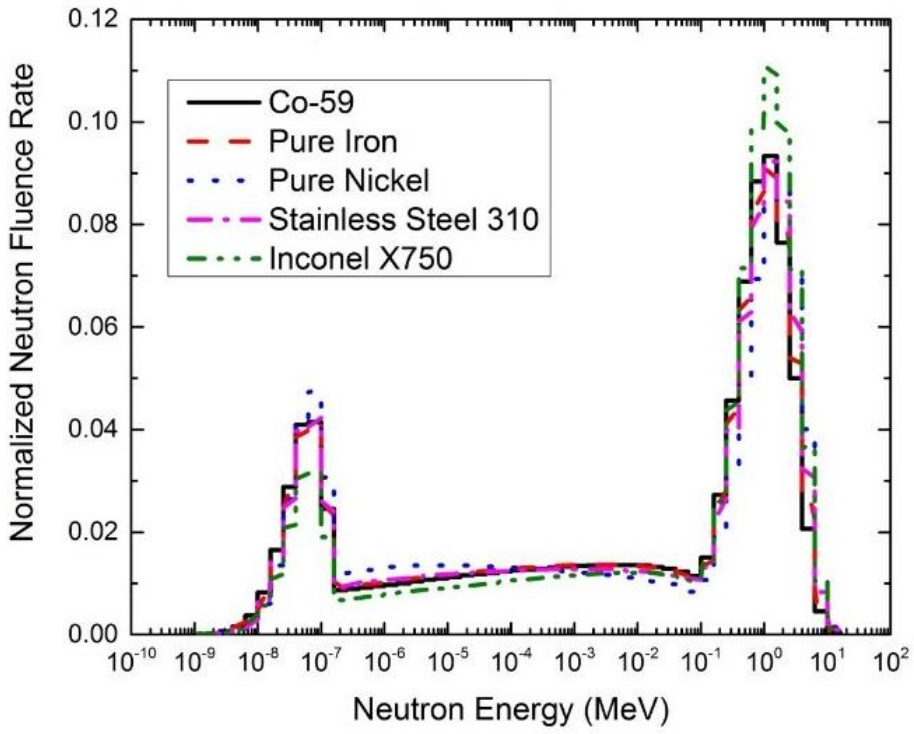

Figure 8-4 Neutron fluence rate spectra obtained for different targets in target room B, measured by Orchard and Waker (G. Orchard et al., 2021)

In this study, the event-size spectrum of the neutrons released in the interactions of protons with the ^{59}Co target in target room B was measured with the Cy-TEPC and the Cy-GPC. These measurements were then simulated by the PHITS code and the results were compared to the measured data to investigate the functionality of the twin-counter method in the high gamma component mixed-radiation field.

8.1 Experimental measurements

For conducting the measurements in this radiation field, the two counters were stacked vertically, in line with the accelerator beam and 57 cm away from the target (Figure 8-5). The measured data was then converted into dose rate spectra and plotted in Figure 8-6 for comparison.

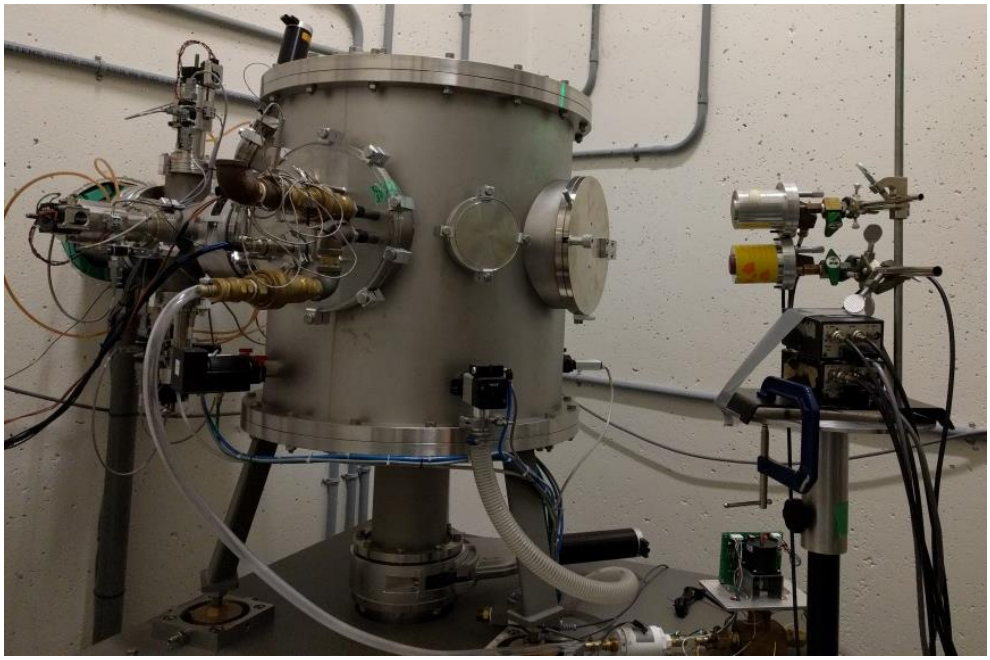

Figure 8-5 Position of the Cy-TEPC and the Cy-GPC in front of the Co-59 target in Room B.

Measurements with the Cy-GPC were conducted at two gas gains to cover not only the smaller events created by high energy protons but also the large energy depositions produced in the heavy ions interactions.

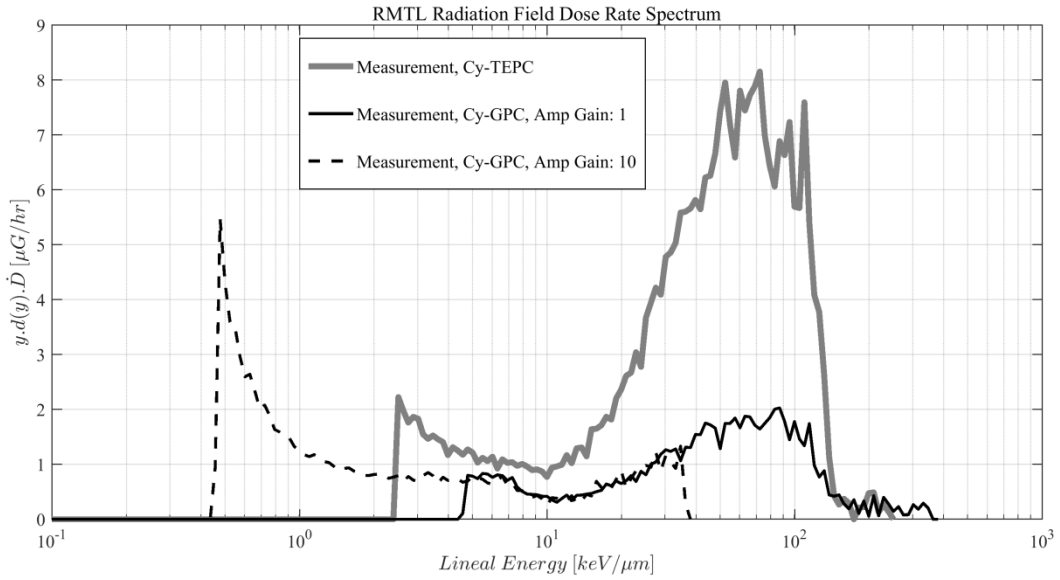

Figure 8-6 Dose rate spectra of the radiation field coming from Co-59 target in room B at the RMTL, measured with the Cy_TEPC and the Cy-GPC (at two gas gains)

As shown in Figure 8-6, the lowest event-size measured by the Cy-GPC is ~0.5 keV/µm (using a gain of 10), whereas the largest event in the spectrum obtained is ~400 keV/µm (using a gain of 1). These two spectra match perfectly in their overlap area from ~5 to ~35 keV/µm, which indicates the reliability of the measurements in this area. However, the lower end of the spectrum measured with the Cy-GPC at the gain of 10 (from 0.5 to 1 keV/µm) and the lower end of the Cy-TEPC measured spectrum (from 2.5 to 4 keV/µm) are not concordant. The events in these two areas, which were measured at high voltages of ~800 V, are most probably contaminated by noise and need to be investigated further in future work to find out the root cause of the noise.

Figure 8-6 also shows that the proton edges of the dose rate spectra measured with the two counters are almost coincident at around 130 keV/µm. The position of the electron edges and

the overall shape of the two spectra are also in good agreement. Moreover, there are noticeable number of events with sizes between 10 to 130 keV/μm recorded by the Cy-GPC, which shows that the Cy-GPC has some sensitivity to the neutrons in this radiation field, although the sensitivity is obviously less compared to the Cy-TEPC. Events larger than 20 keV/μm are certainly not photon-induced but are produced due to neutron interactions. These events are mainly created by protons rather than carbon recoils from the graphite wall. This indicates that there were some interactions between neutrons and the atoms of the tissue equivalent gas inside the graphite counter and recoil protons were created and recorded by the counter. There might also be some events above 300 keV/μm, but they were not collected in this measurement due to the gas gain applied to the counters. Nevertheless, the effect of using the Cy-GPC on the neutron-gamma discrimination was investigated in more detail by subtracting the Cy-GPC recorded events from the Cy-TEPC measured spectrum over the range of 6.5 keV/μm to 20 keV/μm. The start point of this range (6.5 keV/μm) is where the dose rate spectra measured by the Cy-GPC closely matches the dose rate spectra measured by Cy-TEPC. The end point (20 keV/μm) is the upper limit of the overlap area between neutron-induced and photon-induced events. The result of this subtraction is shown in Figure 8-7. This data can be considered the pure neutron spectrum assuming that the Cy-GPC did not record any neutron-induced events smaller than 20keV/μm.

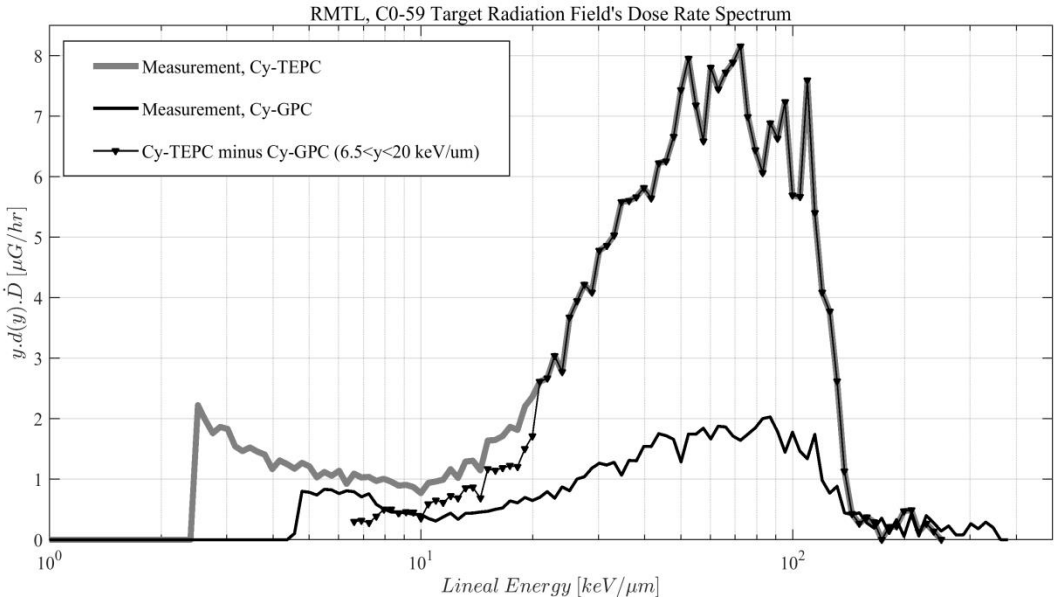

Figure 8-7 Subtraction of Cy-GPC measured data from the dose ate spectrum measured by the Cy-TEPC in the RTML radiation field.

Next, the neutron dose rate value calculated from the neutron spectrum mentioned above was compared against the neutron dose rate obtained from the conventional method, which applied a threshold at 10 kV/μm to the Cy-TEPC measured spectrum. The difference between these values is only about 1.5% as shown in Table 8-1. It is worth noting that this is indeed the maximum difference between the two values due to the fact that the Cy-GPC shows some neutron sensitivity in this radiation field, and therefore, some of the Cy-GPC recoded events in the range of 10 to 20 keV/μm might be neutron-induced. Hence, the neutron dose rate obtained from the subtraction of Cy-GPC from the Cy-TEPC measured spectra would not be much different from the dose rate calculated based on the conventional method. As shown in Table 8-1, the difference between the two spectra drops even further to ~0.4% when the dose equivalent rates are calculated. This means that using a Cy-GPC along with the Cy-TEPC does not make a substantial improvement in measuring the neutron dose/

dose equivalent rate at this radiation field. Nevertheless, using the Cy-GPC at a higher gas gain is beneficial in measuring a complete and therefore more accurate photon dose rate spectrum of this radiation field simultaneously with the mixed-field spectrum measured by the Cy-TEPC.

Table 8-1 Comparison of the RMTL neutron dose rate values obtained in our proposed approach versus the conventional approach

Spectrum	Calculated Dose Rate (μGy/hr)	Calculated Dose Equivalent Rate (μSv/hr)
Cy-TEPC minus Cy-GPC (6.5<y<20 keV/μm)	255.7	4.12 e+03
Cy-TEPC (y>10 keV/μm)	259.7	4.14e+03

To further investigate the neutron sensitivity of the Cy-GPC, the measurement discussed in this section was simulated. The next section provides comparison between the simulated data and the experimental data.

8.2 PHITS simulations

The energy spectrum of the released neutrons from the ^{59}Co target, as measured by Orchard and Waker (Figure 8-4), was used as the neutron energy distribution in the PHITS input code to simulate the counters performance in this radiation field.

The results of this simulation and comparison to the measurement results in section 8.1, are shown in Figure 8-8.

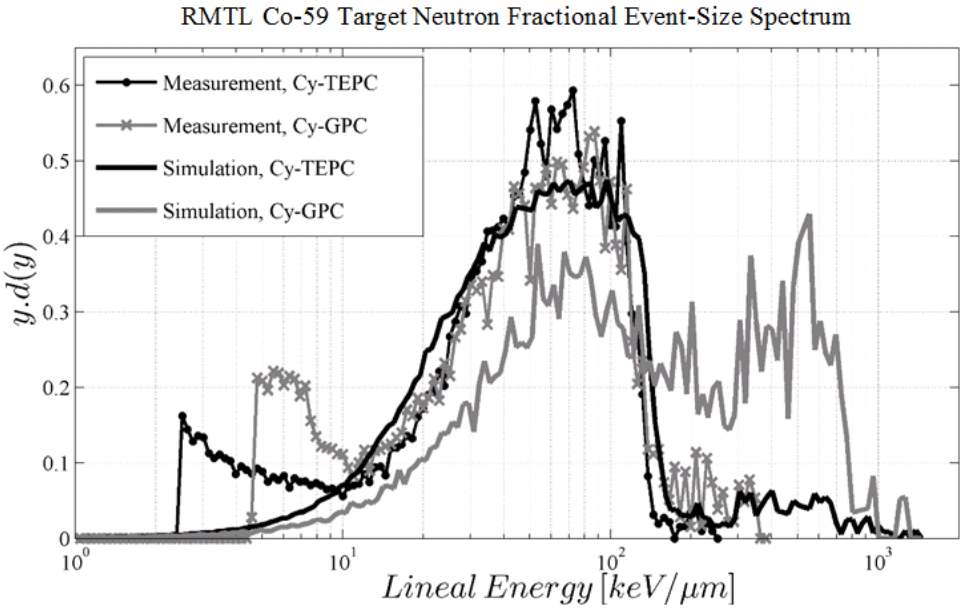

Figure 8-8 Comparison of simulated and measured RMTL released neutrons fractional event-size spectra on 59Co target.

As shown in Figure 8-8, simulation results are in good agreement with measurements in terms of the proton peak and proton edge positions. Moreover, the Cy-GPC simulation event-size spectrum shows noticeable recorded events with lineal energies between 10 and 100 keV/µm just as with the measurement results. Due to normalization and presence of more events above 100 keV/µm, the proton peak of the simulation results appear smaller than the measured data. Having said that, it is obvious that the Cy-GPC is highly responsive to neutrons in this radiation field. A more detailed discussion on this issue can be found at the end of Chapter 9, where similar analysis is conducted for the case of higher energy neutrons at the CERN-EU high-energy Reference Field (CERF) facility.

Simulation results in Figure 8-8 for the Cy-GPC also show more events created by heavier ions i.e. Carbon recoils than the simulated Cy-TEPC.

Moreover, the Simulated Cy-GPC recorded more events created by carbon recoils than the measured spectrum. Due to the applied gas gain to the graphite counter, the measured spectrum only contains the events up to 400 keV/μm. Therefore, it is not possible to make an accurate comparison with the simulation result, which covers the events to up 1500 keV/μm. Moreover, the Cy-GPC recorded several events below 10 keV/μm, mainly created by photons, which are absent in the simulation. If these events are eliminated from the Cy-GPC measured spectrum, the upper end ($100<y<400$ keV/μm) would look bigger due to the normalization effect. After all, the details of the measurement environment, which may affect the neutrons energy distribution through their interactions with the equipment and surrounding walls, was not included in the simulation.

Summary

The neutron-gamma mixed radiation field created due to the interactions of high energy protons produced in the RTML accelerator with the ^{59}Co target material was measured with the Cy-TEPC and the Cy-GPC and also simulated in the PHITS code. The obtained experimental and simulation event-size spectra were in agreement indicating that the Cy-GPC showed higher neutron sensitivity compared to the previous cases in this research. However, when the effect of the Cy-GPC in discrimination of the neutron and photon dose rates in the overlap area between the photon-induced and neutron-induced events (from 10 to 20 keV/μm) was studied, no significant difference was observed from what was obtained with the conventional method. Nevertheless, using the Cy-GPC with a higher gas gain was still beneficial for measuring the photon dose rate spectrum in this radiation field.

Considering that the neutrons in this radiation field have a broad range of energies from 10^{-2} eV up to 10 MeV, it is expected that they undergo various interactions with the wall of the counters and the tissue equivalent gas inside the cavity. These interactions are investigated in the next chapter to better understand the Cy-GPC sensitivity to some neutron radiations.

Chapter 9

High energy neutron component mixed radiation field at the European Organization for Nuclear Research (CERN)

The CERN-EU high-energy Reference Field (CERF) facility has been operational since 1992 for calibration and inter-comparison of active and passive detectors in broad neutron fields (Mitaroff & Silari, 2002). This radiation field is created by a positively charged hadron beam, which consists of 1/3 protons and 2/3 positive pions plus a small kaon component. The beam hits a copper target (50 cm thick and 7 cm in diameter) at a momentum of 120 GeV/c. There are two shielding roofs beside each other on top of the irradiation cave in which the copper target is placed; a concrete shield with a thickness of 80 cm and an iron shield with a thickness of 40 cm (Dinar et al., 2018). As a result of the interactions occurring at the target, secondary charged particles are produced and traverse one of the two shielding roofs depending on the position of the target. Figure 9-1 shows a schematic view of the CERF facility in the North Experimental Hall on the Prévessin site of CERN as modelled in FLUKA [The figure is adopted from (Mitaroff & Silari, 2002) with a few changes]. Each of the roof shields provides an almost uniform radiation field in an area of 2×2 m^2 above it. This area is gridded into 16 squares of 50×50 cm^2 representing radiation exposure locations for measurements. There are also 8 radiation exposure locations on the concrete side. In order to measure the radiation field outside the shield, the detectors should be placed in one of the exposure locations. The main secondary charged particles, which are created when the beam impinges the copper target, are neutrons. However, there are also other particles such as photons, muons, electrons, protons and pions produced in the reactions. These particles,

specifically muons, which come from various sources, cause a significant low-LET background for neutron measurement at the radiation exposure locations. This background needs to be considered in measurements made by devises like TEPCs, which are greatly sensitive to low-LET radiations (Dinar et al., 2018). The detail of the measurements and simulations in this radiation field are studied in this chapter.

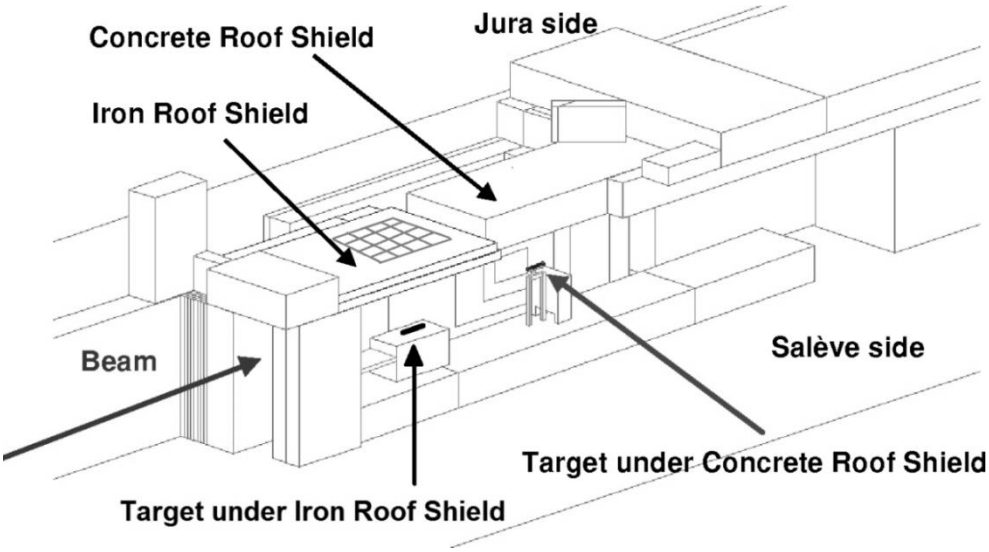

Figure 9-1 Axonometric view of the CERF facility in the North Experimental Hall on the Prévessin site of CERN, modelled in FLUKA, adopted from (Mitaroff & Silari, 2002).

9.1 Experimental measurements

The event-size spectrum of the radiation field at the CERF facility was measured by Orchard and Waker (G. M. Orchard & Waker, 2018) with the Cy-TEPC and the Cy-GPC. The two counters were placed in the 7th radiation exposure location on top of the iron shield

(location IT7) with their center 25 cm above the iron shield. Figure 9-2 shows a view of the iron shield roof gridded for radiation measurements with the counters.

Figure 9-2 Iron shield roof above the target, gridded for radiation measurements at CERF.

Two sets of measurements have been conducted at two different high voltages (643 V and 900 V) applied to the counters to span the event-sizes in a wide range of lineal energies. Applying a higher voltage enables the counter to record lower-LET events, which in this case might be disturbed by the events created by muons (Dinar et al., 2018). Therefore, at the applied high voltage of 900 V, the background radiation of this field has been measured by the two counters. The results of these measurements were converted into dose rate and are shown in Figure 9-3 and Figure 9-4.

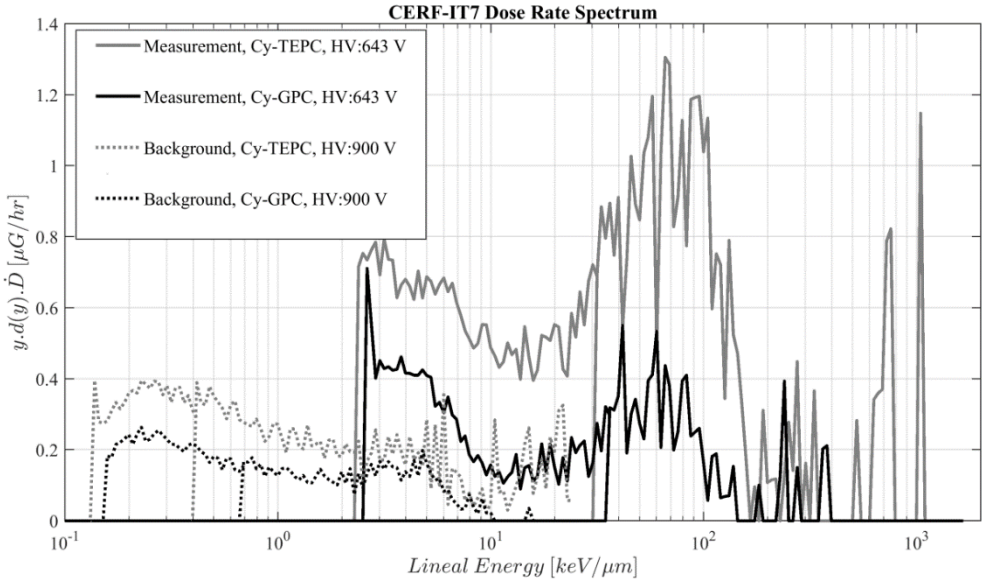

Figure 9-3 Dose rate spectra of the CERF radiation field, measured by the Cy-TEPC and Cy-GPC at the IT7 radiation exposure location, and background dose rate spectra, HV: 900 V.

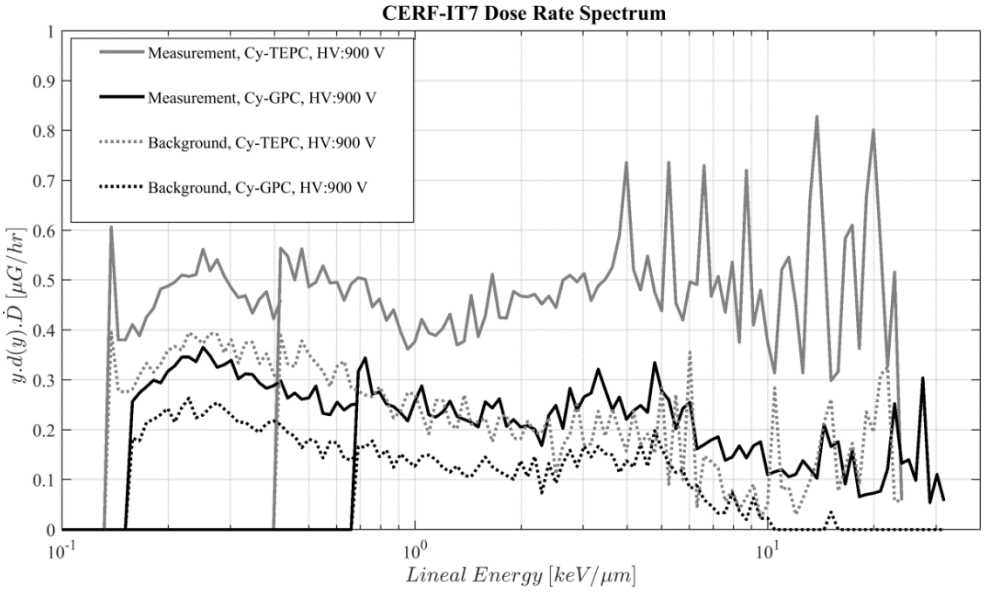

Figure 9-4 CERF radiation field and background dose rate spectra, measured by the Cy-TEPC and Cy-GPC at the IT7 radiation exposure location, HV: 900V.

The background dose rate spectra were then subtracted from the original dose rate spectra measured by the Cy-TEPC and the Cy-GPC to provide a better understanding of the CERF high energy neutrons interactions in these counters (Figure 9-5).

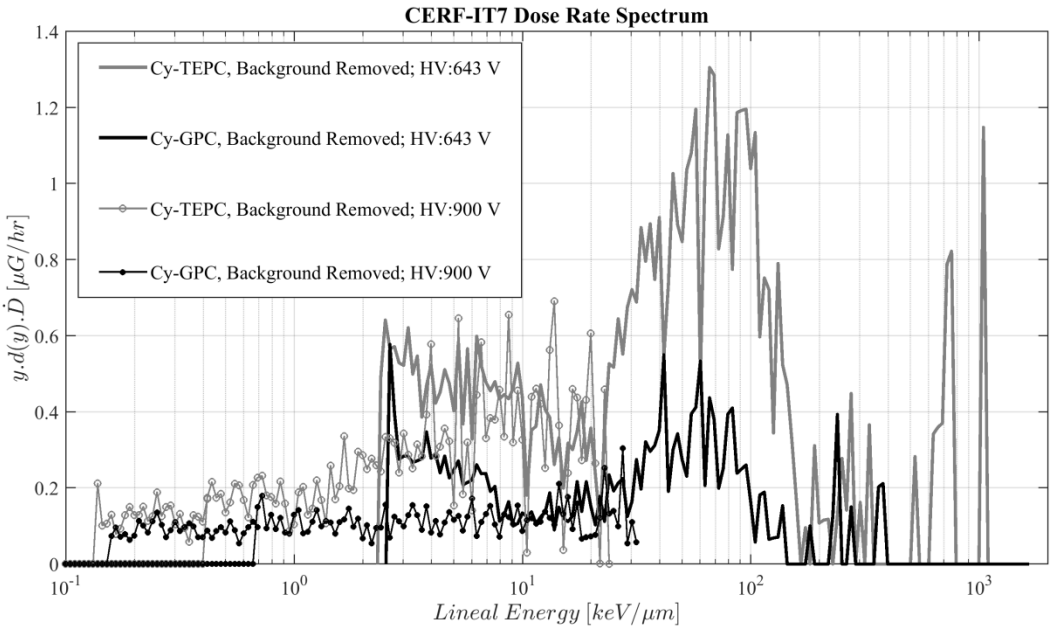

Figure 9-5 Removing background from the CERF dose rate spectra measured with the Cy-TEPC and Cy-GPC.

As it can be seen in this figure, the low-LET events, which are mainly created by photons, can be measured by applying the higher voltage to the counters. Except the area from 3 to 7 keV/μm, where the measured spectra at 643 V are probably contaminated by noise, the upper end of the spectra obtained at 900 V match with the lower part of the data recorded at the high voltage of 643 V. This verifies the reliability of the measurements, specifically in the range of 10 to 20 keV/μm event sizes, which is our region of interest.

Figure 9-5 also shows a good agreement between the Cy-TEPC and the Cy-GPC in terms of the proton edge position at ~130 keV/μm. However, despite our expectation, based on the

results of previous cases, the spectra measured with the two counters do not match in the area of 1 to 10 keV/μm and the Cy-GPC shows fewer recorded events compared to the Cy-TEPC. This does not necessarily mean that the Cy-GPC is less-responsive to photons. The events with the lineal energies smaller than10 keV/μm might be created by other particles in the background radiation not merely photons and the Cy-TEPC is more sensitive to low-LET interactions than the Cy-GPC. The background radiation is also highly variable and changes depending on other experiments going on at the CERN accelerator. Furthermore, the measurements were not conducted simultaneously so the background could be different between the two measurements, in other words, it was higher at the time of the Cy-TEPC measurement. The Cy-GPC also demonstrated a higher-than-expected response to neutrons by showing a considerable proton peak at ~60 keV/μm. Therefore, the neutron dose rate spectrum cannot be obtained by subtracting the whole Cy-GPC measured spectrum from the Cy-TEPC results. Instead, comparison of our proposed method versus the conventional method for finding the neutron dose rate is possible by applying a cut-off at 20 keV/μm on the Cy-GPC measured spectrum and subtract it from the Cy-TEPC measured data at 643 V. The obtained spectrum is shown in Figure 9-6 and the calculated dose rates are compared in Table 9-1.

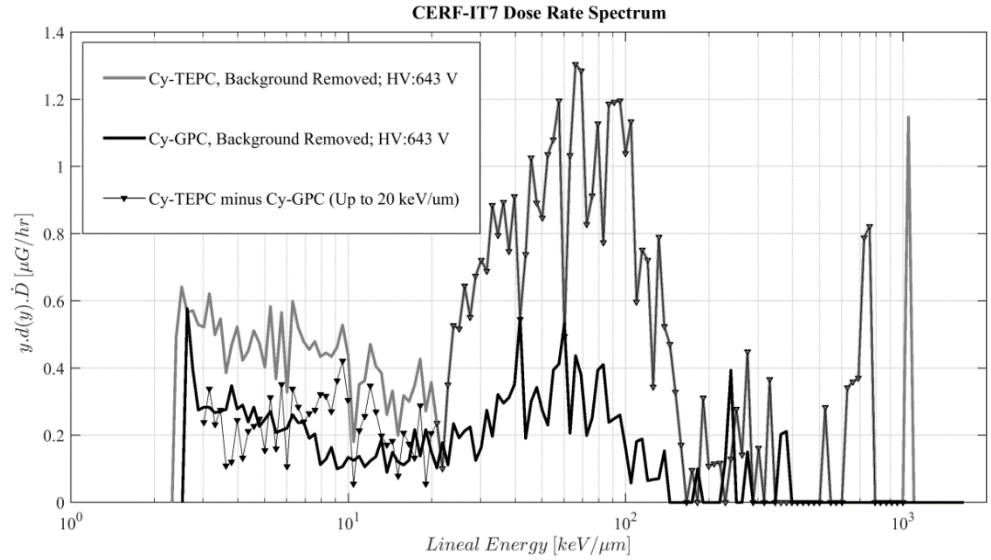

Figure 9-6 CERF neutron dose rate spectrum obtained by subtracting the Cy-GPC measured spectrum (up to 20 keV/μm) from the Cy-TEPC spectrum.

Table 9-1 Comparison of the CERF neutron dose rate values obtained in our proposed approach versus the conventional approach

Spectrum	Calculated Dose Rate (μGy/hr)	Calculated Dose Equivalent Rate (μSv/hr)
Cy-TEPC minus Cy-GPC (3<y<20 keV/μm)	49.8	711.8
Cy-TEPC (y>10 keV/μm)	46.6	721.6

According to the data in Table 9-1, the difference between the neutron dose rates obtained with the dual counters method and the conventional method is ~ -6.7%. This means that the conventional approach slightly underestimates the neutron dose rate in this radiation field compared to the dual counters approach. This difference is even smaller (~-1.4%) for the dose equivalents obtained from the two approaches. Therefore, similar to the case of measuring the neutron dose rate at the RMTL radiation field, adding the Cy-GPC to the Cy-TEPC does not make a significant improvement in measuring the neutron dose rate at the CERF facilities. However, Using the Cy-GPC at a higher HV is still beneficial in measuring the lower LET events created in this radiation field.

For further studies on the counters functionality in a high energy radiation field, these measurements were also simulated in the PHITS code and the comparison results are presented in section 9.2.

9.2 PHITS simulations

The energy distribution of the neutron radiation field at the CERN-EU Reference Field (CERF) facility has been simulated at three positions by Dinar et al. (Dinar et al., 2018) using FLUKA code (Figure 9-7).

Neutron spectral fluence obtained for position IT7 was digitized and used as the neutron energy distribution in the PHITS code input to simulate the measurements conducted by Orchard and Waker (G. M. Orchard & Waker, 2018) with the Cy-TEPC and the Cy-GPC. The output event-size spectra for this high-energy radiation field and comparison to the experimental results are shown in Figure 9-8.

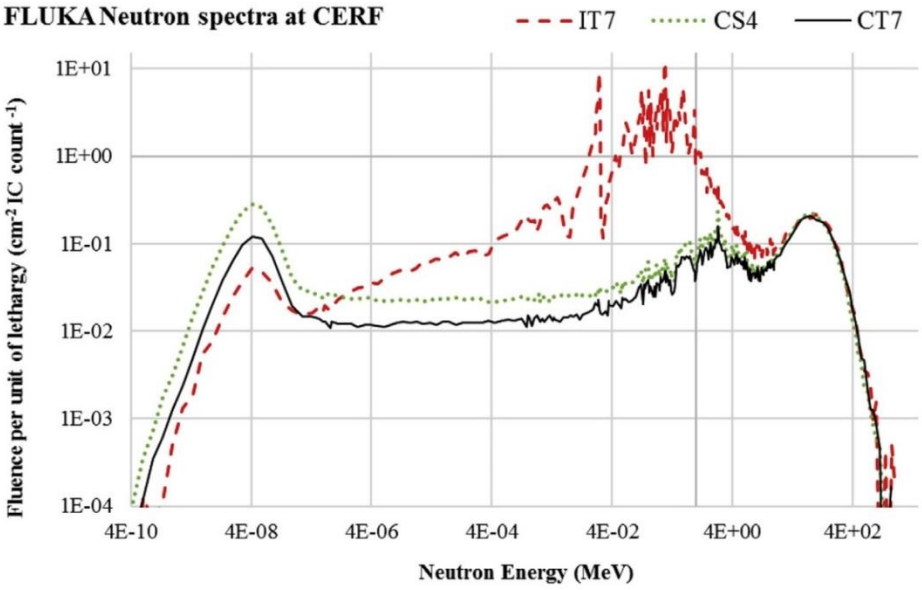

Figure 9-7 Neutron spectral fluence obtained with FLUKA at three positions; IT7, CT7 and CS4 at CERF (Dinar et al., 2018).

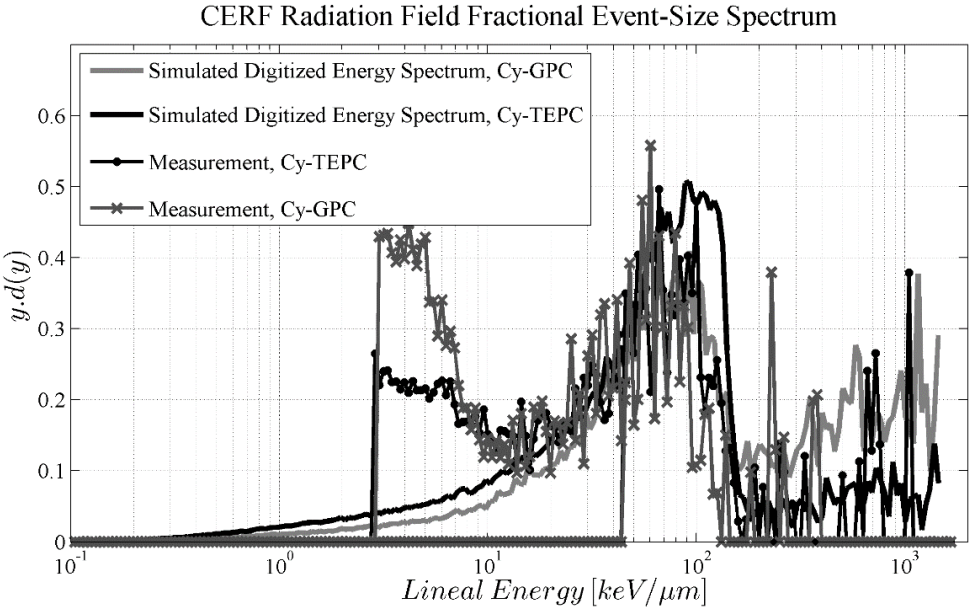

Figure 9-8 Comparison of measurement and simulation results for CERF facility neutrons fractional event-size spectra at position IT7.

As shown in this figure, for both the Cy-TEPC and the Cy-GPC, there is a general agreement between the CERF radiation field fractional event-size spectra measurements and simulation results in terms of the overall shape and the proton peak position. However, similar to the results of the RMTL study in Figure 8-8, the Cy-GPC is highly sensitive to neutrons of the CERF radiation field at IT7 position, and this is verified by measurement and simulation.

In order to take a closer look at these results, the simulated Cy-GPC event-size spectra in these two radiation fields were broken down into their components created by different secondary charged particles and plotted in Figure 9-9 and Figure 9-10. These plots indicate that the events between 10 to ~140 keV/μm are mainly created by protons and to a smaller extent by carbon recoils (nucleus component). Therefore, the next step would be to find out which neutrons in these radiation fields generate protons when interacting with the Cy-GPC graphite wall or the filled gas.

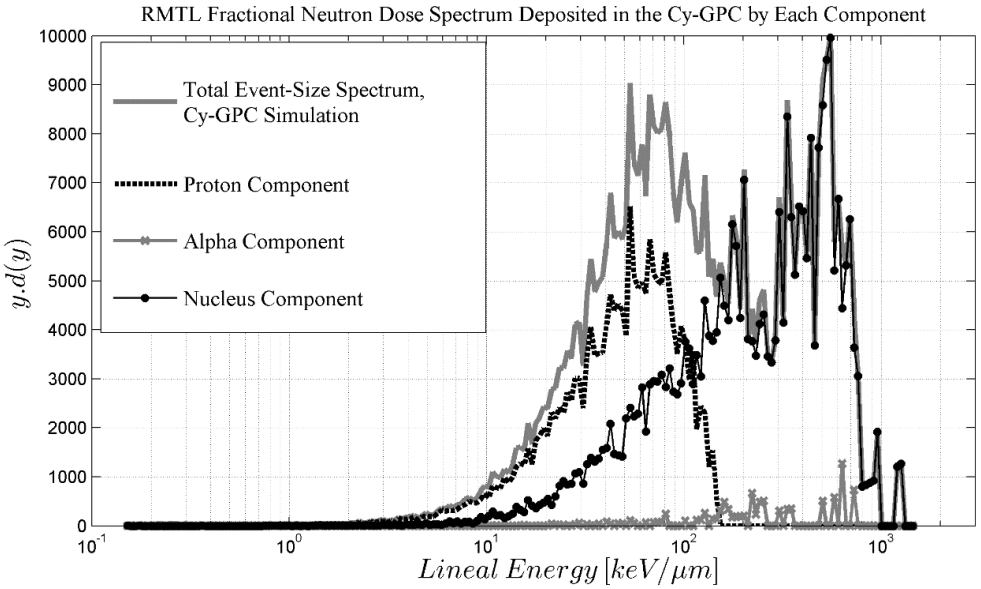

Figure 9-9 RMTL radiation field event-size spectrum broken into components.

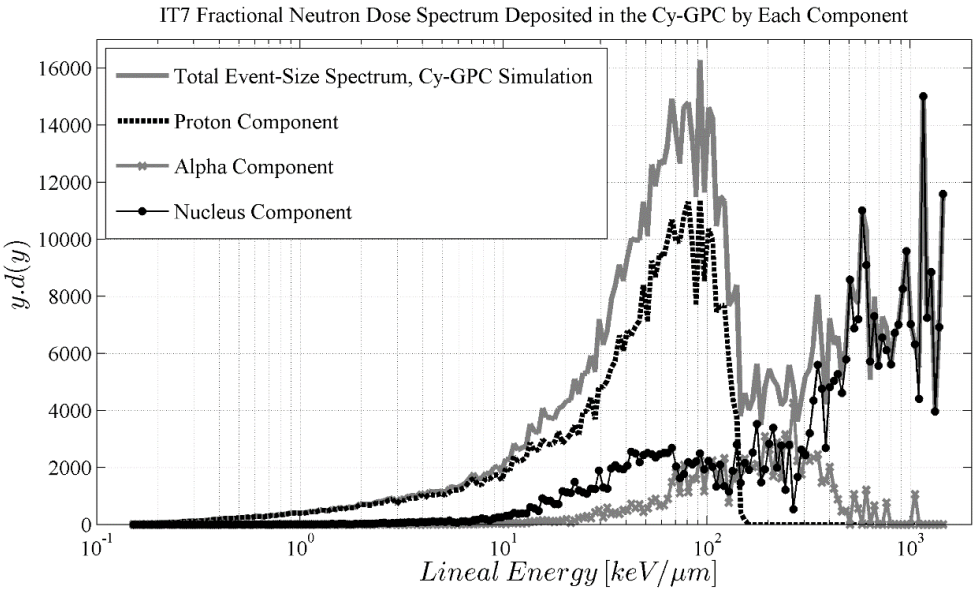

Figure 9-10 CERF radiation field event-size spectrum broken into components.

Since both the RMTL and CERF radiation fields are polyenergetic, it is difficult to come up with an explanation as to why the Cy-GPC is responsive to neutrons in these fields. However, the peaks of the neutron energy distributions of these fields can be assumed as the most dominant energies carried by neutrons. Therefore, by investigating the response of the carbon counter to the neutrons of these energies, the main neutron interactions happening in the counter can be figured out. For this purpose, a few simulations were conducted. In each simulation, neutron source energy corresponds to one of the peaks of the neutron energy distributions of the RMTL and the CERF radiation fields. Figure 9-11 shows the comparison of the Cy-GPC response to two of these monoenergetic neutron radiations that matches to the actual RMTL and CERF event-size spectra in the area of 10 to 100 keV/μm.

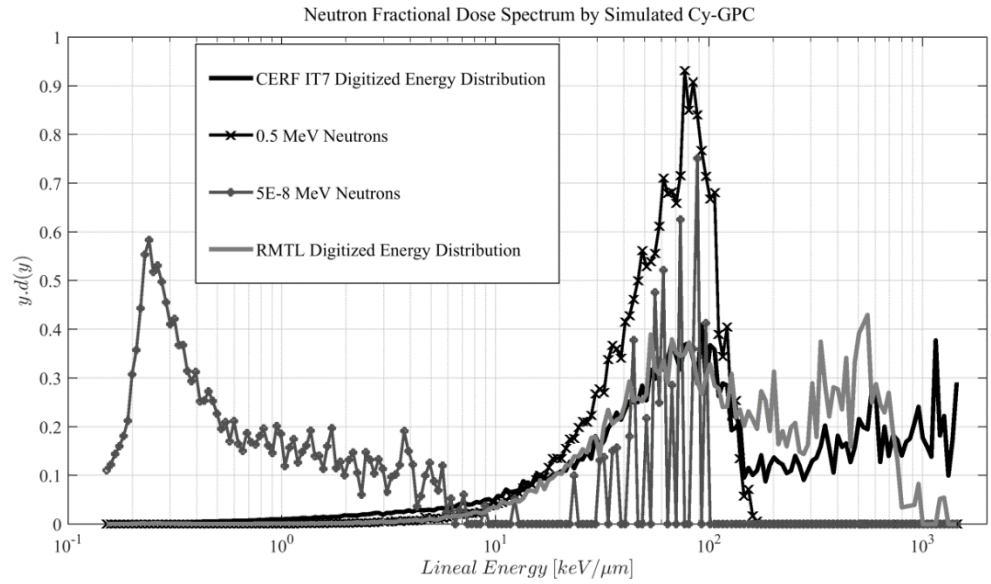

Figure 9-11 Fractional event-size spectra obtained by Cy-GPC simulation and monoenergetic neutron sources corresponding to the peaks of RMTL and CERF neutron distributions.

From this comparison, it seems that the Cy-GPC is mainly sensitive to neutrons with energies of 0.5 MeV and 5×10^{-8} MeV. At these energies, neutrons have great interaction cross sections with Hydrogen (elastic scattering) and Nitrogen ($^{14}N(n,p)^{14}C$) respectively. The cross sections can be found in the (*Sigma Evaluated Nuclear Data File (ENDF) Retrieval & Plotting*; "Sigma Evaluated Nuclear Data File (ENDF) Retrieval & Plotting.,")(*Sigma Evaluated Nuclear Data File (ENDF) Retrieval & Plotting*; "Sigma Evaluated Nuclear Data File (ENDF) Retrieval & Plotting.,") provided by the US National Nuclear data base and the Brookhaven National Laboratory.

In conclusion, although, the Cy-GPC shows very low sensitivity to neutrons because of the graphite wall, it seems that the presence of Hydrogen and Nitrogen in the tissue equivalent

gas inside the counter makes it sensitive to neutrons with specific energies. The results of this study are summarized and some ideas for future work are presented in Chapter 10.

Summary

Similar to the RMTL measurement results, the dual counters approach does not make a significant improvement in measuring the neutron dose rate spectrum at the CERF facilities. However, using the Cy-GPC at a high voltage (i.e. higher than what was applied to the Cy-TEPC), in addition to the Cy-TEPC, is still beneficial in measuring the low LET events of the CERF radiation field simultaneously.

On the other hand, the Cy-GPC showed noticeable response to neutrons in the CERF dose rate measurements. It measured several events with sizes between 10 to 100 keV/μm just like its response to the RMTL neutrons. The neutron energy distributions in these two radiation fields are different from each other. There are higher energy neutrons at the CERF facility, and they may interact with the graphite wall of the counter and create carbon recoils with higher lineal energies (≥100 keV/μm). However, the high amount of data with lower lineal energies in both radiation fields was unexpected and needed to be further investigated. The measurements in these radiation fields were also simulated in the PHITS code and similar results were found. These results reinforced the conjecture of neutron interactions with the tissue equivalent gas inside the graphite counter. To find the interactions responsible for the Cy-GPC neutron sensitivity, the peaks of the neutron energy distributions of these two radiation fields were assumed as the most dominant neutron energy values. Some simulations were then conducted to evaluate the Cy-GPC response to the monoenergetic neutron

radiations corresponding to these values. The Cy-GPC showed most sensitivity to two of these neutron energies mainly through the reactions with Hydrogen and Nitrogen atoms. The conclusion drawn from this observation is that for making the heterogeneous counter insensitive to neutrons, it is not sufficient to make the wall out of Graphite, because the tissue equivalent gas inside the counter is sensitive to neutrons at specific energies.

Chapter 10

Conclusions and recommendations for future work

10.1 Summary of the research

In this thesis the idea of using a set of twin proportional counters for neutron-gamma dosimetry in mixed-radiation fields was investigated. Photons exist almost everywhere that neutrons are generated, but create different radiobiological effects from that of the neutrons. Therefore, discrimination of the absorbed dose deposited by each of these components of a mixed-radiation field is of great importance, especially in radiation protection and radiation biology sciences. An established method in neutron dosimetry is using TEPCs to measure the

lineal energy dose spectrum of the mixed-field. Then, the best available photon event-size spectrum is subtracted from the mixed-field spectrum to find the neutron event-size spectrum. However, finding a photon dose spectrum, which fits the intended radiation field, might be neither easy nor accurate, especially in unknown radiation fields, for which applying an arbitrary gamma spectrum may result in lower accuracy dosimetry. Therefore, one way to improve the accuracy of this method would be to find a way of measuring the actual photon dose spectrum.

The approach of this research, which was explained in Chapter 1, was to develop a heterogeneous proportional counter to measure the pure photon dose-rate spectrum for the purpose of mixed-field dosimetry, the counter was expected to be insensitive to neutrons, because of its graphite wall. The ultimate goal of this study was then to explore the plausibility of a single device for neutron dosimetry in neutron- gamma mixed radiation fields. A brief description of the study strategy through experimental measurements and computational simulations was also presented in Chapter 1.

In the second chapter, the study methodology was explained in details. A general background of microdosimetry, the principles, quantities and parameters involved in this field were described. Then, the fundamentals of experimental microdosimetry and its application in dosimetry using a TEPC, as the most well-known device in this area, were explained. Operational principles of TEPCs were reviewed and it was demonstrated how a TEPC could simulate tissue sites in size and material composition. Then, some technical details about the calibration of the counters used in this research were explained. It was also mentioned that in some of the mixed-field measurements, two amplifiers needed to be used simultaneously, to

collect all the events created by photons and neutrons. In these measurements each amplifier recorded part of the event-size spectrum depending on the applied gain. A method was suggested to combine the two spectra and cover a broader range of event-sizes, so that the counter performance was evaluated over the whole range of events created by both photons and neutrons.

Chapter 3 presented a literature review on the experimental and computational methods, which have been used prior to this research for neutron-gamma mixed field dosimetry. In terms of the experimental efforts that have been done for neutron dosimetry, two main ideas were discussed in this section. The first one was the twin-chamber method, in which one ion chamber was sensitive to both neutrons and photons and the other one was only sensitive to photons. The neutron dose was then calculated by subtracting the photon dose value from the mixed-field dose. This method worked well at the time. However, since ion chambers work only in current mode, not pulse mode, the output of this measurement was the total neutron dose value, and the frequency of the absorbed dose at each lineal energy was not available. Therefore, the pattern of neutron energy deposition in a medium could not be studied by this method. The second well-stablished method for neutron dosimetry is measuring the mixed field dose spectrum with a TEPC. Then, a photon dose spectrum would be fitted and subtracted from the mixed-field spectrum to find the neutron dose spectrum. As was mentioned before, this method includes inaccuracies due to the uncertainties in choosing the appropriate photon dose spectrum. The idea of twin-counters proposed in this research was in fact a combination of the two aforementioned methods to provide an accurate measurement of the photon dose spectrum with developing a heterogeneous proportional counter.

Chapter 3Chapter 4 included the explanation of experimental and computational approach of this study to implement the proposed idea. First, the details of the counters design used in the measurements were described. The twin counters were a Cylindrical TEPC (Cy-TEPC) and a Cylindrical Graphite Proportional Counter (Cy-GPC), both of them had identical geometry and tissue equivalent filling gas. However, the wall of the Cy-GPC was made of Carbon, which is insensitive to neutrons, but has very similar sensitivity to photons as the Cy-TEPC. A commercial 5" spherical TEPC (from Farwest technology) was also used in some of the measurements as a benchmark for the Cy-TEPC's operation. Before conducting the actual mixed-field measurements, it was necessary to verify that the twin counters had the same response to photons, but very different sensitivities to neutrons. For this purpose, the counters tested in four photon radiation fields: 20 keV, 65 keV and 120 keV X-Rays and 0.662 MeV Cs-137 gamma radiation fields. Through these measurements, the two cylindrical counters showed very similar sensitivity to photons. Then the counters were used in measuring the 2.5 MeV pure neutron radiation field. As it was expected, the Cy-GPC showed almost no sensitivity to these neutrons. On the other hand, the 2.5 MeV neutrons dose rate spectrum measured by the Cy-TEPC had a very similar shape to the dose rate spectrum measured by the 5" TEPC. However, the Cy-TEPC spectrum was shifted towards higher lineal energies and a difference of 15% to 20% was observed between the positions of the two TEPCs dose rate spectra. This issue was not an obstacle in implementing the twin-counters idea, because the position of the spectra measured by the Cy-TEPC and the Cy-GPC still matched perfectly. The difference between the cylindrical and spherical TEPCs measurements was further investigated in chapter 5 and 6.

In addition to the experimental measurements, the counters were simulated using the PHITS Monte Carlo code, to benchmark the code against the measurement results. This code was chosen based on the comparison between different computational methods used for low energy neutron and gamma ray fields, made by Ali [(Ali et al., 2013)]. A description of the PHITS tallies and sections used for conducting the simulations was also provided in chapter 4. PHITS simulations conducted in this chapter also verified that the Cy-GPC was almost insensitive to neutrons.

After verifying the insensitivity of the Cy-GPC to neutrons, a set of neutron-gamma mixed field measurements and simulations were conducted with the twin counters to evaluate their performance in a wide range of neutron energy in the next chapters. These radiation fields included:

- Neutron-gamma mixed radiation field at the Ontario Tech University radiation protection laboratory,
- 14.8 MeV neutron irradiation field at the Physikalisch-Technische Bundesanstalt (PTB), Braunschweig,
- Broad spectrum source of ^{241}Am-Be,
- High gamma component mixed radiation field at Kingston Reactor Materials Testing Laboratory (RMTL),
- High energy neutron component mixed radiation field at the European Organization for Nuclear Research (CERN).

For the mixed radiation field of 2.5 MeV neutrons and Cs-137 gamma rays, which was studied in Chapter 5, the two counters performance was exactly as expected. The Cy-GPC recorded some photon-created events above 10 keV/μm, which in the conventional method was considered as the threshold for neutron-created events. Therefore, the neutron dose rate which was calculated by subtracting the photon dose rate from the mixed-field dose rate was smaller and more precise than what was obtained from the conventional method. However, this difference was small enough to be of concern only in radiation biology rather than radiation protection measurements.

When the counters and the conducted measurements were simulated in PHITS, the exact same event-size spectrum of 2.5 MeV neutrons obtained by measurements was generated in simulation. The comparison between the results of the simulated spherical and cylindrical TEPCs also showed the same difference in the position of the spectra observed in the measurements data. In both cases the spectrum measured by the Cy-TEPC was shifted towards higher lineal energies compared to the spherical TEPC data.

In Chapter 6, another simulation was conducted for the monoenergetic 14.8 MeV neutron field, whose dose rate spectrum was measured with the 5" spherical TEPC at the Physikalisch-Technische Bundesanstalt (PTB) laboratories in another work (**Alberts**, 1989). The overall shape and fluctuations of the simulated and measured dose spectra with the 5" spherical and Cy-TEPC matched well. The shift to higher lineal energies between the simulated Cy-TEPC and the simulated 5" TEPC was observed in this case too. However, the dose spectrum measured with the 5" TEPC was matched to the simulated Cy-TEPC

spectrum, rather than the simulated 5” spherical counter. This probably happened due to inaccuracy in the calibration of the 5” TEPC in the measurements.

The shift between the positions of the event-size spectra measured with the cylindrical and spherical TEPCs were observed in both measurements and simulations for the monoenergetic 2.5 MeV and 14 MeV neutrons. The most probable reason for this shift seemed to be the geometry effect of the counter. Therefore, the chord length distributions in a sphere and in a right cylinder were investigated and compared together in section 6.2. According to the geometry comparison, the maximum chord length in a sphere is its diameter, while in a cylinder, energetic particles may traverse across chords longer than the cylinder diameter, and thus, they may deposit more energy inside the Cy-TEPC. That is why the event-size spectrum obtained by the Cy-TEPC, both in experiments and simulations, were shifted towards higher lineal energies. This difference might need to be considered when the performance of a cylindrical and a spherical TEPC is compared. However, with the twin-counters method, in which both the counters have the same geometries, this issue is not a concern.

The other mixed field dose rate spectrum, which was measured with the twin counters was the broad neutron spectrum of the ^{241}Am-Be source at the radiation protection laboratory of the Ontario Tech University. The details and results of the measurements and simulations of this radiation field were explained in Chapter 7. The neutron dose rate of this radiation field was also obtained by subtracting the photon dose rate spectrum, measured by the Cy-GPC, from the Cy-TEPC measured spectrum. In the obtained neutron dose-rate spectrum however, there were some events recorded below 10 keV/μm. These events could have been created

either by higher energy protons with smaller stopping power, or by the energetic protons, which traversed the very small chord lengths across the counter cavity and deposited only a part of their energy. The results of the ^{241}Am-Be radiation field measurements were also replicated by simulations and it was confirmed that the neutron event-size spectrum included some events below 10 keV/μm. These events made a difference of ~5% in the neutron dose rate value compared to the value obtained from the conventional method by applying the threshold of neutron-created events at 10 keV/μm. Therefore, it was confirmed that using the twin counter method proposed in this research improves neutron dosimetry accuracy. On the other hand, the ^{241}Am-Be event-size spectrum measured by the Cy-TEPC showed more events with higher stopping power and had a proton peak at higher lineal energy compared to the simulation results with the Cy-TEPC. This difference is probably due to the existence of more low energy neutrons in the measurement area compared to the PHITS simulation, in which the details of the laboratory environment and contents were not included. Therefore, the interactions of fast neutrons to the surrounding walls and equipment of the lab, which lead to the creating of lower energy neutrons, were not considered. Less energetic neutrons have higher stopping power and deposit more energy, which leads to larger events inside the counter.

This study concluded by evaluating the twin counters functionality in the mixed radiation fields of the RMTL (Queen's University) and CERF facilities and the results were discussed in Chapter 8 and Chapter 9. The neutron energy ranges of these two radiation fields were different and higher energy neutrons were produced at the CERF radiation field. However, in both cases the Cy-GPC showed much more than expected sensitivity to neutrons with

recording significant number of events large than 20 keV/μm. Nevertheless, in the range of 10 to 20 keV/μm events, which was basically considered as the overlap area for the events created by photons and neutrons, the Cy-GPC measured fewer events. Therefore, the Cy-GPC was assumed almost insensitive to neutrons in this area. The effect of using the twin counters method on discriminating the neutron-induced and photon induced events was then investigated by subtracting the Cy-GPC recorded data (up to 20 keV/μm) from the Cy-TEPC measured spectrum. The resulting neutron dose rate spectrum was compared to the spectrum obtained by applying the threshold of neutron dose rate spectrum at 10 keV/μm. In the case of RMTL measurements, the neutron dose rate value found in the twin counter method was ~1.5% less and in the CERF measurements, it was ~6.7 % higher than the conventional method result in each radiation field. The difference in the dose-equivalent rate values obtained with our approach and the conventional method was even smaller in both cases. Thus, from the radiation protection point of view using the twin counters method did not seem to have any advantage over the conventional method.

In both cases the simulation results were also in agreement with the experimental data and verified the sensitivity of the Cy-GPC to neutrons in these radiation fields. This problem was further investigated in section 9.2 to find out the reason for the graphite counter's sensitivity to these neutrons. Since both of the RMTL and CERF radiation fields contained polyenergetic neutrons, it was not easy to find out the exact neutron energies to which the Cy-GPC was sensitive. Therefore, the neutron spectral fluence of the two fields was broken down into some monoenergetic neutron radiations corresponded to the peaks of the neutron energy distributions at these facilities. The two counters were then modeled in PHITS to

investigate the sensitivity of the Cy-GPC to each of these neutron energies. It was also necessary to find out whether the neutrons interacted with the graphite wall or the filled gas inside the Cy-GPC.

According to the simulation results, the Cy-GPC was found to be sensitive to neutrons with the energies of ~0.5 MeV and ~5×10^{-8} MeV. Then, the event-size spectra of the two radiation fields were broken down into components and it was realized that the main particles that contributed in creating events between 10 and 100 keV/μm were protons. Considering the energy and the product of the neutron interactions in the Cy-GPC, the interaction responsible for the neutron sensitivity of the counter were found to be $^{14}N(n,p)^{14}C$. It was thus verified that the neutrons mainly interacted with the nitrogen atoms in the gas inside the Cy-GPC's cavity and the Graphite wall of the counter was insensitive at least to the lower LET particles. Therefore, in order to develop the GPC so that it is insensitive to all neutron energies, the gas inside the counter should be changed, not the wall material.

Table 10-1 summarises the microdosimetric quantities in the conducted mixed-field measurements of this study, and the statistical uncertainties, which were calculated based on the error propagation formulas in section 0 and Appendix CAppendix AAppendix B. In each radiation field, the mixed-field component was measured with the Cy-TEPC and the photon component was measured with the Cy-GPC. In each case the neutron component was obtained by subtracting the photon dose rate from the mixed field dose rate.

Table 10-1 Frequency mean lineal energy, dose-mean lineal energy and dose-rate values for neutron-gamma mixed field measurements

Radiation Field	Radiation Component	$\bar{y}_F$ (keV/μm)	$\bar{y}_D$(keV/μm)	$\dot{D}$ (μGy/hr)
2.5 MeV neutrons + Cs-137 photons	Mixed Field	25.42 ± 4.37e-1	46.73 ± 1.39	48.08 ± 6.63e-1
	Photon	0.50 ± 2.6e-4	1.83 ± 2.5e-3	9.75 ± 1.54e-1
	Neutron	-	-	38.33 ± 1.13
Am-Be	Mixed Field	14.43 ± 7.07e-2	36.27 ± 3.99e-1	340.52 ± 1.70
	Photon	1.86 ± 2.98E-3	3.25 ± 8.45e-3	26.13 ± 2.27e-1
	Neutron	-	-	314.39 ± 4.31

RMTL accelerator facility	Mixed Field	21.37 ± 2.63e-1	56.97 ± 1.14	298.26 ± 3.13
	Photon	26.13 ± 4.70e-1	64.69 ± 2.36	81.74 ± 1.24
	Neutron	-	-	255.7 (6.5<y<20)
CERF (643V)	Mixed Field	11.85 ± 3.40e-1	95.25 ± 17.43	70.56 ± 1.96
	Photon	8.62 ± 2.98e-1	43.75 ± 6.30	24.71 ± 7.81e-1
	Neutron	-	-	49.8 (3<y<20)
CERF (900V)	Mixed Field	1.20 ± 2.45e-2	*6.53 ± 2.66e-1*	28.34 ± 4.76e-1
	Photon	0.99 ± 2.76e-2	6.99 ± 3.98e-1	12.75 ± 2.92e-1
	Neutron	-	-	-

Additionally, Table 10-2 provides a summary of the frequency mean lineal energies and the dose mean lineal energies obtained through simulations for the neutron component of the radiation fields studied in this thesis.

Table 10-2 Frequency mean lineal energy and dose-mean lineal energy for the neutron radiation fields simulations

Simulated Radiation Fields	$\bar{y}_F$ (keV/µm)	$\bar{y}_D$(keV/µm)
2.5 MeV neutrons	36.72 ± 1.7e-1	78.06 ± 9.7e-1
14.8 MeV neutrons	11.96 ± 1.88e-2	142 ± 1.11
^{241}Am-Be neutrons	20.65 ± 9.0e-2	100.87 ± 2.42
RMTL neutrons	30.88 ± 2.0e-1	84.48 ± 2.20

CERF neutrons	11.96 ± 1.2e-2	139 ± 7.34

10.2 Conclusion and recommendations for future works

After conducting many measurements and simulations for different neutron energies it has been shown that the Graphite walled Cy-GPC is largely insensitive to neutrons. Although fast neutrons may interact through elastic scattering and create carbon recoils, they and other incident neutrons, which have almost no interactions with carbon, lead to very few energy deposition events in the overlap region of lineal energy between the carbon-walled Cy-GPC and the tissue equivalent Cy-TEPC. Therefore, the idea of using twin proportional counters to measure both photon and neutron components of a mixed-field has been demonstrated to be completely feasible and potentially much simpler than conventional methods employing different detector types with different working principles. However, at very low energies, neutrons may interact with tissue equivalent gas through the $^{14}N(n,p)^{14}C$ reaction, because of the presence of nitrogen. The fill gas inside the graphite counter was primarily chosen to make it match the Cy-TEPC, since the heterogeneous counter ideally should be insensitive to neutrons yet measure the photon dose to tissue accurately. The tissue equivalent gas inside the Cy-GPC could be replaced by another gas or gas mixture containing no nitrogen atoms. The first option that seems appropriate for a nitrogen free counting-gas is carbon dioxide. Thus, the expectation is that a graphite walled counter filled with CO_2 would be almost completely insensitive to neutrons, while measuring the same photon dose as a TEPC. However, due to the low drift velocity of electrons in CO_2 (Povinec, 1979), it may not have a

suitable gas gain to be used as an alternative for TE-gas. Further research on the properties of other counting gas mixtures to use in graphite walled proportional counters is obviously needed.

Another improvement worth future study is to change the geometry of the twin counters. As mentioned before, the ultimate goal of this research is to design a single device for neutron-gamma mixed field dosimetry. The current cylindrical shape was chosen for the counters to make the manufacturing in a research workshop easier. A cylinder of equal height and diameter was also considered as the most similar geometry in terms of chord-length distribution to the spherical shape of the reference 5" TEPC, which was a benchmark counter in this study. However, as it was observed in practice, there was an approximate 15% shift between the dose spectra measured by cylindrical and spherical TEPCs. The shift occurs due to the availability of chord-lengths longer than the cylinder's diameter when charged particles traverse in a cylindrical cavity. This shift may result in underestimating the neutron dose measurement in the region of 10 to 20 keV/μm, which is the overlap area between the photon and neutron dose spectra and will cause some uncertainties in measured microdosimetric quantities, such as mean quality factors and dose-mean lineal energy ($\bar{y}_D$). An optimal design however could be a hemispherical shape for each of the two counters, thus enabling an overall spherical geometry, which would make a twin chamber arrangement physically compact and also isotropic in response. This design has been theoretically studied by Broughton and Waker (Broughton & Waker, 2017) with promising results. However, this design has only been modelled and simulated for two monoenergetic neutron radiation fields

and actual counters need to be constructed and validated with experimental measurements in a range of different mixed-radiation fields.

Another factor to be considered in manufacturing a single device for mixed-field dosimetry is the counter's sensitivity in terms of counts per unit dose rate. The sensitivity of a counter in terms of counts per micro-Sievert per hour depends principally on its size (cross-section) and also on radiation type. As shown in previous studies (A. Waker, Szornel, & Nunes, 1997), the 5" TEPC has adequate sensitivity to make it suitable for neutron monitoring in nuclear power plants. Another study (Qashua & Waker, 2011) also discussed that when TEPCs sensitive enough for neutron monitoring are used in mixed-radiation fields, the potential of pulse-pile-up at low event-sizes can be problematic. This study also provided further justification as to why using a separate counter for the photon component is a good idea. Moreover, the photon dose rate is often greater than the neutron dose rate in a power plant mixed-radiation field. Therefore, the neutron counter would be expected to be larger than the photon counter in physical size, meaning that different gas pressures should be applied to the two counters to simulate the same tissue site size. This complication undermines the philosophy behind designing a single device. An alternative would be to have a multi-element counter with one element made of graphite while the majority of elements are made of tissue equivalent plastic. Since the size of each element is the same in this design, the same gas pressure can be applied to all the elements. The first design of a multi-element TEPC, which was developed at Columbia University (Rossi, 1983), was complex due to the requirement of maintaining a uniform electric field in each counting element (Kliauga, Rossi, & Johnson, 1989) and subsequent work on this design has not been reported. However, in the

METEPC design, introduced later by Waker, an anode wire support arrangement was designed and implemented, resulting in a smaller and simpler design of the individual counting elements (A. Waker, 2010). A most recent study has focused on a multi-element counter with hemispherical geometry to improve isotropic response and robustness of the counter by avoiding ultra-thin anode wires. Preliminary design options in the study indicates the potential for a more compact design compared to the dual-counter concept (Ali & Waker, 2019).

Finally, in summary, this study has shown that despite constraints due to the physics of radiation interaction, the prospects for a single device based on carbon and tissue equivalent walled proportional counters for nuclear power plant and nuclear facilities mixed field monitoring are excellent.

Appendix A

Neutron interaction cross sections with H, C, N, and O nuclei

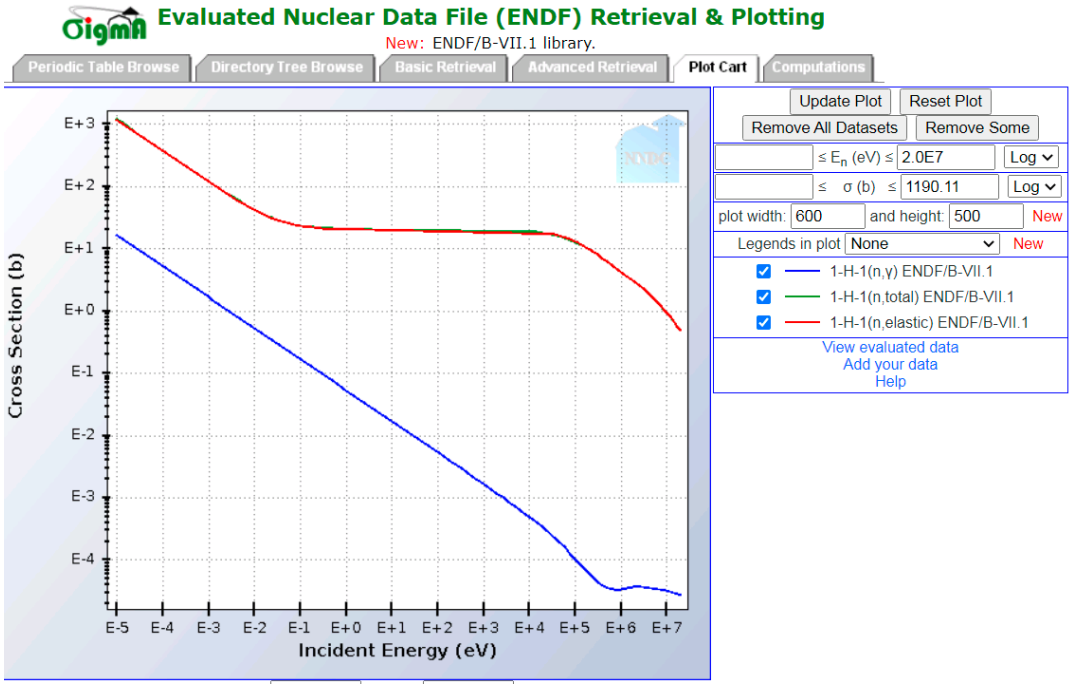

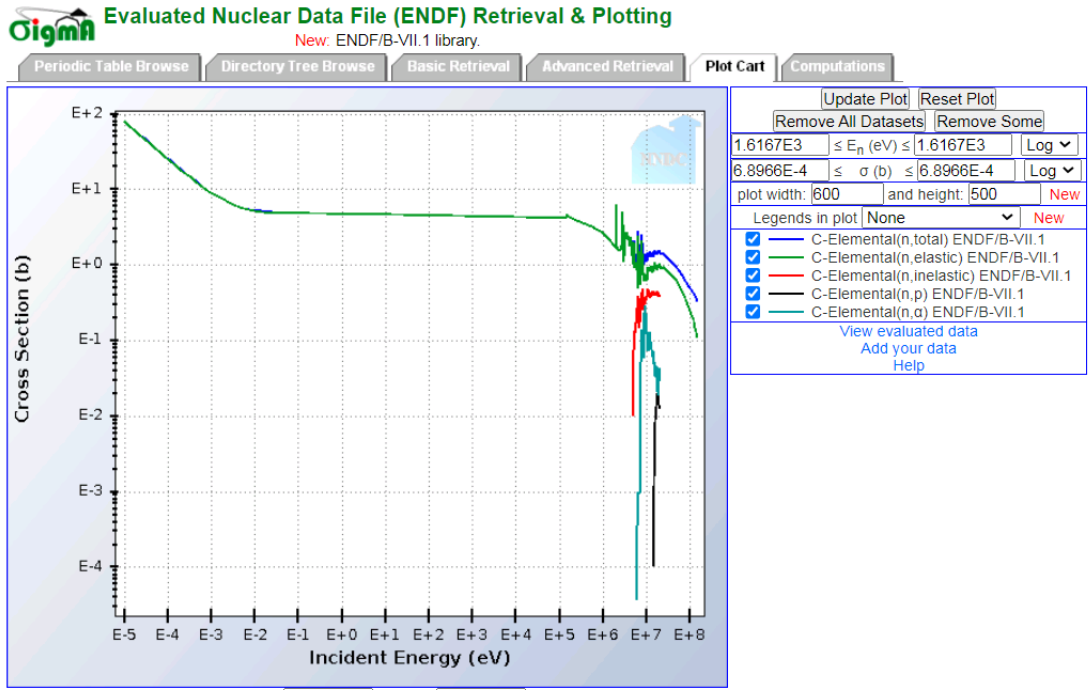

z

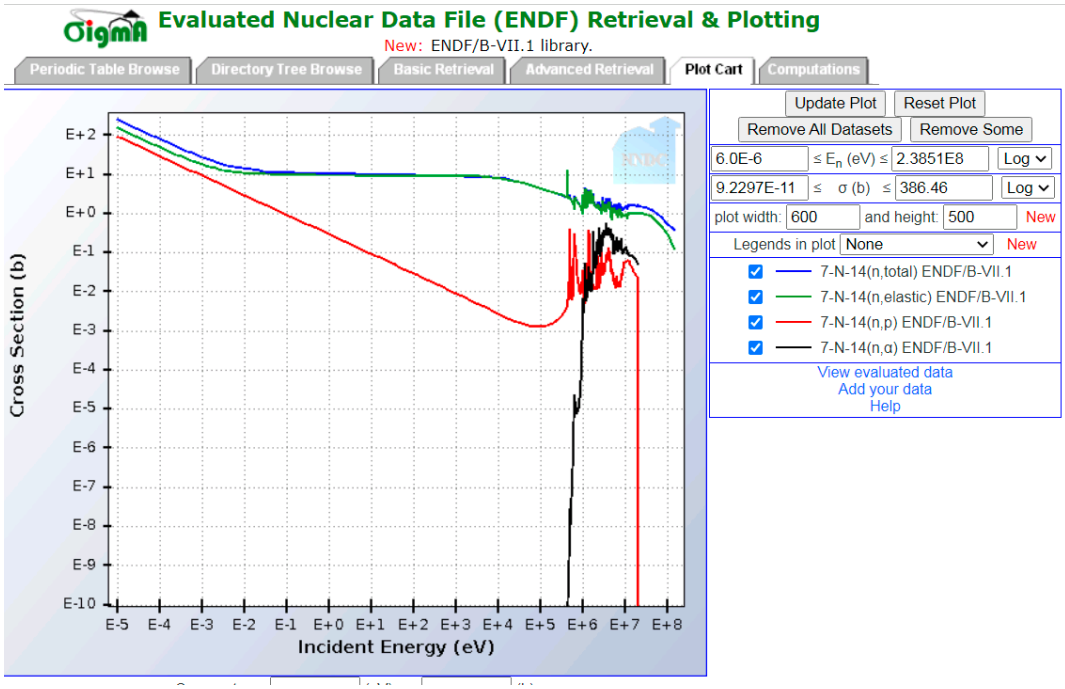
Evaluated Nuclear Data File (ENDF) Retrieval & Plotting
New: ENDF/B-VII.1 library.
Periodic Table Browse
Directory Tree Browse
Basic Retrieval
Advanced Retrieval
Plot Cart
Computations
Update Plot
Reset Plot
Remove All Datasets
Remove Some
6.0E-6 ≤ E_n (eV) ≤ 2.3851E8 Log
9.2297E-11 ≤ σ (b) ≤ 386.46 Log
plot width: 600 and height: 500 New
Legends in plot None New
7-N-14(n,total) ENDF/B-VII.1
7-N-14(n,elastic) ENDF/B-VII.1
7-N-14(n,p) ENDF/B-VII.1
7-N-14(n,α) ENDF/B-VII.1
View evaluated data
Add your data
Help
Cross Section (b)
E+2 E+1 E+0 E-1 E-2 E-3 E-4 E-5 E-6 E-7 E-8 E-9 E-10
E-5 E-4 E-3 E-2 E-1 E+0 E+1 E+2 E+3 E+4 E+5 E+6 E+7 E+8
Incident Energy (eV)

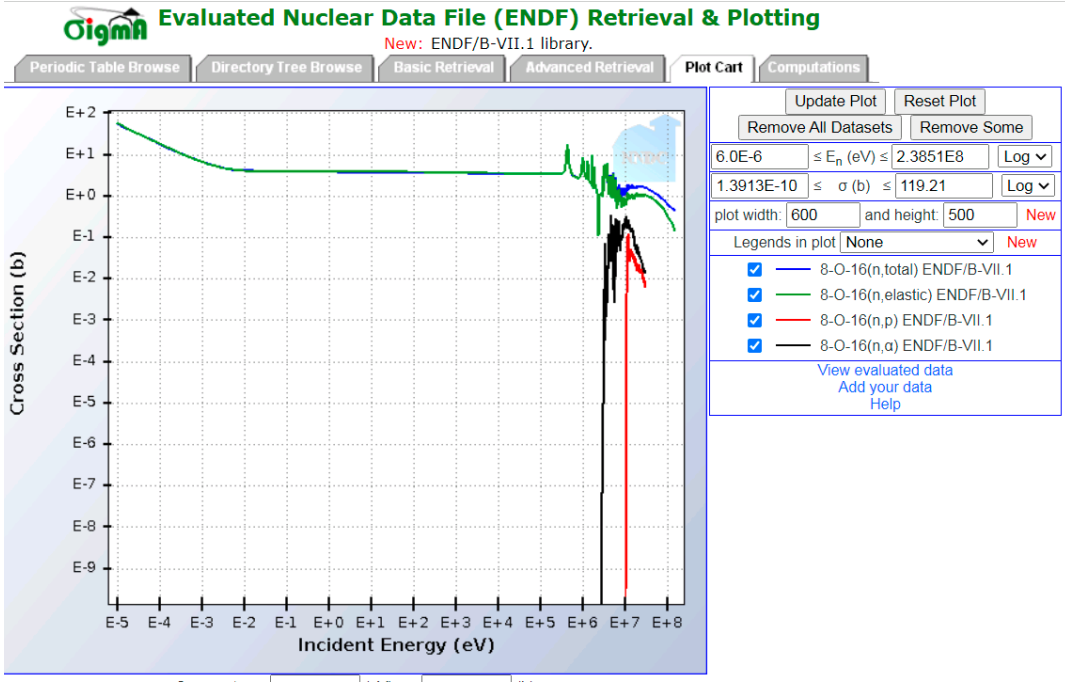
Evaluated Nuclear Data File (ENDF) Retrieval & Plotting
New: ENDF/B-VII.1 library.
Periodic Table Browse
Directory Tree Browse
Basic Retrieval
Advanced Retrieval
Plot Cart
Computations
Update Plot
Reset Plot
Remove All Datasets
Remove Some
6.0E-6 ≤ E_n (eV) ≤ 2.3851E8 Log
1.3913E-10 ≤ σ (b) ≤ 119.21 Log
plot width: 600 and height: 500 New
Legends in plot None New
8-O-16(n,total) ENDF/B-VII.1
8-O-16(n,elastic) ENDF/B-VII.1
8-O-16(n,p) ENDF/B-VII.1
8-O-16(n,α) ENDF/B-VII.1
View evaluated data
Add your data
Help
Cross Section (b)
E+2 E+1 E+0 E-1 E-2 E-3 E-4 E-5 E-6 E-7 E-8 E-9
E-5 E-4 E-3 E-2 E-1 E+0 E+1 E+2 E+3 E+4 E+5 E+6 E+7 E+8
Incident Energy (eV)

Appendix B

Derivation of the relative statistical uncertainties for the frequency mean lineal energy, Dose mean lineal energy, and dose rate

In the measurement scenario considered, the radiation environment includes background radiation, as observed in the CERF measurements at 900 V conducted in this study. Both the background radiation and the pure radiation measurements were obtained using the Cy-TEPC and the Cy-GPC detectors. To determine the pure radiation measurements, the background radiation was subtracted from the counters' measured spectrum. Therefore, in the final spectra for every lineal energy (y_i): $f(y_i) = f_c(y_i) - f_b(y_i)$.

For the statistical error calculation, the uncertainties of both components should be considered. For this purpose, the following error propagation formula has been used:

$$if\ Q = a + b + \cdots + -(x + y + \cdots z) \rightarrow \delta Q = \sqrt{(\delta a)^2 + (\delta b)^2 + \cdots + (\delta z)^2}$$

Therefore, for $\dot{D} = \frac{1}{m}\sum y_i \dot{f}(y_i) = \frac{1}{m}\sum y_i\left(\dot{f}_c(y_i) - \dot{f}_b(y_i)\right)$, the statistical error would be:

$$\delta\dot{D} = \frac{1}{m}\sqrt{\sum\left(y_i\delta\dot{f}_c(y_i)\right)^2 + \sum\left(y_i\delta\dot{f}_b(y_i)\right)^2}$$

and since $\delta\dot{f}_c(y_i) = \sqrt{\dot{f}_c(y_i)}$ and $\delta\dot{f}_b(y_i) = \sqrt{\dot{f}_b(y_i)}$,

$$\delta\dot{D} = \frac{1}{m}\sqrt{\sum {y_i}^2\dot{f}_c(y_i) + \sum {y_i}^2\dot{f}_b(y_i)}$$

And, the relative error would be:

$$\frac{\delta \dot{D}}{\dot{D}} = \frac{\sqrt{\sum {y_i}^2 \dot{f}_c(y_i) + \sum {y_i}^2 \dot{f}_b(y_i)}}{\sum y_i\left(\dot{f}_c(y_i)\right) - \sum y_i\left(\dot{f}_b(y_i)\right)} = \frac{\sqrt{G}}{B}$$

For

$$\bar{y}_f = \frac{\sum y_i f(y_i)}{\sum f(y_i)} = \frac{\sum y_i\left(f_c(y_i) - f_b(y_i)\right)}{\sum f_c(y_i) - f_b(y_i)}$$

$$\frac{\delta \bar{y}_f}{\bar{y}_f} = \sqrt{\left(\frac{\delta(\sum y_i f(y_i))}{\sum y_i f(y_i)}\right)^2 + \left(\frac{\delta(\sum f(y_i))}{\sum f(y_i)}\right)^2}$$

$$= \sqrt{\left(\frac{\delta\left(\sum y_i\left(f_c(y_i) - f_b(y_i)\right)\right)}{\sum y_i\left(f_c(y_i) - f_b(y_i)\right)}\right)^2 + \left(\frac{\delta(\sum f_c(y_i) - f_b(y_i))}{\sum f_c(y_i) - f_b(y_i)}\right)^2}$$

$$= \sqrt{\left(\frac{\sqrt{\sum\left\{\left(\delta y_i f_c(y_i)\right)^2 + \left(\delta y_i f_b(y_i)\right)^2\right\}}}{\sum y_i\left(f_c(y_i) - f_b(y_i)\right)}\right)^2 + \left(\frac{\sqrt{\sum\left\{\left(\delta f_c(y_i)\right)^2 + \left(\delta f_b(y_i)\right)^2\right\}}}{\sum f_c(y_i) - f_b(y_i)}\right)^2}$$

$$= \sqrt{\left(\frac{\sqrt{\sum {y_i}^2 f_c(y_i) + \sum {y_i}^2 f_b(y_i)}}{\sum y_i\left(f_c(y_i) - f_b(y_i)\right)}\right)^2 + \left(\frac{\sqrt{\sum f_c(y_i) + f_b(y_i)}}{\sum f_c(y_i) - f_b(y_i)}\right)^2} =$$

$$\sqrt{\frac{\sum {y_i}^2 (f_c(y_i) + f_b(y_i))}{(\sum y_i (f_c(y_i) - f_b(y_i)))^2} + \frac{\sum f_c(y_i) + f_b(y_i)}{(\sum f_c(y_i) - f_b(y_i))^2}} = \sqrt{\frac{A}{B^2} + \frac{C}{D^2}}$$

For $\bar{y}_d = \frac{\sum y_i d(y_i)}{\sum d(y_i)} = \frac{\sum {y_i}^2 f(y_i)}{\sum y_i f(y_i)} = \frac{\sum {y_i}^2 (f_c(y_i) - f_b(y_i))}{\sum y_i (f_c(y_i) - f_b(y_i))}$

$$\frac{\delta \bar{y}_d}{\bar{y}_d} = \sqrt{\left(\frac{\delta(\sum {y_i}^2 f(y_i))}{\sum {y_i}^2 f(y_i)}\right)^2 + \left(\frac{\delta(\sum y_i f(y_i))}{\sum y_i f(y_i)}\right)^2} =$$

$$\sqrt{\left(\frac{\delta(\sum {y_i}^2 (f_c(y_i) - f_b(y_i)))}{\sum {y_i}^2 (f_c(y_i) - f_b(y_i))}\right)^2 + \left(\frac{\delta(\sum y_i (f_c(y_i) - f_b(y_i)))}{\sum y_i (f_c(y_i) - f_b(y_i))}\right)^2} =$$

$$\sqrt{\left(\frac{\sqrt{\sum\left\{(\delta {y_i}^2 f_c(y_i))^2 + (\delta {y_i}^2 f_b(y_i))^2\right\}}}{\sum {y_i}^2 (f_c(y_i) - f_b(y_i))}\right)^2 + \left(\frac{\sqrt{\sum\left\{(\delta y_i f_c(y_i))^2 + (\delta y_i f_b(y_i))^2\right\}}}{\sum y_i \{f_c(y_i) - f_b(y_i)\}}\right)^2}$$

$$= \sqrt{\left(\frac{\sqrt{\sum {y_i}^4 f_c(y_i) + \sum {y_i}^4 f_b(y_i)}}{\sum {y_i}^2 (f_c(y_i) - f_b(y_i))}\right)^2 + \left(\frac{\sqrt{\sum {y_i}^2 \{f_c(y_i) + f_b(y_i)\}}}{\sum y_i \{f_c(y_i) - f_b(y_i)\}}\right)^2}$$

$$= \sqrt{\frac{\sum {y_i}^4 (f_c(y_i) + f_b(y_i))}{(\sum {y_i}^2 (f_c(y_i) - f_b(y_i)))^2} + \frac{\sum {y_i}^2 (f_c(y_i) + f_b(y_i))}{\left(\sum y_i (f_c(y_i) - f_b(y_i))\right)^2}}$$

$$= \sqrt{\frac{E}{F^2} + \frac{A}{B^2}}$$

Appendix C

An example of mixed-radiation field measurement data analysis

An example of MATLAB codes used for analyzing measurement results from Cy-TEPC and Cy-GPC, to obtain spectra and values of neutron dose rate and dose equivalent rate.

```
%=========================================================================
% Name: Faezeh Forouzan
% Purposes of the Code:
% 1. Redistribution of the linear MCA pulse height data, produced by the
% mixed radiation field of 2.5 MeV neutrons and 0.662 MeV gamma rays
% measured by the Cy-TEPC and Cy-GPC, into an equal logarithmic interval
% basis (50 log bins per decade),
% 2. Calculate and plot the dose rate spectra
% 3. Subtraction of Cy-GPC measured spectrum from the Cy-TEPC data to
% obtain the neutron dose rate spectrum.
% 4. Calculate and plot the dose equivalent spectrum.
%=========================================================================
%-------------------------------------------------------------------------
% Step (1) Generating input Pulse Height Spectrum measured bt the Cy-TEPC
%-------------------------------------------------------------------------
clc;clear; close all


% Cy-TEPC Charachterisation
format long
LTAmp_TEPC = 11310.2590; % Cy-TEPC measurement LIVE TIME
remca_TEPC = csvread('DPP8192_TEPC_G10_4m_P385_30cm_3hrs_11Aprl2017.csv');
% Cy-TEPC input pulse height distribution
AlphaEnergy_TEPC = 161.8; % Energy of alpha particles of calibration source
AlphaPeak_TEPC  = 938; % Alpha peak position channel number on the MCA
TesterAmpGain_TEPC = 1; % Gain of amplifier when measuring the alpha peak
Cf_testerAmp_TEPC = AlphaEnergy_TEPC/AlphaPeak_TEPC % Calibration fector
% of the amplifier when measuring the alpha peak

AmpGain_TEPC = 6; % Gain of amplifier when making the measurements with
% Cy-TEPC

cf_TEPC= Cf_testerAmp_TEPC/(AmpGain_TEPC/TesterAmpGain_TEPC) % Calibration
% factor of amplifier when making the measurements with Cy-TEPC
DE_TEPC = 0; % Initial value of deposited Energy in Cy-TEPC
DE_TEPC10 =0; % Initial value of deposited Energy in Cy-TEPC, y>10 keV/um
H_DE_TEPC = 0; % Initial value of deposited Energy in Cy-TEPC, for
% calculationg the dose equivalent

H_DE_TEPC10 =0;  % Initial value of deposited Energy in Cy-TEPC, for
% calculationg the dose equivalent, y>10 keV/um
%-------------------------------------------------------------------------
```

```
%physical charcrteristics of counter
P_TEPC = 55; % Gas pressure inside the counter
density_TEPC = 1.798*(P_TEPC/750.061683); % Density of the gas
d_TEPC = 1.5 * 10^(-2); % diameter of the sensitive volume
h_TEPC = 1.5 * 10^(-2); % Height of the sensitive volume
Volume_TEPC = h_TEPC*pi*(d_TEPC/2)^2; % Volume of the sensitive volume
mass_TEPC = density_TEPC * Volume_TEPC; % Mass of gas inside the counter

%------------------------------------------------------------------------
% Step (2) % Executing the redistribution of linear Pulse Height data
% and calculating the Deposited energy, Deposited dose-rate, and
% Deposited dose-equivalent rate spectra and valuse measured by the Cy-TEPC.
% And, Also the values of ybarF, ybarD and their relative uncertaintiess.
%------------------------------------------------------------------------
% Initial conitions
remca_TEPC';
exremca_TEPC = remca_TEPC'; % Input matrix transpose
Lowest_Channel_TEPC = 348; % Lowest channel of MCA in TEPC measurements
lc_TEPC= Lowest_Channel_TEPC; % Initial value of the lowest channel number
% of each bin

Uppermost_Channel_TEPC = 8192; % Uppermost channel of MCA
uc_TEPC = Uppermost_Channel_TEPC; % Initial value of the highest channel
% number of each bin

starty_TEPC = (lc_TEPC * cf_TEPC); % Start (lowest) value of lineal energy
endy_TEPC = (cf_TEPC * uc_TEPC); % End (highest) value of lineal energy
start_log_chn_TEPC = (log10(starty_TEPC)*50+100);
% First logarithmic bin value corresponding to the lowest lineal energy

end_log_chn_TEPC = (log10 (endy_TEPC)*50 +100);
% Last logarithmic bin value corresponding to the highest lineal energy

startlogchn_TEPC = round(start_log_chn_TEPC);
% First logarithmic bin number corresponding to the lowest lineal energy

endlogchn_TEPC = round(end_log_chn_TEPC);
% Last logarithmic bin number corresponding to the highest lineal energy
factor = 10^(1/50); % Width of equal logarithmic bins

logchncount_TEPC = startlogchn_TEPC;
% Initial value of the logarithmic bins counter

startlinchn_TEPC = (starty_TEPC/cf_TEPC);
% Initial value of linear channels

endivy_TEPC = (starty_TEPC*factor);
% End value of the logarithmic bins counter

endlinchn_TEPC = (endivy_TEPC/cf_TEPC);
% End value of linear channels
```

```
istartlinchn_TEPC = round(startlinchn_TEPC)
% Initial value of the linear channels counter

iendlinchn_TEPC = round(endlinchn_TEPC);
% End value of the linear channels counter

Ch10_TEPC= 10/cf_TEPC;
% Linear channel coresponding to y=10 keV/um

Ch100_TEPC = 100/cf_TEPC;
% Linear channel coresponding to y=100 keV/um

% The loop below, calculates the deposited energy distribution (d(y))values
% to be used for obtaining the dose rate and dose-equivalent rate spectra
while(logchncount_TEPC <= endlogchn_TEPC)
    summation_TEPC = 0;
    % Sum of d(y) in each logarithmic bin

    summation_TEPC10 = 0;
    % Sum of d(y) in each log bin, y > 10 keV/um

    H_summation_TEPC = 0;
    % Sum of d(y) in each log bin multiplied by corresponding Q values

    H_SUM_TEPC = 0;
    while (istartlinchn_TEPC<=iendlinchn_TEPC);
          summation_TEPC = summation_TEPC +...
          exremca_TEPC(round(istartlinchn_TEPC))*istartlinchn_TEPC*cf_TEPC;

      % The subloop below, calculates the value of Q at each data point
          if (Ch10_TEPC >= istartlinchn_TEPC)
           Q = 1;
            % Q values for y<10 keV/um;

        elseif (istartlinchn_TEPC >= Ch10_TEPC) & ...
                (istartlinchn_TEPC <= Ch100_TEPC)
          Q = 0.32*istartlinchn_TEPC*cf_TEPC-2.2;
         % Q values for 10<y<100 keV/um;

        elseif (istartlinchn_TEPC >= Ch100_TEPC)
          Q = 300/sqrt(istartlinchn_TEPC*cf_TEPC);
         % Q values for y>100 keV/um;
         else
           Q = 0;
         end
            H_summation_TEPC = Q* summation_TEPC;
            H_SUM_TEPC = H_SUM_TEPC + H_summation_TEPC;

        % The subloop below, calculates the dose-equivalent distribution
                    if (istartlinchn_TEPC >= lc_TEPC)
                        summation_TEPC10 =summation_TEPC;
                        Q = 0.32*istartlinchn_TEPC*cf_TEPC-2.2;
```

```
                        H_summation_TEPC10 = Q*summation_TEPC;
                          else
                         summation_TEPC10 = 0;
                         H_summation_TEPC10 = 0;
                    end

            istartlinchn_TEPC = (istartlinchn_TEPC +1)
    end

    DE_TEPC = DE_TEPC + summation_TEPC;
    % Deposited Energy (keV/um) data poitns in Cy-TEPC

    H_DE_TEPC = H_DE_TEPC + H_summation_TEPC;
    % Deposited Energy data poitns in Cy-TEPC, multiplied by Q values

    DE_TEPC10 = DE_TEPC10 + summation_TEPC10;
    % Deposited Energy data poitns in Cy-TEPC, y > 10 keV/um

    H_DE_TEPC10 = H_DE_TEPC10 + H_summation_TEPC10;
    % Deposited Energy data poitns in Cy-TEPC, multiplied by Q values,
    % y > 10 keV/um

    dose_TEPC = (summation_TEPC * (4/3)*1.602*10^(-10))/mass_TEPC;
    % Dose distribution data poitns (uJ/kg, uGy) in each logarithmic bin

    D_eqlogplot_TEPC(logchncount_TEPC) = dose_TEPC/(LTAmp_TEPC/3600);
    % Dose-rate distribution data poitns (uGy/hr) in each logarithmic bin

    H_TEPC = (H_summation_TEPC* (4/3)*1.602*10^(-10))/mass_TEPC;
    %Dose-equivalent distribution data poitns (uSv) in each logarithmic bin

    H_eqlogplot_TEPC(logchncount_TEPC) = H_TEPC/(LTAmp_TEPC/3600);
    % Dose-equivalent-rate distribution data poitns (uSv/hr) in each
    % logarithmic bin

    logchncount_TEPC = (logchncount_TEPC +1);
    istartlinchn_TEPC = iendlinchn_TEPC;
    iendlinchn_TEPC = istartlinchn_TEPC *factor;

    if iendlinchn_TEPC > Uppermost_Channel_TEPC;
        iendlinchn_TEPC = Uppermost_Channel_TEPC;
    end
end

DepositedEnergy_TEPC = DE_TEPC
H_DepositedEnergy_TEPC = H_DE_TEPC

%-------------------------------------------------------------------------
% The loop below calculaes the Total dose-rate, Total dose-equivalent-rate,
% Fequency mean lineal energy (YbarF), Dose mean lineal energy (YbarD),
% and the coresponding relative errors measured by Cy-TEPC
%-------------------------------------------------------------------------
```

```
% Initial values of the parameters for calculation of YbarF and YbarD

sigmady_TEPC = 0;
sigmafy_TEPC = 0;
sigmayfy_TEPC = 0;
sigmaydy_TEPC = 0;
sigmay2fy_TEPC = 0;
sigmay4fy_TEPC = 0;
sigmayfy_TEPC10 = 0;
sigmay2fy_TEPC10 = 0;

while(lc_TEPC <= uc_TEPC);
        y = lc_TEPC*cf_TEPC;
        fy = exremca_TEPC (lc_TEPC);
        dy = fy*y;
        sigmady_TEPC = sigmady_TEPC + dy;
        sigmafy_TEPC = sigmafy_TEPC + fy;
        sigmayfy_TEPC = sigmayfy_TEPC + y*fy;
        sigmaydy_TEPC = sigmaydy_TEPC + dy*y;
        sigmay2fy_TEPC = sigmay2fy_TEPC + y^2*fy;
        sigmay4fy_TEPC = sigmay4fy_TEPC + y^4*fy;
        if (lc_TEPC >= Lowest_Channel_TEPC)
            sigmayfy_TEPC10 = sigmayfy_TEPC10 + y*fy;
            sigmay2fy_TEPC10 = sigmay2fy_TEPC10 + y^2*fy;
        else
             summation_TEPC10 = 0;
        end
        lc_TEPC = lc_TEPC +1;
end
%-------------------------------------------------------------------------
% The following parameters are the terms in calculation of Total Dose-rate,
% Total Dose-Equivalent-Rate, Fequency mean lineal energy (YbarF),
% Dose mean lineal energy (YbarD), and the coresponding relative errors
%-------------------------------------------------------------------------
sigmayfy_TEPC = sigmayfy_TEPC;
sigmafy_TEPC = sigmafy_TEPC;
sigmaydy_TEPC =sigmaydy_TEPC;
sigmady_TEPC = sigmady_TEPC;
sigmay2fy_TEPC = sigmay2fy_TEPC;
sigmay4fy_TEPC = sigmay4fy_TEPC;

Dose_TEgas_TEPC = (DE_TEPC *(4/3)*1.602*10^(-10))/mass_TEPC;
% Deposited Dose value (uGy) measured by Cy-TEPC

Doserate_TEPC = (Dose_TEgas_TEPC/(LTAmp_TEPC/3600));
% Dose-Rate value (uGy/hr) measured by Cy-TEPC

Dose_EQV_TEPC = (H_DE_TEPC *(4/3)*1.602*10^(-10))/mass_TEPC;
% Deposited Dose-Equivalent value (uSv) measured by Cy-TEPC

Dose_EQV_rate_TEPC = (Dose_EQV_TEPC/(LTAmp_TEPC/3600));
% Deposited Dose-Equivalent-Rate value (uSv/hr) measured by Cy-TEPC
```

```
YbarF_TEPC = sigmayfy_TEPC/sigmafy_TEPC;
% YbarF value measured by TEPC

YbarD_TEPC = sigmaydy_TEPC/sigmady_TEPC;
ErrDoseRate_TEPC = sqrt(sigmay2fy_TEPC)/sigmayfy_TEPC;
% Relative error of Dose-Rate
% YbarD value measured by TEPC

ErrYbarF_TEPC = sqrt((sigmay2fy_TEPC)/(sigmayfy_TEPC)^2+1/sigmafy_TEPC);
% Relative error of YbarF

ErrYbarD_TEPC = sqrt((sigmay4fy_TEPC)/(sigmay2fy_TEPC)^2+...
    (sigmay2fy_TEPC)/(sigmayfy_TEPC)^2);
% Relative error of YbarD

sigmayfy_TEPC10 = sigmayfy_TEPC10;
sigmay2fy_TEPC10 = sigmay2fy_TEPC10;

Dose_TEgas_TEPC10 = (DE_TEPC10 *(4/3)*1.602*10^(-10))/mass_TEPC;
% Deposited Dose value (uGy) measured by Cy-TEPC, y>10 keV/um

Doserate_TEPC10 = (Dose_TEgas_TEPC10/(LTAmp_TEPC/3600));
% Dose-Rate value (uGy/hr) measured by Cy-TEPC, y>10 keV/um

ErrDoseRate_TEPC10 = sqrt(sigmay2fy_TEPC10)/sigmayfy_TEPC10;
% Relative error of Dose-Rate, y>10 keV/um

Dose_Equivalent_TEgas_TEPC10 =(H_DE_TEPC10*(4/3)*1.602*10^(-10))/mass_TEPC;
% Deposited Dose-Equivalent value (uSv) measured by Cy-TEPC, y>10 keV/um

Dose_Equivalent_rate_TEPC10 = (Dose_Equivalent_TEgas_TEPC10/...
    (LTAmp_TEPC/3600));
% Deposited Dose-Equivalent-Rate value (uSv) measured by Cy-TEPC,
% y>10 keV/um

%--------------------------------------------------------------------------
% Step (3) Generating input Pulse Height Spectrum measured bt the Cy-GPC
%--------------------------------------------------------------------------
format long
% Cy-GPC Charachterisation
LTAmp_GPC = 11354.055; % Cy-GPC measurement LIVE TIME
remca_GPC = ...
    csvread('DPP8192_GPC_G10_4m_P385_30cm_3hrs_11Aprl2017_MOD_CH72.csv');
% Cy-GPC input pulse height distribution

AlphaEnergy_GPC = 157.7; % Energy of alpha particles of calibration source
AlphaPeak_GPC  = 5564; % Alpha peak position channel number on the MCA
TesterAmpGain_GPC = 0.75; % Gain of amplifier when measuring the alpha peak
Cf_testerAmp_GPC = AlphaEnergy_GPC/AlphaPeak_GPC % Calibration fector
% of the amplifier when measuring the alpha peak
```

```
AmpGain_GPC = 10; % Gain of amplifier when making the measurements with
% Cy-GPC

cf_GPC= Cf_testerAmp_GPC/(AmpGain_GPC/TesterAmpGain_GPC) % Calibration
% factor of amplifier when making the measurements with Cy-GPC

DE_GPC = 0; % Initial value of deposited Energy in Cy-GPC
DE_GPC10 =0; % Initial value of deposited Energy in Cy-GPC, y>10 keV/um
H_DE_GPC = 0; % Initial value of deposited Energy in Cy-GPC, for
% calculationg the dose equivalent

H_DE_GPC10 =0;  % Initial value of deposited Energy in Cy-GPC, for
% calculationg the dose equivalent, y>10 keV/um
%-------------------------------------------------------------------------
%physical charcrteristics of counter
P_GPC = 55.6; % Gas pressure inside the counter
density_GPC = 1.798*(P_GPC/750.061683); % Density of the gas
d_GPC = 1.5 * 10^(-2); % diameter of the sensitive volume
h_GPC = 1.5 * 10^(-2); % Height of the sensitive volume
Volume_GPC = h_GPC*pi*(d_GPC/2)^2; % Volume of the sensitive volume
mass_GPC = density_GPC * Volume_GPC; % Mass of gas inside the counter

%-------------------------------------------------------------------------
% Step (4) % Executing the redistribution of linear Pulse Height data
% and calculating the Deposited energy, Deposited dose-rate, and
% Deposited dose-equivalent rate spectra and valuse measured by the Cy-GPC.
% And, Also the values of ybarF, ybarD and their relative errors.
%-------------------------------------------------------------------------
% Initial conitions
remca_GPC';
exremca_GPC = remca_GPC'; % Input matrix transpose
Lowest_Channel_GPC = 15; % Lowest channel of MCA in GPC measurements
lc_GPC= Lowest_Channel_GPC;% Initial value of the lower chanel of each bin
Uppermost_Channel_GPC = 8192; % Uppermost channel of MCA
uc_GPC = Uppermost_Channel_GPC;
starty_GPC = (lc_GPC * cf_GPC); % Start (lowest) value of lineal energy
endy_GPC = (cf_GPC * uc_GPC); % End (highest) value of lineal energy
start_log_chn_GPC = (log10(starty_GPC)*50+100);
% First logarithmic bin value corresponding to the lowest lineal energy

end_log_chn_GPC = (log10 (endy_GPC)*50 +100);
% Last logarithmic bin value corresponding to the highest lineal energy

startlogchn_GPC = round(start_log_chn_GPC);
% First logarithmic bin number corresponding to the lowest lineal energy

endlogchn_GPC = round(end_log_chn_GPC);
% Last logarithmic bin number corresponding to the highest lineal energy

factor = 10^(1/50); % Width of equal logarithmic bins
logchncount_GPC = startlogchn_GPC;
% Initial value of the logarithmic bins counter
```

```
startlinchn_GPC = (starty_GPC/cf_GPC);
% Initial value of linear channels

endivy_GPC = (starty_GPC*factor);
% End value of the logarithmic bins counter

endlinchn_GPC = (endivy_GPC/cf_GPC);
% End value of linear channels

istartlinchn_GPC = round(startlinchn_GPC)
% Initial value of the linear channels counter

iendlinchn_GPC = round(endlinchn_GPC);
% End value of the linear channels counter

Ch10_GPC= 10/cf_GPC;
% Linear channel coresponding to y=10 keV/um

Ch100_GPC = 100/cf_GPC;
% Linear channel coresponding to y=100 keV/um

% The loop below, calculates the deposited energy distribution (d(y))values
% to be used for obtaining the dose rate and dose-equivalent rate spectra
% measured by Cy-GPC
while(logchncount_GPC <= endlogchn_GPC)
    summation_GPC = 0;
    % Sum of d(y) in each logarithmic bin

    summation_GPC10 = 0;
    % Sum of d(y) in each log bin, y > 10 keV/um

    H_summation_GPC = 0;
    % Sum of d(y) in each log bin multiplied by corresponding Q values

    H_SUM_GPC = 0;
    while (istartlinchn_GPC<=iendlinchn_GPC);
          summation_GPC = summation_GPC +
exremca_GPC(round(istartlinchn_GPC))*istartlinchn_GPC*cf_GPC;

          % The subloop below, calculates the value of Q at each data point
          if (Ch10_GPC >= istartlinchn_GPC)
           Q = 1;
           % Q value for y<10 keV/um

        elseif (istartlinchn_GPC >= Ch10_GPC) & ...
               (istartlinchn_GPC <= Ch100_GPC)
           Q = 0.32*istartlinchn_GPC*cf_GPC-2.2;
         % Q value for 10<y<100 keV/um

        elseif (istartlinchn_GPC >= Ch100_GPC)
           Q = 300/sqrt(istartlinchn_GPC*cf_GPC);
```

```
      % Q value for y >100 keV/um
      else
        Q = 0;

      end
         H_summation_GPC = Q* summation_GPC;
         H_SUM_GPC = H_SUM_GPC + H_summation_GPC;

     % The subloop below, calculates the dose-equivalent distribution
                 if (istartlinchn_GPC >= lc_GPC)
                     summation_GPC10 =summation_GPC;
                     Q = 0.32*istartlinchn_GPC*cf_GPC-2.2;
                     H_summation_GPC10 = Q*summation_GPC;
                       else
                      summation_GPC10 = 0;
                      H_summation_GPC10 = 0;
                  end

         istartlinchn_GPC = (istartlinchn_GPC +1)
end

DE_GPC = DE_GPC + summation_GPC;
% Deposited Energy (keV/um) data poitns in Cy-GPC

H_DE_GPC = H_DE_GPC + H_summation_GPC;
% Deposited Energy data poitns in Cy-GPC, multiplied by Q values

DE_GPC10 = DE_GPC10 + summation_GPC10;
% Deposited Energy data poitns in Cy-GPC, y > 10 keV/um

H_DE_GPC10 = H_DE_GPC10 + H_summation_GPC10;
% Deposited Energy data poitns in Cy-GPC, multiplied by Q values,
% y > 10 keV/um

dose_GPC = (summation_GPC * (4/3)*1.602*10^(-10))/mass_GPC;
% Dose distribution data poitns (uJ/kg, uGy) in each logarithmic bin

D_eqlogplot_GPC(logchncount_GPC) = dose_GPC/(LTAmp_GPC/3600);
% Dose-rate distribution data poitns (uGy/hr) in each logarithmic bin

H_GPC = (H_summation_GPC* (4/3)*1.602*10^(-10))/mass_GPC;
%Dose-equivalent distribution data poitns (uSv) in each logarithmic bin

H_eqlogplot_GPC(logchncount_GPC) = H_GPC/(LTAmp_GPC/3600);
% Dose-equivalent-rate distribution data poitns (uSv/hr) in each
% logarithmic bin

logchncount_GPC = (logchncount_GPC +1);
istartlinchn_GPC = iendlinchn_GPC;
iendlinchn_GPC = istartlinchn_GPC *factor;

if iendlinchn_GPC > Uppermost_Channel_GPC;
```

```
        iendlinchn_GPC = Uppermost_Channel_GPC;
    end
end

DepositedEnergy_GPC = DE_GPC
H_DepositedEnergy_GPC = H_DE_GPC

%-------------------------------------------------------------------------
% The loop below calculaes the Total dose-rate,
% Total dose-equivalent-rate, Fequency mean lineal energy (YbarF),
% Dose mean lineal energy (YbarD), and the coresponding relative errors
% measured by Cy-GPC
%-------------------------------------------------------------------------
% Initial values of the parameters for calculation of YbarF and YbarD
sigmady_GPC = 0;
sigmafy_GPC = 0;
sigmayfy_GPC = 0;
sigmaydy_GPC = 0;
sigmay2fy_GPC = 0;
sigmay4fy_GPC = 0;
sigmayfy_GPC10 = 0;
sigmay2fy_GPC10 = 0;

while(lc_GPC <= uc_GPC);
        y = lc_GPC*cf_GPC;
        fy = exremca_GPC (lc_GPC);
        dy = fy*y;
        sigmady_GPC = sigmady_GPC + dy;
        sigmafy_GPC = sigmafy_GPC + fy;
        sigmayfy_GPC = sigmayfy_GPC + y*fy;
        sigmaydy_GPC = sigmaydy_GPC + dy*y;
        sigmay2fy_GPC = sigmay2fy_GPC + y^2*fy;
        sigmay4fy_GPC = sigmay4fy_GPC + y^4*fy;
        if (lc_GPC >= Lowest_Channel_GPC)
            sigmayfy_GPC10 = sigmayfy_GPC10 + y*fy;
            sigmay2fy_GPC10 = sigmay2fy_GPC10 + y^2*fy;
        else
             summation_GPC10 = 0;
        end
        lc_GPC = lc_GPC +1;
end

sigmayfy_GPC = sigmayfy_GPC;
sigmafy_GPC = sigmafy_GPC;
sigmaydy_GPC =sigmaydy_GPC;
sigmady_GPC = sigmady_GPC;
sigmay2fy_GPC = sigmay2fy_GPC;
sigmay4fy_GPC = sigmay4fy_GPC;

Dose_TEgas_GPC = (DE_GPC *(4/3)*1.602*10^(-10))/mass_GPC;
% Deposited Dose value (uGy) measured by Cy-GPC
```

```
Doserate_GPC = (Dose_TEgas_GPC/(LTAmp_GPC/3600));
% Dose-Rate value (uGy/hr) measured by Cy-GPC

Dose_EQV_GPC = (H_DE_GPC *(4/3)*1.602*10^(-10))/mass_GPC;
% Deposited Dose-Equivalent value (uSv) measured by Cy-GPC

Dose_EQV_rate_GPC = (Dose_EQV_GPC/(LTAmp_GPC/3600));
% Deposited Dose-Equivalent-Rate value (uSv/hr) measured by Cy-GPC

YbarF_GPC = sigmayfy_GPC/sigmafy_GPC;
% YbarF value measured by GPC

YbarD_GPC = sigmaydy_GPC/sigmady_GPC;
% YbarD value measured by GPC

ErrDoseRate_GPC = sqrt(sigmay2fy_GPC)/sigmayfy_GPC;
% Relative error of Dose-Rate measured by GPC

ErrYbarF_GPC = sqrt((sigmay2fy_GPC)/(sigmayfy_GPC)^2+1/sigmafy_GPC);
% Relative error of YbarF measured by GPC

ErrYbarD_GPC = sqrt((sigmay4fy_GPC)/(sigmay2fy_GPC)^2+...
    (sigmay2fy_GPC)/(sigmayfy_GPC)^2);
% Relative error of YbarD measured by GPC

sigmayfy_GPC10 = sigmayfy_GPC10;
sigmay2fy_GPC10 = sigmay2fy_GPC10;

Dose_TEgas_GPC10 = (DE_GPC10 *(4/3)*1.602*10^(-10))/mass_GPC;
% Deposited Dose value (uGy) measured by Cy-GPC, y>10 keV/um

Doserate_GPC10 = (Dose_TEgas_GPC10/(LTAmp_GPC/3600));
% Dose-Rate value (uGy/hr) measured by Cy-GPC, y>10 keV/um

ErrDoseRate_GPC10 = sqrt(sigmay2fy_GPC10)/sigmayfy_GPC10;
% Relative error of Dose-Rate, y>10 keV/um

Dose_Equivalent_TEgas_GPC10 =(H_DE_GPC10*(4/3)*1.602*10^(-10))/mass_GPC;
% Deposited Dose-Equivalent value (uSv) measured by Cy-GPC, y>10 keV/um

Dose_Equivalent_rate_GPC10 = (Dose_Equivalent_TEgas_GPC10/...
    (LTAmp_GPC/3600));
% Deposited Dose-Equivalent-Rate value(uSv) measured by Cy-GPC, y>10 keV/um

%-------------------------------------------------------------------------
% Step (5) Obtaining the pure neutron spectrum by subtracting the Cy-GPC
% measured spectrum from the Cy-TEPC measured spectum and plotting the
% dose-rate and dose-equivalent-rate spectra
%-------------------------------------------------------------------------
if 1 == 1;
fig1=figure(1);
```

```
% Generating the equal loarithmic bins on the lineal energy axis
x=50*log10(decade(0, 5, 1));
y=10.^((x-100)/50);

YYY=strread(num2str(y),'%s');
for tt=1:length(YYY)
    YY{tt}='';
end

for gg=1:9:length(YYY)
YY{gg}=YYY{gg};
end

h1=semilogx(10.^(([1:numel(D_eqlogplot_TEPC)]-100)./50),D_eqlogplot_TEPC,...
    'r:','LineWidth',4)
% Plot of the dose-rate spectrum, measured by Cy-TEPC
hold on
h2=semilogx(10.^(([1:numel(D_eqlogplot_GPC)]-100)./50),D_eqlogplot_GPC,...
    'b:','LineWidth',4)
% Plot of the dose-rate spectrum, measured by Cy-GPC

%--------------------------------------------------------------------------
% Obtaining the pure neutron spectrum
%--------------------------------------------------------------------------
[m,n] = size(D_eqlogplot_TEPC);
[a,b] = size(D_eqlogplot_GPC);
Dif= n-b;
Null_GPC= zeros(1,n);
Photon=0;
[e,f] = size(H_eqlogplot_TEPC);
[c,d] = size(H_eqlogplot_GPC);
Dif= f-d;
Null_H_GPC= zeros(1,f);
Photon_H =0;
i=1
while i < n
    if (150<=i)&(i<=b);
       Null_GPC(1,i)= D_eqlogplot_GPC(1,i);
       Null_H_GPC(1,i)= H_eqlogplot_GPC (1,i);
    else
        Null_GPC(1,i) =0;
        Null_H_GPC(1,i) =0;
    end
  Photon= Photon + Null_GPC(1,i);
  % Photon dose-rate spectrum data points, y > 10 keV/um

  Photon_H= Photon_H + Null_H_GPC(1,i);
  % Photon dose-equivalent-rate spectrum data points, y > 10 keV/um
  i=i+1
end

logint=0.046056;
```

```
Gamma = Null_GPC;
% Photon dose-rate spectrum

Mixed = D_eqlogplot_TEPC;
% Mixed-field dose-rate spectrum

Neutron = Mixed-Gamma;
% Neutron dose-rate spectrum

Norm_Neutron = Neutron./(logint*sum(Neutron));
% Normalized neutron dose-rate spectrum

H_Gamma = Null_H_GPC;
% Photon dose-equivalent-rate spectrum

H_Mixed = H_eqlogplot_TEPC;
% Mixed-field dose-equivalent-rate spectrum

H_Neutron = H_Mixed-H_Gamma;
% Neutron dose-equivalent-rate spectrum

H_Norm_Neutron = H_Neutron./(logint*sum(H_Neutron));
% Normalized neutron dose-equivalent-rate spectrum

%-------------------------------------------------------------------------
% Dose-rate and dose-equivalent-rate spectra plots specifications
%-------------------------------------------------------------------------
h3=semilogx(10.^([1:numel(Neutron)]-100)./50),Neutron,'k','LineWidth',2)
% Plot of the pure neutron dose-rate spectrum

h4=semilogx(10.^([1:numel(Norm_Neutron)]-100)./50),Norm_Neutron,'k:',...
    'LineWidth',2)
% Plot of the normalized pure neutron dose-rate spectrum

h5=semilogx(10.^([1:numel(H_eqlogplot_TEPC)]-100)./50),H_eqlogplot_TEPC,...
'b','LineWidth',2)
% Plot of the dose-equivalent-rate spectrum, measured by Cy-TEPC

h6=semilogx(10.^([1:numel(H_eqlogplot_GPC)]-100)./50),H_eqlogplot_GPC, ...
    'r','LineWidth',2)
% Plot of the dose-equivalent-rate spectrum, measured by Cy-GPC

h7=semilogx(10.^([1:numel(H_Neutron)]-100)./50),H_Neutron,'g',...
    'LineWidth',2)
% Plot of the pure neutron dose-equivalent-rate spectrum

title ('Dose-Rate and dose-equivalnt-rate Spectra')
xlabel ('$Lineal\:Energy\:[keV/\mu m]$','interpreter','latex')
ylabel ('$y.d(y).\dot{D}\:[\mu Gy/hr]$ $-$ $y.d(y).\dot{H}\:[\mu Sv/hr]$',...
    'interpreter','latex')
grid on
hold on
```

```
legend([h1,h2,h3,h4,h5, h6, h7],{'Mixed-field $$\dot{D}$$, Cy-TEPC',...
    'Photon $$\dot{D}$$, Cy-GPC','Obtained neutron $$\dot{D}$$', ...
    'Normalized neutron $$\dot{D}$$','Mixed-field $$\dot{H}$$, Cy-TEPC',...
    'Photon $$\dot{H}$$, Cy-GPC','Obtained neutron $$\dot{H}$$'},...
    'FontSize',8,'interpreter','latex')
 set(findall(fig1,'-property','FontSize'),'FontSize',14)
end
%--------------------------------------------------------------------------
% Noramlizing the pure neutron dose-rate spectrum
%--------------------------------------------------------------------------
fig2=figure(2);

logint=0.046056;
neqlogplot_TEPC = D_eqlogplot_TEPC./(logint*sum(D_eqlogplot_TEPC));
h8=semilogx(10.^(([1:numel(neqlogplot_TEPC)]-100)./50),...
        neqlogplot_TEPC,'b','LineWidth',4)
% Plot of the normalized dose-rate spectrum, measured by Cy-TEPC
hold on

neqlogplot_GPC = D_eqlogplot_GPC./(logint*sum(D_eqlogplot_GPC));
h9=semilogx(10.^(([1:numel(neqlogplot_GPC)]-100)./50),neqlogplot_GPC,...
    'r','LineWidth',4)
% Plot of the normalized dose-rate spectrum, measured by Cy-TEG

x=50*log10(decade(0, 5, 1));
y=10.^((x-100)/50);
    title ('Fractional Dose Rate Spectrum')
    xlabel ('$Lineal\:Energy\:[keV/\mu m]$','interpreter','latex')
    ylabel('$y.d(y).\dot{D}$','interpreter','latex')
    grid on
    hold on
    set(findall(fig2,'-property','FontSize'),'FontSize',12)
hold on
```

Appendix D

An example of the PHITS input code for simulation of the counters in a mixed-radiation field (in this case at the RMTL)

```
[ T i t l e ]
Irradiation of 1.5 cm sensitive volume of the Cy-TEPC/Cy-GPC at RMTL radiation field (at a distance of 20 cm from the target surface)

[ P a r a m e t e r s ]
 icntl    = 0    $icntl=0, normal PHITS calculation $icntl=7, execute [t-gshow] tally (graphical output)
 rseed    = -1   $Initial random number of history,
                 $rseed < 0, to estimate the statistical uncertainty and calculate the standard deviation of each tally output
 maxcas   = 2000000000 $Number of source particles
 maxbch   = 1          $Number of batch
 file(6)  = Name_of_the_file.out       $Output file name
 file(7)  = c:/phits/data/xsdir.jnd    $Cross section directory file name
 file(14) = c:/phits/data/trxcrd.dat   $γ decay data file name
 emin(1)  = 1.0E-3     $Minimum PROTON transport kinetic energy
 emin(2)  = 1.0E-10    $Minimum NEUTRON transport kinetic energy
 dmax(2)  = 3.0E3      $Maximum NEUTRON kinetic energy to use data library
 emin(12) = 1.0E-3     $Minimum ELECTRON transport kinetic energy
 dmax(12) = 1.0E3      $Maximum ELECTRON kinetic energy to use data library
 emin(13) = 1.0E-3     $Minimum POSITRON transport kinetic energy
 dmax(13) = 1.0E3      $Maximum POSITRON kinetic energy to use data library
 emin(14) = 1.0E-3     $Minimum PHOTON transport energy
 dmax(14) = 1.0E3      $Maximum PHOTON energy to use data library
 emin(18) = 1.0E-3     $Minimum ALPHA transport kinetic energy
 emin(19) = 1.0E-3     $Minimum NUCLEUS transport kinetic energy
 nedisp   = 1          $Landau Vavilov energy straggling for charged particle transport
 e-mode   = 1          $Event generator mode
$ deltb    = 1.e-5
```

$ deltm = 1.12345

$ igchk = 1

[S o u r c e]

s-type = 5 $Rectangular solid with energy distribution

$s-type = 2, monoenergetic radiation sources

proj = neutron $Projectile type

x0 = -2 $Minimum x coordinate (cm)

x1 = 2 $Maximum x coordinate (cm)

y0 = -2 $Minimum y coordinate (cm)

y1 = 2 $Maximum y coordinate (cm)

z0 = 20 $Minimum z coordinate (cm)

z1 = 20 $Maximum z coordinate (cm)

dir = -1 $Direction cosine from z axis

$ phi = 0

$ Neutron Energy Spectrum

e-type = 1 $Type of energy distribution, e-type=1:any energy distribution

ne = 65 $Number of energy groups $For monoenergetic radiation sources e0 = energy of radiation

$First column: energy of each bin $Second column: probabilities of the particle generation

1.86E-08 0

1.86E-08 0.000545798

2.71E-08 0.000806972

2.71E-08 0.00157818

4.18E-08 0.00158287

4.17E-08 0.00363943

6.26E-08 0.0039009

6.25E-08 0.00801402

9.90E-08 0.00801901

9.88E-08 0.0162453

1.48E-07	0.0162496
1.48E-07	0.028589
2.21E-07	0.0285934
2.21E-07	0.0409328
3.31E-07	0.0409372
5.24E-07	0.0414563
5.27E-07	0.025775
8.12E-07	0.0239802
8.16E-07	0.00829894
1.22E-06	0.00856041
1.94E-06	0.00907953
2.91E-06	0.00908393
4.36E-06	0.00960246
6.55E-06	0.00986393
1.09E-05	0.0103836
2.04E-05	0.0106475
3.70E-05	0.0106539
5.25E-05	0.0109148
7.07E-05	0.0116892
0.000131707	0.0114389
0.000238751	0.0119595
0.000522917	0.0129963
0.00105638	0.0130039
0.00272134	0.0140424
0.00535089	0.0140497
0.0120476	0.0132873
0.0294157	0.0127829
0.0465861	0.0127878
0.0758018	0.0127931
0.0993588	0.0122819
0.104915	0.0112542
0.157394	0.0115157
0.148952	0.014857

0.235878 0.0151191
0.241419 0.0274587
0.352542 0.0274628
0.341197 0.0457145
0.555217 0.0454627
0.55107 0.0696273
0.804723 0.0696314
0.844383 0.0889123
1.23315 0.0886593
1.23128 0.0935436
1.94953 0.0943198
2.06891 0.0770967
3.10429 0.076844
3.04614 0.0506226
4.57058 0.0503699
4.48962 0.0208066
7.11028 0.0208115
6.58866 0.00487231
10.7223 0.00436345
11.026 0.00153597
14.0646 0.00153861
15.6765 0.000511502
16

[M a t e r i a l]
MAT[1] $fill gas composition
1H -10.3
6000 -56.9
14N -3.5
16O -29.3
MAT[2] $Wall material composition $A-150 Shonka Plastic for TEPC $Carbon for GPC
1H -10.1

```
 6000        -77.6
 14N         -3.5
 16O         -5.2
 19F         -1.7
MAT[ 3 ]     $Counter parts composition PTFE C2F4
 6000        -33.33
 19F         -66.67
MAT[ 4 ]     $PMMA C5O2H8
 6000        -33.3
 16O         -13.3
 1H          -53.4

[ S u r f a c e ]   $Geometry definition and coordinates of the counter parts and surrounding area
c Box
1 BOX     -20.00     -20.00     -20.00      40.00       0.00       0.00
          0.00      40.00       0.00       0.00       0.00      40.00
c C
2 RCC 0.00 0.00 -2.00 0.00 0.00 4.00     1.25

c C10
3 RCC 0.00 0.00 1.00 0.00 0.00 1.10     0.15

c C11
4 RCC 0.00 0.00 -1.00 0.00 0.00 0.25     0.10

c C12
5 RCC 0.00 0.00 0.75 0.00 0.00 0.25     0.10

c C7
6 RCC 0.00 0.00 -2.20 0.00 0.00 0.10     0.75

c C8
7 RCC 0.00 0.00 2.10 0.00 0.00 0.10     0.75
```

c C9

8 RCC 0.00 0.00 -2.10 0.00 0.00 1.10 0.15

c PMME13

9 RCC 0.00 0.00 -2.60 0.00 0.00 0.40 0.75

c PMME14

10 RCC 0.00 0.00 2.20 0.00 0.00 0.40 0.75

c PMME15

11 RCC 0.00 0.00 -2.20 0.00 0.00 1.20 0.07

c PMME16

12 RCC 0.00 0.00 1.00 0.00 0.00 1.20 0.07

c PTFE3

13 RCC 0.00 0.00 -2.10 0.00 0.00 0.10 0.75

c PTFE4

14 RCC 0.00 0.00 2.00 0.00 0.00 0.10 0.75

c PTFE5

15 RCC 0.00 0.00 -2.00 0.00 0.00 0.50 0.25

c PTFE6

16 RCC 0.00 0.00 1.50 0.00 0.00 0.50 0.25

c TEgas1

17 RCC 0.00 0.00 -0.75 0.00 0.00 1.5 0.75

c Void17

18 RCC 0.00 0.00 -1.00 0.00 0.00 0.25 0.07

```
c Void18
19 RCC 0.00 0.00 0.75 0.00 0.00 0.25     0.07

c Void19
20 RCC 0.00 0.00 -2.30 0.00 0.00 1.20     0.04

c Void20
21 RCC 0.00 0.00 1.10 0.00 0.00 1.20     0.04

c Void21
22 RCC 0.00 0.00 -2.60 0.00 0.00 0.30     0.15

c Void22
23 RCC 0.00 0.00 2.30 0.00 0.00 0.30     0.15

c TEgas2
24 RCC 0.00 0.00 -1.5 0.00 0.00 0.75     0.75

c TEgas3
25 RCC 0.00 0.00 0.75 0.00 0.00 0.75     0.75

[ C e l l ]            $Cell definition in the counter parts
c Cell1A150Plastic
00001   2  -1.127        -2 +15 +16 +17 +24 +25
c Cell2TEGas_SensitiveVolume
00002   1  -1.318E-4     -17
c Cell3TEGas_LeftVolume
00003   1  -1.318E-4     -24 +8 +4
c Cell4TEGas_RightVolume
00004   1  -1.318E-4     -25 +3 +5
c Cell5PTFE
00005   3  -2.2         (-13 : -14 : -15 : -16 ) +8 +3
```

```
c Cell6A150Plastic
00006   2  -1.127       (-6 : -7 : -8 : -3 : -4 : -5 ) +11 +12 +18 +19
c Cell7PMME
00007   4  -1.18        (-9 : -10 : -11 : -12 )  #(-20 : -21 : -22 : -23 ) +18 +19
c Cell8V0id
00008   0              (-20 : -21 : -22 : -23 ) : -18 : -19
c Cell9Void
00009   0              -1 +2 +13 +14 +6 +7 +9 +10
c Cell10fOuter region
000010   -1             +1

[ I m p o r t a n c e ]     $Importance of each region in the counter
part = neutron proton alpha nucleus electron positron     $Secondary particles to be considered
 reg         imp
   1         1
   2         1
   3         1
   4         1
   5         1
   6         1
   7         1

[ T - Deposit ]                $Specification of dose and deposit energy distributions
    mesh = reg                 $Geometry mesh
    reg = 2                    $Depositied energy in the counter's sensitive volume is interseted $cell2
    unit = 3                   $Unit of deposited dose calculation Unit=3: Number [1/source]
    letmat =    0              $Material ID for LET, D=0: real material
    dedxfnc =   0              $User defined multiplier, 0(no)
    material =  all            $Number of specific material
    output = deposit           $Defenition of the output file
    part = (proton alpha nucleus electron positron) proton alpha nucleus (electron positron)
                               $Particles and interactions of interest in calculating the energy deposition
    e-type = 3                 $Energy mesh
```

```
    ne = 201                    $Number of energy groups in the deposit output file
    emin = 0.000197
    emax = 1.97
    axis = eng                  $Axis value of output data
    file =  Name_of_the_file.dat  $Deposit file name

[ T - gshow ] off   $Gives graphical geometry output for region boundary by xyz mesh.
 mesh = xyz
 x-type = 2
 nx = 49
 xmin = -5
 xmax = 5
 y-type = 2
 ny = 1
 ymin = -5
 ymax = 5
 z-type = 2
 nz = 48
 zmin = -5
 zmax = 5
 axis = xz
 file = MODdmax_CyTEPC_CERF_energy_distribution_neutron_CylindricalSource
 output = 2     $Region boundary + material color
$2d-type = 1
 resol = 50      $Multiply region line resolution by resol times
 width = 0.5    $The line thickness
 epsout = 1
 angel = noms nofr port
$gslat = 1      $Show lattice boundry
[END]
```

Appendix E

2.5 MeV neutron radiation field simulation data analysis

An example of MATLAB code used for analyzing the Cy-TEPC and/or Cy-GPC simulation results, to obtain event-size spectrum and dose distribution .

```
%========================================================================
% Name: Faezeh Forouzan (derived from a code written by Davis Broughton)
% Purpose of MATLAB Code: Process the pulse height tallies produced by
% PHITS to calculate response parameters of the
% TEPC after being irradiated by a 2.5 MeV neutron source
%========================================================================
clc;clear;
%------------------------------------------------------------------------
% Step (1) Import PHITS Deposit Tally results (deposit column in the  data
% file)
%------------------------------------------------------------------------
%The first and second column of the following matrix will store the energy
%deposition bin endpoints and the third column will store the average bin
%counts
DATA_FROM_PHITS = dlmread...
    ('1p5SensitiveVolume_CyTEPC_2p5MeVneutron_Source4x4_Cutoff.txt','');
%------------------------------------------------------------------------
% Step (2) Declare Required Information
%------------------------------------------------------------------------
%%%%%%%% CHECK THE FOLLOWING SECTION BEFORE RUNNING THE CODE
Source_Neutrons = 2E9; % %Number of Source Neutrons Incident on TEPC
Source_Surface_Area = 4^2; %Surface area of plane source [cm^2]
l_bar = 1.33; % Mean Chord Length of Simulated Site [um]
% l_bar for sphere & right cylinder: 1.33
rho = 1.318e-04; % Density of TE Gas in the sensitive volume (unit: g/cc)
m_gas = (rho/1000)*2.6507; % Mass of TE gas in the sensitive volume
% (unit: kg)
%%% DON'T CHANGE ANYTHING BEYOND HERE
%%%%%%%%%%%%%%%%%%%%%%%%%%%%%%%%%%%%%%%%%%%%%%%%%%%%%%%%%%%%%%%%%%%%%%%%%%%
linlog_bin_width = 0.04605; % Logarithmic Lineal Energy Bin Width [keV/um]
Fluence = Source_Neutrons/Source_Surface_Area; %Fluence of Neutron Source
% [n/cm^2]
%------------------------------------------------------------------------
% Step (3) Populate Lineal Energy vs. Counts Matrix
%------------------------------------------------------------------------
%The first column of the matrix below stores the lineal energy midpoint of
%each bin, the second column stores the corresponding counts, and the third
%column stores the associated standard deviation of the counts
DATA = zeros(length(DATA_FROM_PHITS),3);
%The loop below populates the first column
for i = 1:1:length(DATA_FROM_PHITS)
```

```
DATA(i,1) = 0.5*(DATA_FROM_PHITS(i,1) + DATA_FROM_PHITS(i,2))*(1000/l_bar);
%finds midpoint of the energy bin and converts to [keV/um]
end
%The second column will now be populated (this is the frequency of events)
DATA(:,2) = DATA_FROM_PHITS(:,3).*Source_Neutrons;
%Number of events in each bin
%The loop below populates the third column
for j = 1:1:length(DATA)
DATA(j,3) = sqrt(DATA(j,2)); %sqrt of number of events (error)
end
%-------------------------------------------------------------------------
% Step (4) Calculate the Frequency and Dose Mean Lineal Energy and their
% associated Standard Deviations
%-------------------------------------------------------------------------
%The following variables will assist in the calculation of quantities and
%their standard deviations
a = 0; %sum((y_i)^4*f(y_i))
b = 0; %sum((y_i)^2*f(y_i))
c = 0; %sum(y_i*f(y_i))
cd= 0;
d = 0; %sum(f(y_i))

%The loop below will calculate the value of yF and yD
for k = 1:1:length(DATA)
a = a + (DATA(k,1)^4*DATA(k,2));
b = b + (DATA(k,1)^2*DATA(k,2));
c = c + (DATA(k,1)*DATA(k,2));
cd = cd + ((DATA(k,1)*DATA(k,2))*(4/3)*1.602*10^(-10))/m_gas;
d = d + (DATA(k,2));
end
yF = c/d; %Value of yF
yD = b/c; %Value of yD
yf_SD = yF*sqrt(((sqrt(b)/c)^2) + ((sqrt(d)/d)^2));
%Standard Deviation of yF
yd_SD = yD*sqrt(((sqrt(a)/b)^2) + ((sqrt(b)/c)^2));
%Standard Deviation of yD
%-------------------------------------------------------------------------
% Step (5) Calculate the event-size spectrum and Dose Distribution
%-------------------------------------------------------------------------
%The first column of the matrix below stores the lineal energy midpoint of
%each bin, the second column stores the value of yd(y) for the bin, and the
%third column stores the associated standard deviation

ydy = zeros(length(DATA),3);
dose = zeros(length(DATA),3);

ydy(:,1) = DATA(:,1); %Load in the lineal energy bin midpoints
dose(:,1) = DATA(:,1);

%The loop below calculates the normalized value of yd(y) and dose for
% each bin and the associated standard deviation
for m = 1:1:length(DATA)
```

```
ydy(m,2) = (DATA(m,1)*DATA(m,2))/(c*linlog_bin_width);

ydy(m,3) = ydy(m,2)*sqrt((((DATA(m,1)*DATA(m,3))/...
          (DATA(m,1)*DATA(m,2)))^2) + ((sqrt(c)/c)^2));

dose(m,2) = ((DATA(m,1)*DATA(m,2)*(4/3)*1.602*10^(-10))/m_gas)/...
          (cd*linlog_bin_width);
end
%Plot the Partial Dose Distributions
fig2 = figure(2);
%This plot is usually compared to the normalized measured dose-rate spectra
%which is plotted in the second fig (fig 2) of the code written for
%measurements.
semilogx(ydy(:,1),ydy(:,2),'g')
hold on
semilogx(dose(:,1),dose(:,2),'b.')
%-------------------------------------------------------------------------
% Step (6) Calculate dose per unit fluence
%-------------------------------------------------------------------------
%The following variables will store the total absorbed dose and its
%standard deviation
Dose_per_unit_fluence = 0;
Dose_per_unit_fluence_SD = 0;

%The following loop will calculate the value of the above variables
for i3 = 1:1:length(DATA)
Dose_per_unit_fluence = Dose_per_unit_fluence + (DATA(i3,1)*DATA(i3,2)*...
    l_bar/1000);
Dose_per_unit_fluence_SD = Dose_per_unit_fluence_SD + (DATA(i3,1)^2*...
    DATA(i3,3));
end
Dose_per_unit_fluence_SD = 1.60218*10^-13*...
    sqrt(Dose_per_unit_fluence_SD)*l_bar/1000/(m_gas*Fluence);
Dose_per_unit_fluence = 1.60218*10^-13*Dose_per_unit_fluence/...
    (m_gas*Fluence);

hold on
```

Appendix F

14. 8 MeV neutron radiation field measured data analysis

An example of MATLAB code used for analyzing measurement results from Cy-TEPC and Cy-GPC, to obtain spectra and values of neutron dose rate and dose equivalent rate.

```
%========================================================================
% Name: Faezeh Forouzan (Derived from a code written by David Broughton)
% Purpose of MATLAB Code: Process the pulse height distribution produced by
% 14.8 MeV neutrons and measured with a 5 inch spherical TEPC
%========================================================================
%------------------------------------------------------------------------
% Step (1) Input measured data
%------------------------------------------------------------------------
%The first column of the following matrix will store the energy deposition
% bin midpoints and the second column will store the values of yd(y) in
% each bin
clc;clear;
D= csvread('dy_data_14p8_Neutrons_measurement.csv');
DATA_FROM_Sheet = D(:,1:2);

%------------------------------------------------------------------------
% Step (2) Populate Lineal Energy vs. dose (d(y)) Matrix
%------------------------------------------------------------------------
%The first column of the matrix below shows the lineal energy midpoint of
% each equal logarithmic bin, and the second column stores the
% corresponding yd(y) values.
DATA = zeros(length(DATA_FROM_Sheet),2);
%The loop below populates the first column
for i = 1:1:length(DATA_FROM_Sheet)
DATA(i,1) = DATA_FROM_Sheet(i,1);
end
%The second column will now be populated (this is the frequency of events)
DATA(:,2) = DATA_FROM_Sheet(:,2);
%The loop below populates the third column
for j = 1:1:length(DATA)
DATA(j,3) = sqrt(DATA(j,1)); %sqrt of number of events (error)
end
%------------------------------------------------------------------------
% Step (4) Calculate the Frequency and Dose Mean Lineal Energy and their
% associated Standard Deviations
%------------------------------------------------------------------------
%The following two quatities will store the frequency and dose mean lineal
%energies and their standard deviations respectively
yF = 0;
yD = 0;
yf_SD = 0;
yd_SD = 0;
```

```
%The following variables will assist in the calculation of quantities and
%their standard deviations (e and f are used for Q_bar)
a = 0; %sum((y_i)^4*f(y_i))
b = 0; %sum((y_i)^2*f(y_i))
c = 0; %sum(y_i*f(y_i))
d = 0; %sum(f(y_i))

%The loop below will calculate the value of yF, yD, standard deviations and
%relative errors;
for k = 1:1:length(DATA)
a = a + (DATA(k,1)^4*DATA(k,2));
b = b + (DATA(k,1)^2*DATA(k,2));
c = c + (DATA(k,1)*DATA(k,2));
d = d + (DATA(k,2));
end
yF = c/d; %Value of yF
yD = b/c; %Value of yD
yf_SD = yF*sqrt(((b)/(c^2)) + (1/d));  %Standard Deviation of yF
yd_SD = yD*sqrt(((a)/(b^2)) + (b/(c^2))); %Standard Deviation of yD
Rel_yf_D = yf_SD/yF; % Relative error of yF
Rel_yd_D = yd_SD/yD; % Relative error of yD
%-------------------------------------------------------------------------
% Step (5) Plot the Partial yd(y) Distributions
%-------------------------------------------------------------------------
fig1 = figure(1)
semilogx(DATA(:,1),DATA(:,2),'g')
```

Bibliography

Al-Bayati, S. N. (2012). *The application of experimental microdosimetry to mixed-field neutron-gamma dosimetry.* (Master of Applied Science (MASc)), UOIT, UOIT.

Alberts, W. G., Dietze, E., Guldbakke, S., Kluge, H., Schuhmacher, H.,. (1989). International intercomparison of TEPC systems used for radiation protection. *Radiation protection dosimetry, 29*(1/2), 47-53.

Ali, F., & Waker, A. (2019). Simulation of the Performance of Compact Tissue Equivalent Proportional Counters to Perform Neutron Dosimetry in CANDU Workplaces. *Candu Owners Group (COG) Technical Note, TN-18-3001*(TN-18-3001).

Ali, F., Waker, A., & Waller, E. (2013). Simulation of a compact multi element tissue equivalent proportional counter response in low energy monoenergetic neutron fields.

Attix, F. H. (1986). *Introduction to Radiological Physics and Radiation Dosimetry*. University of Wisconsin Medical school, Madison Wisconsin, United States: John Wiley & Sons.

Auxier, J., Snyder, W., & Jones, T. (1968). Neutron interactions and penetration in tissue. *Radiation dosimetry, 1*, 275-316.

Belhaj, O. E., Boukhal, H., El Mahjoub Chakir, K. L., Hadouachi, M., Sadeq, Y., Belhaj, S., . . . Soudjay, S. ISO 4037 2019: ESTABLISHMENT OF X-RAY NARROW-SPECTRUM SERIES USED IN THE NATIONAL SECONDARY STANDARD DOSIMETRY LABORATORY OF MOROCCO.

Benjamin, P., Kemshall, C., & Redfearn, J. (1968). A high resolution spherical proportional counter. *Nuclear Instruments and Methods, 59*(1), 77-85.

Berger, M. J. (1963). Monte Carlo calculation of the penetration and diffusion of fast charged particles. *Methods in Computational Physics., 135*.

Bielajew, A. F. (2001). Fundamentals of the Monte Carlo method for neutral and charged particle transport. *The University of Michigan, 1*.

Birkhoff, R., Turner, J., Anderson, V., Feola, J., & Hamm, R. (1970). The determination of LET spectra from energy-proportional pulse-height measurements I. Track-length distributions in cavities. *Health physics, 18*(1), 1-14.

Brackenbush, L. (1991). Using tissue equivalent proportional counters to determine dose equivalent.

Broughton, D. P., & Waker, A. J. (2017). Monte Carlo Simulations Comparing the Response of a Novel Hemispherical Tepc to Existing Spherical and Cylindrical Tepcs for Neutron Monitoring and Dosimetry. *Health physics, 112*(5), 430-438.

Burmeister, J., Kota, C., Maughan, R. L., & Waker, A. J. (2001). Miniature tissue-equivalent proportional counters for BNCT and BNCEFNT dosimetry. *Medical physics, 28*(9), 1911-1925.

Byun, S. H., Spirou, G. M., Hanu, A., Prestwich, W. V., & Waker, A. J. (2009). Simulation and first test of a microdosimetric detector based on a thick gas electron multiplier. *IEEE Transactions on Nuclear Science, 56*(3), 1108-1113.

Campion, P. (1971). The operation of proportional counters at low pressures for microdensity. *Physics in Medicine & Biology, 16*(4), 611.

Cirrone, G., Cuttone, G., Di Rosa, F., Pandola, L., Romano, F., & Zhang, Q. (2010). Validation of the Geant4 electromagnetic photon cross-sections for elements and compounds. *Nuclear Instruments and Methods in Physics Research Section A: Accelerators, Spectrometers, Detectors and Associated Equipment, 618*(1-3), 315-322.

Crossman, J., & Watt, D. (1994). Inherent calibration of microdosemeters for dose distribution in lineal energy. *Radiation protection dosimetry, 55*(4), 295-298.

Delafield, H., Holt, P., & Boot, S. (1976). Mixed field dosimetry with paired ionization chambers: CM-P00068567.

DeLuca Jr, P., Schell, M., Pearson, D., & Attix, F. (1981). Applicability of paired graphite and A150 plastic proportional counters to neutron-and photon-dose determinations: Wisconsin Univ., Madison (USA). Dept. of Medical Physics.

Dinar, N., Pozzi, F., Silari, M., Puzo, P., Chiriotti, S., De Saint-Hubert, M., . . . Waker, A. (2018). Instrument intercomparison in the high-energy field at the CERN-EU reference field (CERF) facility and comparison with the 2017 FLUKA simulations. *Radiation measurements, 117*, 24-34.

Evans, R. D. (1968). Radiation Dosimetry. *Vol. I, Fundamentals, edited by FH Attix and WC Roesch (Academic, New York, 1968)*, 106-109.

Faddegon, B. A., Kawrakow, I., Kubyshin, Y., Perl, J., Sempau, J., & Urban, L. (2009). The accuracy of EGSnrc, Geant4 and PENELOPE Monte Carlo systems for the simulation of electron scatter in external beam radiotherapy. *Physics in Medicine & Biology, 54*(20), 6151.

Farah, J., De Saint-Hubert, M., Mojżeszek, N., Chiriotti, S., Gryzinski, M., Ploc, O., . . . Olko, P. (2017). Performance tests and comparison of microdosimetric measurements with four tissue-equivalent proportional counters in scanning proton therapy. *Radiation measurements, 96*, 42-52.

Fasso, A., Ferrari, A., Ranft, J., & Sala, P. (1995). *An update about FLUKA.* Paper presented at the Proc. 2nd workshop on Simulating Accelerator Radiation Environment, SARE-2, CERN-Geneva.

Ferrari, A., Sala, P., Guaraldi, R., & Padoani, F. (1992). An improved multiple scattering model for charged particle transport. *Nuclear Instruments and Methods in Physics Research Section B: Beam Interactions with Materials and Atoms, 71*(4), 412-426.

Forouzan, F., & Waker, A. J. (2018). Development of heterogeneous proportional counters for neutron dosimetry. *Radiation protection dosimetry, 180*(1-4), 168-171.

Furuta, H., Nishide, A., Kudo, S. i., & Saigusa, S. (2020). Estimation of photon energy and direction distributions at Japanese nuclear power plants based on literature survey for J-EPISODE study. *Radiation protection dosimetry, 190*(4), 372-391.

Greening, J. R. (1985). *Fundamentals of radiation dosimetry*: CRC Press.

Hanu, A., Byun, S., & Prestwich, W. (2010). A Monte Carlo simulation of the microdosimetric response for thick gas electron multiplier. *Nuclear Instruments and Methods in Physics Research Section A: Accelerators, Spectrometers, Detectors and Associated Equipment, 622*(1), 270-275.

ICRP60. (1991). 1990 Recommendations of the International Commission on Radiological Protection. ICRP Publication 60. *Ann. ICRP 21 (1-3).*

ICRP103. (2007). ICRP publication 103. *Ann. ICRP, 37*(2.4), 2.
ICRU_Report10b. (1964). *Physical Aspects of Irradiation: Recommendations of the International Commission on Radiological Units and Measurements (ICRU). Report 10b 1962*: U.S. Department of Commerce, National Bureau of Standards.
ICRU_Report26. (1977). Neutron dosimetry for biology and medicine.
ICRU_report36. (1983). Report 36. *International Commission on Radiation Units and Measurements, Bethesda, MD*.
ICRU_Report95. (2017). Operational quantities for external radiation exposure.
Kellerer, A. M. (1971a). Considerations on the random traversal of convex bodies and solutions for general cylinders. *Radiation Research*, 359-376.
Kellerer, A. M. (1971b). Theory of wall-effects in microdosimetric measurements.
Kliauga, P. (1990). Measurement of single event energy deposition spectra at 5 nm to 250 nm simulated site sizes. *Radiation protection dosimetry, 31*(1-4), 119-123.
Kliauga, P., Rossi, H., & Johnson, G. (1989). A multi-element proportional counter for radiation protection measurements. *Health physics, 57*(4), 631-636.
Knoll, G. F. (2010). *Radiation detection and measurement*: John Wiley & Sons.
Kyllönen, J., & Lindborg, L. (2007). Photon and neutron dose discrimination using low pressure proportional counters with graphite and A150 walls. *Radiation protection dosimetry, 125*(1-4), 314-317.
Lindborg, L. (1975). Microdosimetry measurements in beams of high energy photons and electrons: Technique and results: Statens Straalskyddsinstitut.
Lindborg, L., & Waker, A. (2017). *Microdosimetry: experimental methods and applications*: CRC Press.
Malimban, J., Nam, U.-W., Pyo, J., Youn, S., & Ye, S.-J. (2019). Characterization of a new tissue equivalent proportional counter for dosimetry of neutron and photon fields: comparison of measurements and Monte Carlo simulations. *Physics in Medicine & Biology, 64*(17), 17NT02.
Mazrou, H., Idiri, Z., Sidahmed, T., & Allab, M. (2010). MCNP5 evaluation of a response matrix of a Bonner Sphere Spectrometer with a high efficiency 6 LiI (Eu) detector from 0.01 eV to 20 MeV neutrons. *Journal of radioanalytical and nuclear chemistry, 284*(2), 253-263.
Ménard, S., Cutarella, D., Lahaye, T., & Bolognese-Milsztajn, T. (2001). An active personal neutron dosemeter based on microdosimetric principles: CIME. *Radiation protection dosimetry, 96*(1-3), 265-268.
Mendoza, E., Cano-Ott, D., Guerrero, C., & Capote, R. (2012). New evaluated neutron cross section libraries for the GEANT4 code.
Menzel, H., Bühler, G., & Schuhmacher, H. (1982). *Investigation of basic uncertainties in the experimental determination of microdosimetric data.* Paper presented at the Proceedings, Eighth Symposium on Microdosimetry (J. Booz and HG Ebert, Eds.).
Min, Z., Shuhu, W., Cong, D., & Xu, J. (2017). *Modeling and simulation of TEPC based on GEANT4.* Paper presented at the 2017 13th IEEE International Conference on Electronic Measurement & Instruments (ICEMI).

Mitaroff, A., & Silari, M. (2002). The CERN-EU high-energy reference field (CERF) facility for dosimetry at commercial flight altitudes and in space. *Radiation protection dosimetry, 102*(1), 7-22.
Moro, D., & Chiriotti, S. (2015). EuTEPC: measurements in gamma and neutron fields. *Radiation protection dosimetry, 166*(1-4), 266-270.
Nam, U.-W., Park, W.-K., Lee, J., Pyo, J., Moon, B., & Kim, S. (2015). Proton beam dosimetry using a TEPC with a 252Cf neutron calibration. *Journal of the Korean Physical Society, 67*(8), 1459-1462.
National Bureau of Standards Gaithersburg MD; G. S. Hurst, R. S. C., F. C. Maienschein, H. H. Rossi, J. A. Sayeg, R. H. Schuler, R. W. Wallace. (1961). *Measurement of Absorbed Dose of Neutrons, and of Mixtures of Neutrons and Gamma Rays*: NBS.
Orchard, G., Feuerstake, T., McDonald, C., & Waker, A. (2021). Investigation of the stray neutron fields produced from proton irradiated Ta, Co-59, Ni, Fe, Inconel X750 and stainless steel 310 targets in a materials testing laboratory environment. *Applied Radiation and Isotopes, 178*, 109961.
Orchard, G. M., & Waker, A. J. (2018). The response of a multi-element tissue equivalent proportional counter in accelerator based high-altitude neutron fields. *Radiation protection dosimetry, 180*(1-4), 142-145.
Podgorsak, E. B. (2005). Radiation oncology physics. *a handbook for teachers and students/EB Podgorsak.–Vienna: International Atomic Energy Agency, 657*.
Povinec, P. (1979). A study of proportional counter optimization for long-term counting. *Nuclear Instruments and Methods, 163*(2-3), 363-368.
Qashua, N., & Waker, A. (2011). Study of the effect of high dose rate on tissue equivalent proportional counter microdosimetric measurements in mixed photon and neutron fields. *Nuclear Instruments and Methods in Physics Research Section A: Accelerators, Spectrometers, Detectors and Associated Equipment, 652*(1), 854-857.
RMTL. (2015). Reactor Materials Testing Laboratory at Queen's University
Rossi, H. (1983). Multi-element dosimeters for radiation protection measurements.
Schrewe, U., Schuhmacher, H., Brede, H., & Dietze, G. (1990). Determination of photon and neutron dose fractions with tissue-equivalent proportional counters. *Radiation protection dosimetry, 31*(1-4), 143-147.
Siebert, B., Grindborg, J., Grosswendt, B., & Schuhmacher, H. (1994). New analytical representation of W values for protons in methane-based tissue-equivalent gas. *Radiation protection dosimetry, 52*(1-4), 123-127.
Sigma Evaluated Nuclear Data File (ENDF) Retrieval & Plotting. Retrieved from: https://www.nndc.bnl.gov/sigma/index.jsp?as=14&lib=endfb7.1&nsub=10
Sigma Evaluated Nuclear Data File (ENDF) Retrieval & Plotting. from https://www.nndc.bnl.gov/sigma/index.jsp?as=14&lib=endfb7.1&nsub=10
Standardization, I. O. f. (2001). *REFERENCE NEUTRON RADIATIONS: Pt. 1 Characteristics and Methods of Production*: International Organization for Standardization.
Stinchcomb, T., Kuchnir, F., & Skaggs, L. (1980). Comparison of the microdosimetric event-size method and the twin-chamber method of separating dose into neutron and gamma components. *Physics in medicine and biology, 25*(1), 51.

Svensson, H., & Landberg, T. (1994). Neutron therapy—The historical background. *Acta Oncologica, 33*(3), 227-231.
Taylor, G., Hawkes, N., & Shippen, A. (2015). Accurate simulations of TEPC neutron spectra using Geant4. *Radiation Physics and Chemistry, 116*, 186-188.
Taylor, G., Jansen, J., Zoetelief, J., & Schuhmacher, H. (1995). Neutron W Values in Methane-Based Tissue Equivalent Gas up to 60 MeV. *Radiation protection dosimetry, 61*(1-3), 285-290.
Turner, J. E. (2005). Interaction of ionizing radiation with matter. *Health physics, 88*(6), 520-544.
Waker, A. (1983). *Gas gain characteristics of some walled proportional counters used in microdosimetry*. Paper presented at the Proc. 8th Symp. on Microdosimetry (Jülich).
Waker, A. (1995). Principals of experimental microdosimetry. *Radiation protection dosimetry, 61*(4), 297-308.
Waker, A. (2010). A preliminary study of the performance of a novel design of multi-element tissue equivalent proportional counter for neutron monitoring. *Radiation measurements, 45*(10), 1309-1312.
Waker, A., Schrewe, U., Burmeister, J., Dubeau, J., & Surette, R. (2002). Classical microdosimetry in radiation protection dosimetry and monitoring. *Radiation protection dosimetry, 99*(1-4), 311-316.
Waker, A., Szornel, K., & Nunes, J. (1997). TEPC performance in the CANDU workplace. *Radiation protection dosimetry, 70*(1-4), 197-202.
Waker, A. J. (1985). Experimental uncertainties in microdosimetric measurements and an examination of the performance of three commercially produced proportional counters. *Nuclear Instruments and Methods in Physics Research Section A: Accelerators, Spectrometers, Detectors and Associated Equipment, 234*(2), 354-360.
Waker, A. J. (1986). An investigation of the characteristics of a spherical single-wire proportional counter used for experimental microdosimetry. *Nuclear Instruments and Methods in Physics Research Section A: Accelerators, Spectrometers, Detectors and Associated Equipment, 243*(2-3), 561-566.
Wharton, C., Seabury, E., Chichester, D., Caffrey, A., Simpson, J., & Lemchak, M. (2011). *X-Ray Measurements Of A Thermo Scientific P385 DD Neutron Generator*. Paper presented at the APPLICATION OF ACCELERATORS IN RESEARCH AND INDUSTRY: Twenty-First International Conference.
Zaider, M., & Rossi, H. H. (1996). *Microdosimetry and its Applications*: Springer.
Zhao, X. (2010). *Micro-dose study on the tissue equivalent proportional counter used in the emitted nuclide by Berta particle Auger electron [D]*. (Master Dissertation), Tsinghua University.
Ziegler, J. F. Stopping and Range of Ions in Matter (SRIM) http://www.srim.org.
Ziegler, J. F., Ziegler, M. D., & Biersack, J. P. (2010). SRIM–The stopping and range of ions in matter (2010). *Nuclear Instruments and Methods in Physics Research Section B: Beam Interactions with Materials and Atoms, 268*(11), 1818-1823.